Diss. ETH No. 18796

MODEL-BASED OPTIMAL EMISSION CONTROL OF DIESEL ENGINES

A dissertation submitted to

ETH ZURICH

for the degree of

Doctor of Science

presented by

Michael Benz

Dipl. Ing. ETH in Mechanical Engineering

born April 27, 1978

citizen of Marbach, St. Gallen

accepted on the recommendation of

Prof. Lino Guzzella, examiner

Prof. Konstantinos Boulouchos, co-examiner

2010

Michael Benz

mbenz@alumni.ethz.ch

ETH Zürich

Institute for Dynamic Systems and Control

Sonneggstrasse 3

8092 Zürich, Switzerland

Planst Du für ein Jahr, so säe Korn, planst Du für ein Jahrzehnt, so pflanze Bäume, planst Du für ein Leben, so bilde Menschen.

Kuan Tzu

Acknowledgments

This thesis is based on my research performed at the Institute for Dynamic Systems and Control of ETH Zurich between 2004 and 2009. The first part of the project was funded by an Integrated Project of the European Commission FP6 Program (Green). The second part of the project was financially supported by Daimler AG.

First of all, I would like to thank my supervisor, Prof. Dr. Lino Guzzella, for providing me support, and for motivating me to follow the exhausting path over the top of the mountain (doctoral thesis). Furthermore, I would like to express my gratitude to Prof. Dr. Konstantinos Boulouchos for accepting to be my co-examiner, and for his valuable contributions. A special thanks goes to Dr. Christopher Onder for his technical inputs, his support at the project meetings, and especially for his assistance in writing the scientific papers. I really enjoyed the journeys to the half-yearly meetings of the Green project all over Europe.

Then, I would like to thank the team of Dr. Krutzsch at Daimler AG for their interest in my work. Many fruitful discussion during my visits in Untertürkheim improved the quality of the research and brought in the interests of the industrial partners. A special thank you goes to Dr. Rüdiger Steiner who organized all the subproject issues during the Green project and who supported me in writing the various technical and financial reports. In addition, I want to acknowledge the technical collaboration with the AVL List GmbH where I could produce the measurement data. Dr. Herwig Ofner and Dr. Ingo Allmer advocated for all my wishes to improve the quality of the experimental data sets.

I am further indebted to Brigitte Rohrbach for the outstanding proofreading of this text and all my scientific publications.

The time I spent at the Institute was challenging, sometimes frustrating, but mostly very enjoyable. Therefore, many thanks also to my colleagues for providing me a great working environment with many discussions in the Kafistübli also far beyond the research subjects. In particular, I would like to thank Alexander Schilling, Yves Hohl, and Ezio Alfieri from the diesel research group, as well as Frédéric Tschanz, Stephan Zentner, and Jonas Asprion who joined that research group during the last year of the project. A special thank you goes to Samuel Fux and Philipp Schürmann for the first implementation of the IDSC Engine Library, Tobias Nüesch for deriving the mean-value model of the light-duty engine, and Markus Hehn who helped me greatly in the implementation of the optimal control algorithm and in the writing of my second publication.

In addition, I want to mention Olle Sundström for his assistance in parallelizing my code and for his outstanding support concerning the IDSC computer cluster as well as Søren Ebbesen for helping me to solve various LaTeX problems.

Last but not least, I am very grateful to my family and friends for their support and encouragement which made the realization of this dissertation possible.

Zurich, March 29, 2010

Michael Benz

Abstract

This thesis presents a novel methodology for deriving control-oriented models of the raw emissions of diesel engines. An extended quasi-static approach is developed where some engine process variables, such as combustion or cylinder charge characteristics, are used as inputs. These inputs are chosen by a selection algorithm that is based on genetic programming techniques. Based on the inputs selected, a hybrid symbolic regression algorithm generates the adequate nonlinear structure of the emission model. With this approach the model identification efforts can be reduced significantly. Although this symbolic regression model requires only few parameters to be identified, it provides results comparable to those obtained with artificial neural networks that include five times more parameters. The symbolic regression model is capable of predicting the behavior of the engine in operating points not used for the model parametrization and it can be adapted easily to other engine classes.

The measurement data used to generate and test the raw emission model are obtained on two different engine test benches, one is a heavy-duty engine type and the other is a light-duty engine. Based on standard engine maps, various actuator input variations are tested. Approximately 300 static measurement points of the entire engine operating range are measured for both engine types. In addition, dynamic tests are performed

including load steps, accelerations, and driving cycles to be able to identify the transient behavior of the engine systems.

The model derived is then tested on two different application fields. First, the model is used as a virtual sensor to estimate the engine out emission during various operating conditions. Results from experiments under steady-state and transient operating conditions are used to show the accuracy of the modeling approach presented.

Second, the model is used to investigate optimal controls for the various actuators of a modern diesel engine system. A novel optimization method is proposed that allows a reduction of the pollutant emission of diesel engines during transient operation. The key idea is to synthesize optimal actuator commands using reliable models of the engine system and powerful numerical optimization methods. Therefore, the raw emission model is embedded into a mean-value engine model for the dynamics of the gas path including the turbocharger, the fuel injection, and the torque generation. The optimization substantially changes the input signals, such that the engine model is enabled to extrapolate all relevant outputs beyond the regular operating area. A feedforward controller for the injected fuel mass is used during the optimization to eliminate the nonlinear path constraints. A direct single-shooting method is found to be most effective for the numerical optimization. The simulation results show a significant potential for reducing the pollutant emissions while increasing the driveability of the vehicle.

Zusammenfassung

Die vorliegende Arbeit behandelt eine neue Methode zur Herleitung regelungstechnisch orientierter Modelle der Rohemissionen für Dieselmotoren. Ein erweiterter quasi-stationärer Ansatz wurde entwickelt, wobei charakteristische Prozessgrössen, wie zum Beispiel der Verbrennungsschwerpunkt oder Zylinderladungskenngrössen als Eingänge benutzt werden. Die Modelleingänge werden mittels eines mathematischen Verfahrens ausgewählt, das auf einem evolutionären Algorithmus beruht. Basierend auf den ausgewählten Eingängen wird mittels eines symbolischen Regressionsverfahrens eine nichtlineare Modellstruktur für das Emissionsmodell hergeleitet. Dank dieser Methodik kann der Modellierungsaufwand deutlich reduziert werden. Obwohl die gefundene Modellstruktur nur wenige Parameter hat, sind die Simulationsergebnisse vergleichbar mit künstlichen neuronalen Netzen, die mehr als fünf mal so viele Parameter aufweisen. Die gefundene Modellstruktur ist extrapolationsfähig und übertragbar auf andere Motortypen.

Für die Herleitung und die Überprüfung der Modellstruktur wurden Messungen auf zwei unterschiedlichen Motorprüfständen durchgeführt. Der Erste ist ein Lastkraftwagen-Motor, der Zweite ein Lieferwagenmotor. Ausgehend von den standard Motorenkennfeldern, wurden verschiedenste Aktuator Variationen durchgeführt. Für beide Motoren wurden ungefähr 300

statische Messpunkte im ganzen Betriebsbereich vermessen. Zusätzlich wurden noch dynamische Messungen von Lastsprüngen, Beschleunigungen und Fahrzyklen durchgeführt, um die Dynamik des Motorsystems zu identifizieren.

Das hergeleitete Modell wurde auf zwei möglichen Anwendungsfeldern getestet. Im Ersten stand die Verwendung als virtueller Sensor im Vordergrund. Das Modell wurde unter den verschiedensten Betriebsbedingungen getestet. Simulationsergebnisse von stationären sowie transienten Bedingungen zeigen die Genauigkeit des vorliegenden Modells.

Als Zweites werden optimale Betriebsstrategien des Dieselmotors untersucht. Eine neue Optimierungsmethode ist entwickelt worden, welche eine Verminderung der Rohemissionen während ausgewählten transienten Übergängen erreicht. Die Grundidee ist, optimale Aktuatorstellungen herzuleiten, basierend auf präzisen Modellen und mächtigen numerischen Methoden. Deswegen wurde das Rohemissionsmodell in ein Mittelwertmodell eingebettet, welches die dynamischen Prozesse des Gaspfades, des Turboladers, der Kraftstoffeinspritzanlage und der Drehmomententstehung abbildet. Der Optimierer verändert die Eingänge des Motorsystems wesentlich, daher muss das Gesamtmodell sehr gute Extrapolationsfähigkeiten besitzen.

Eine Kraftstoffsteuerung für die eingespritzte Dieselmenge wird verwendet, um die nichtlinearen Zustandsvorgaben einzuhalten. Das Optimierungsproblem wird mittels eines direkten Verfahrens gelöst. Simulationsergebnisse zeigen ein grosses Potential die Emissionen zu reduzieren und ebenso die Fahrbarkeit des Fahrzeuges zu steigern.

Contents

Chapter 1

Introduction

Due to ecological and economical reasons, drivetrains with low fuel consumption and toxic exhaust emissions are required. Diesel engines are often used for heavy-duty as well as for passenger car applications due to their lower fuel consumption compared with gasoline engines. Unfortunately, diesel engines emit relatively high amounts of nitrogen oxides (NO_x) and particulate matter (PM).

1.1 Motivation

Due to the more stringent emissions legislation, exhaust aftertreatment devices have become necessary. In contrast to gasoline engines, where the aftertreatment problem is solved by using an efficient three-way catalyst, there is no aftertreatment system for diesel engines established as yet, that would be comparable to the efficiency of a three-way catalyst. Nevertheless, there exist promising devices to reduce the exhaust emissions as well. Thus far economical reasons and restricted user friendliness have prevented their further spread. The reduction of PM is tackled by using a diesel particle filter (DPF), with the disadvantages of a higher fuel con-

sumption due to the higher backpressure in the exhaust system and the necessary regenerations of the filter. A selective catalytic reduction (SCR) catalyst is typically used to reduce emissions of nitrogen oxides. However, the SCR catalyst has a limited conversion rate and requires a second fluid (urea solution) to be carried on board.

The optimal control of the entire engine system is a challenging task. The engine control system cannot be optimized separately from the operation strategy of the aftertreatment devices due to the strong interactions between them. Coordinated operation strategies are thus a promising step toward effective engine systems. In addition, for each aftertreatment system a different calibration of the engine is necessary to guarantee an optimal interaction of the entire system. The calibration of the electronic control unit (ECU) is thus a time consuming process, requiring a large amount of measurement data and experienced engineers. Although powerful tools are available to support the calibration, the process is still far away from being possible in a fully automatic way.

Figure 1.1 shows the structure of a modern diesel engine system with its components and actuators. Several actuators affect the gas path and the fuel injection system. The gas path is equipped with an EGR valve, an intake air throttle, and a turbine with variable geometry (VTG). The common-rail injection system adds several additional degrees of freedom to the engine system. Multiple injection events with different injection pressures, timings, and durations offer various design parameters for calibration engineers. The optimal operation of a diesel engines themselves is thus an ambitious task. The driver operates the vehicle to follow a desired speed trajectory by actuating the gas pedal. The position of the gas pedal

determines the amount of fuel injected into the cylinders. The additional actuators present in the engine are used to increase engine power while reducing the output of emissions at the same time. Therefore, the control of this overactuated system offers a great potential for optimizations.

Currently, the control of diesel engines is mostly based on two-dimensional maps [1]. The inputs of these maps are the quantity of the fuel injected and the current engine speed. The maps are tuned until the results stay within the legislated limits for a given test cycle while the desired driveability of the engine is maintained. Feedback controllers are used to obtain the predefined boost pressure, EGR rate, and fuel rail pressure stored in the static engine maps. During transient operation, additional controls are used to keep emissions within a reasonable range. For instance, the actual injected fuel is restricted by limiters that are employed to prevent

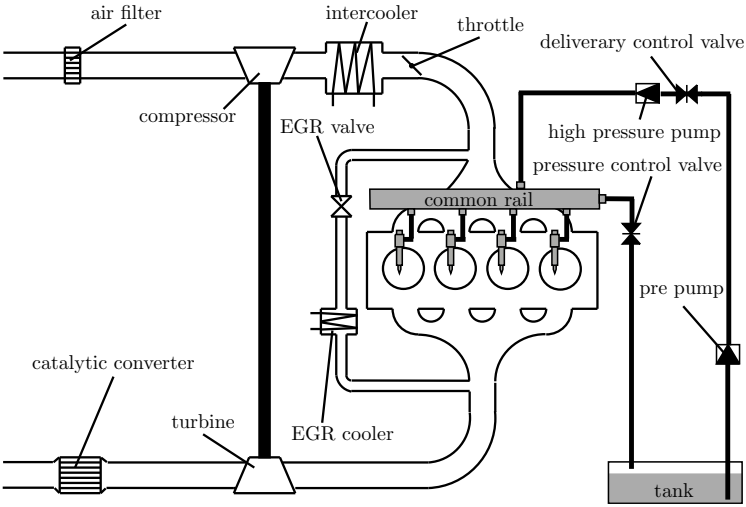

Figure 1.1: Illustration of a standard diesel engine and its components

smoke. Not surprisingly, in transient operation, suboptimal trajectories of the actuator inputs result, especially concerning the emissions values.

1.2 Objectives

On the basis of limited test bench availability due to economic and time restrictions, mathematical models are an essential tool for optimizing the configuration and the operation strategies of the engine system in static as well as in transient operation modes. These targets can be reached only with fast, yet accurate models based on a physics-oriented approach. Due to the better portability of such approaches, their fast application to other engines is guaranteed.

Therefore, the goal of the project is to develop a control-oriented raw emission model (PM, NO_x) of diesel engines. The main focus is on a simple description of engine-out emissions, while a good portability between different engines is to be ensured. The following application areas are to be investigated primarily:

- evaluation of engine system configurations,
- derivation of operation strategies ,
- controller design,
- application of virtual sensor designs.

Fast and accurate models allow the comparison and optimization of various engine concepts and operation strategies, such as high or low pressure

EGR or different aftertreatment configurations. The simulation-based engine design reduces test bench time and the costly refitting of the engine under investigation. New or different devices (e.g. turbocharger, aftertreatment system) can be investigated without requiring any previously manufactured expensive hardware. Using engine models, adequate control structures of the engine system can be investigated. In addition, acting as virtual sensors, models can replace expensive sensors.

1.3 Contributions

The research carried out within the framework of this dissertation have led to the following scientific publications:

- M. Benz, C.H. Onder, L. Guzzella, "Engine Emission Modeling using a Mixed Physics and Regression Approach", *Journal of Engineering for Gas Turbines and Power*, vol. 132, 2010.
- M. Benz, M. Hehn, C.H. Onder, L. Guzzella, "Model-Based Actuator Trajectories Optimization for a Diesel Engine Using a Direct Method", *Journal of Engineering for Gas Turbines and Power*, accepted.

The first paper was been submitted to the journal in March 2009 and is to be published in 2010. It presents a novel methodology to derive control-oriented model for static processes, which uses characteristic process variables as inputs into the model. The inputs are selected automatically by an algorithm based on genetic programming techniques and artificial neural networks. A symbolic regression method derives the equations of the

model. The methodology is tested on two different engine data sets.

The second paper was been submitted to the journal in September 2009 and is to be published in 2010. Based on a mean-value engine model (MVEM) and the extended quasi-static emission model introduced in the first publication, optimal input trajectories of a diesel engine system are derived. The goals are reduced outputs of the transient raw emission or an enhanced driveability, respectively.

The two publications have been incorporated in this thesis. Chapters 4 – 6 are mainly based on the first publication, while the second publication forms part of Chapter 7.

1.4 Outline

The dissertation is organized as follows: In Chapter 2 the state-of-the-art modeling approaches for engine systems are presented. In addition, several methods discussed in literature to derive engine controls are briefly introduced. In Chapter 3, the experimental setup is presented. Chapter 4 introduces the modeling methodology used, while Chapter 5 discusses the raw emission model derived using an extended quasi-static modeling approach. Various techniques are used to derive the mathematical model of the raw emissions. The raw emission model is tested on two application fields. In Chapter 6, the model is tested on various transient operations of the engine acting as a virtual raw emission sensor. Chapter 7 presents an investigation of optimal actuator controls. A direct single shooting method is chosen to solve the optimal control problem. Therefore, the raw emission model is embedded into a gas path model using a mean-value

engine model approach. Chapter 8 summarizes the thesis and draws some conclusions. In addition, an outlook for future research fields is provided. All the symbols and abbreviations used are listed in Appendix A.

Chapter 2

State of the Art

This chapter on the current state of the art contains two sections. Section 2.1 provides an overview of current modeling approaches for engine systems, whereas the focus of Section 2.2 is on the control of diesel engines.

2.1 Engine Modeling Approaches

To model the gas path of internal combustion (IC) engines, mean-value models are the state of the art for control-oriented applications (see, for example, [2], [3]). The mean-value model approach shows a good compromise between computational efficiency and accuracy. The physics-based approach simplifies the model calibration process. The relevant engine dynamics are represented by ordinary differential equations. The combustion is often treated as quasi-static in this modeling approach, since the gas path actuators used cannot influence or control the fast dynamics of the combustion process.

For the engine raw emissions a control-oriented modeling approach is not established as yet. Current models reported in literature can be divided into three main categories:

- empirical models [4],[5],
- phenomenological models [6],
- three-dimensional computational fluid dynamics (CFD) models [7].

The phenomenological and the CFD models are usually crank-angle-based and describe the in-cylinder processes in detail. Because of the high computational costs of these models, such approaches are not feasible for transient simulations that must run much faster than real-time. Event- or time-based empirical models are computationally more efficient. Therefore they can be used for real-time simulations. Black-box models are typical examples of this class of models. Since the internal structure of the system is unknown, the input/output behavior is modeled with either an artificial neural network (ANN) algorithm or with a polynomial approach (see, for example, [4], [5]).

The disadvantage of such a black-box modeling approach is the vast number of measurements needed to identify the parameters. This large number of parameters limits the portability of such models to other engine types or even to other operating points. The simulation results of these approaches tend to have a poor agreement to measurement data outside of the calibration range. Especially if the model is over-parametrized, poor results can appear in some operation ranges. One approach used to overcome these limitations is the use of so-called gray-box models, which reflect some of the internal physical laws.

A simple polynomial approach is presented in [8], where a statistical model of the (NO_x) emissions was developed. That model is based on relevant process variables. Because of the rather physics-based inputs, the

model is suitable to being applied on different engine types. The relevant process variables used are the center of combustion, the oxygen mass in the cylinder, and the total mass in the cylinder at intake valve closing. The inputs are chosen by expert knowledge. The model has been validated on a large number of static data of heavy-duty engines to show its portability.

A quasi-static approach is presented in [9]. The transient emissions are calculated by static base maps with transient correction factors, which are functions of the actual air/fuel ratio. The model is validated on several engines, showing a maximum relative error of approximately 30% during transient operations.

An ANN approach is presented in [10] based on characteristic pressure trace variables such as combustion center, maximum heat release rate, or peak pressure generated from steady-state measurements. The ANN is validated on measurement data from a transient driving cycle. The symbolic regression (SR) algorithm searches for functional coherences between the input and output data, which leads to a reduced number of parameters needed. The authors of [11] presented a model based on a SR algorithm to estimate the nitrogen oxide emissions directly from the electronic control unit (ECU) signals. Symbolic regression is a technique to reduce the number of parameters needed based on genetic programming techniques [12]. The SR algorithm is able to represent dynamic and static nonlinear data.

2.2 Optimal Control of Diesel Engines

To simplify the calibration of the engine control unit, several methods have been proposed in literature to replace the manual tuning of engine

parameters. A commonly used mathematically assisted calibration process is the design of experiments (DoE) method. An description of this kind of calibration process is given in [13].

Another method to reduce the measurement effort is described in [2], where the driving cycle is approximated by certain representative static operating points. Thus, the emission limits, which are only given for the integral behavior over the whole dynamic cycle, are incorporated into a mathematical optimization of a limited amount of static operating points. The sensitivities to all relevant inputs must be measured in these operating points. Nevertheless these two approaches still require a immense amount of measurement data. A model-based optimization of the static engine control maps using neural network models is proposed by [14].

The optimal control of the actuators during transient operation is discussed in literature as well. Several investigations of the optimal control of the turbocharger and the EGR valve have been conducted and published in [15], [16]. The target of those approaches is a reduction of the transient deviation of the air/fuel ratio using sophisticated control algorithms.

An approach to directly generate optimal input trajectories to reduce emission quantities has been proposed by the authors of [17], who derived an engine model using a generic test cycle with amplitude-modulated pseudo-random binary signals as inputs. These models are then integrated into an upper-level emission optimization tool to determine optimal engine settings. A mean-value engine model based optimization method is proposed by [18]. The model created is integrated in a dynamic optimization process to generate optimal turbine control laws.

Chapter 3

Experimental Setup

The measurements are carried out on two different engine types. The main parameters of these engines are shown in Table 3.1. Both are modern common-rail DI diesel engines equipped with a turbocharger and a high-pressure EGR system. The test benches are equipped with an AVL IndiCom^{TM} system to record the in-cylinder pressure traces. Since the IndiCom^{TM} system delivers an on-line evaluation of the in-cylinder pressure traces, the combustion characteristics such as combustion center can be stored during transient measurements in realtime. The pressure and temperature signals are measured in all receiver elements. The temperature at the outlet of the intercooler is controlled depending on the actual

Table 3.1: Technical data of the test bench engines

Engine type	heavy-duty (HD)	light-duty (LD)
Manufacturer	Daimler	Daimler
Feature	EGR, twin scroll turbine	EGR, VTG
Injection	Common-rail DI	Common-rail DI
Displacement volume	6.5 l	3.0 l
Number of cylinders	6	6
Maximum torque	950 Nm	440 Nm
Maximum power	194 kW	140 kW

operating point. An additional heat flow meter (Sensyflow) is used at the inlet of the engine.

The gas composition (NO, NO_x, CO, CO_2, O_2, THC) of the exhaust gas is measured with an AVL CEB II gas analyzer. The PM emissions are measured with an AVL 430 opacimeter and an AVL 415S smoke meter. A correlation curve is used to calculate the filter smoke number based on the opacity signal measured during transient operation. During the transient measurements, a fast nitric oxide (NO) sensor is used (Cambustion CLD 400). The probe is mounted directly after the exhaust valves. A second fast NO signal is measured just before the sampling point of the CEB II gas analyzer and the opacimeter sampling point, respectively. This measurement setup allows the identification of the exhaust gas path dynamics. The EGR rate is estimated based on CO_2 measurements in the intake and the exhaust manifolds. All the signals are stored at 100 Hz. During transient measurements, the ECU variables are also stored on the ECU application computer, at 1 kHz or 200 Hz, respectively. The measurement data are synchronized by reference signals stored on both recorders.

An overview of the measurements taken is shown in Table 3.2. A base map of both engines is measured. In addition, all the actuator inputs are varied in six relevant operating points, well distributed over the engine operating range. The systematic variations are measured starting from the base map settings. Single and double actuator variations are measured to cover the entire operating range of the engine. The data sets of both engines include approximately 300 static measurement points. Measurements of dynamic operation are taken as well to test the transient prediction capability of the proposed control-oriented emission model. The measurements

are carried out on a highly dynamic test bench and include load steps at constant engine speed, accelerations at constant load, and transient engine cycles like the European Transient Cycle (ETC). To identify the actuator dynamics, steps of all actuator inputs are measured as well.

Table 3.2: Overview of the measurement data

Engine Type	heavy-duty	light-duty
Static variations		
Boost pressure [bar]	1.0-3.0	1.0-2.5
EGR fraction [%]	0-25	0-35
Fuel rail pressure [bar]	500-1600	300 - 1800
Start of injection [°CA aTDC]	(-20) - 10	(-3) - 10
Intake temperature [°C]	25-70	25-75
Transient operating conditions		
Actuator steps [-]	-	u_{soi}, p_f, u_{vtg}, u_{egr}
Load steps at constant speed [%]	40-80	20-80
Accelerations at constant load [rpm]	-	1250-2750
Driving cycles	-	ETC Cycle

Chapter 4

Modeling Methodology

The novel modeling methodology used can be separated into two steps. First, the relevant process variables are chosen by an input variable selection algorithm (IVS), which is discussed in the next section. Using the selected variables as inputs for the model, a hybrid symbolic regression algorithm generates the efficient model equations using genetic programming techniques. The symbolic regression algorithm is presented in Section 4.2.

4.1 Input Variable Selection Algorithm

The selection of the input variables is a important step in the modeling approach. If the system is well known, the relevant inputs into the system can be selected by expert knowledge. Often, the coherences of physical systems are not well understood, or they are computationally expensive to model. The practitioner thus needs an algorithm that selects the relevant inputs directly from measurement data. Algorithms for the IVS task can be classified in wrapper (model-based) or filter (model-free) methods (for details see [19], [20]). Both approaches are briefly discussed next.

Filter techniques are model-free algorithms and utilize a statistical mea-

sure to determine the interdependencies of the input and output variables as the basis for the IVS. A popular method for the input selection is the principal component analysis (PCA) [21]. Its drawback is its sensitivity to noise and to data transformations. The underlying assumption of a linear structure is contradictory to the highly nonlinear system being analyzed here. For a nonlinear system, a common procedure for a filter-based IVS approach has not been established yet in the scientific community, but mutual information (MI) has recently been found to be a suitable measure of dependence for IVS (for details, see [22], [23]). In the present case of continuous data, the estimation of the mutual information can only be approximated. The selection of input variables based on mutual information is more robust to noisy data and nonlinear variable transformation. However, to find an optimal solution the selection algorithm must be able to handle redundant variables. Due to the model-free approach the IVS task based on filter techniques is computationally more efficient than the model-based wrapper techniques. Additionally the selection is more general because it does not depend on a certain model structure.

In contrast, the wrapper approach used in this study treats the input selection search as an optimization of an arbitrary model structure. The input selector exists as a wrapper around the fitness evaluation and the model calibration block. Figure 4.1 shows the procedure of the wrapper approach. The input selection search proposes a potential subset of all the possible inputs. The fitness evaluator calculates a fitness value for each subset to estimate the performance of the selection. Therefore, the chosen model structure is calibrated using the selected inputs. Once a certain performance is reached, the algorithm terminates.

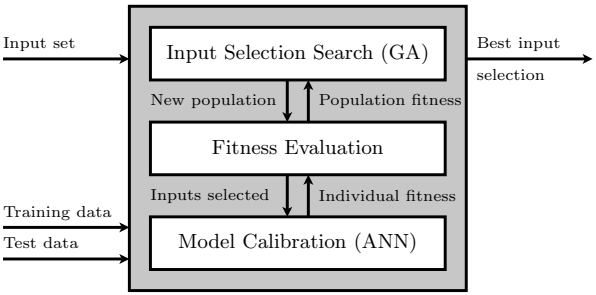

Figure 4.1: The wrapper approach as an input selection algorithm

A frequently used input selection search is the forward or backward selection, where the number of inputs is systematically increased or decreased by the most or least relevant inputs, respectively. Its drawback is that it yields only a suboptimal subset selection, especially if the initial set of possible inputs includes highly correlated variables. Heuristic techniques based on trial and error or so-called brute-force approaches can be used to find the optimal subset. These selection algorithms require an exhaustive search. If large numbers of possible inputs are available, these approaches are computationally too expensive. Thousands of input combinations require a calibration of the model structure. Hence for practical algorithms, the search is conducted for a satisfactory subset rather than for an optimal subset.

An algorithm based on genetic-programming techniques is used in this study to find a promising subset [12]. The input selection search proposes a combination of potential input candidates. Each individual of the population is represented by a bit string where 1 means that the input is selected and 0 that the input is not selected, respectively. After estimating the performance of each individual, a new population is generated. The algo-

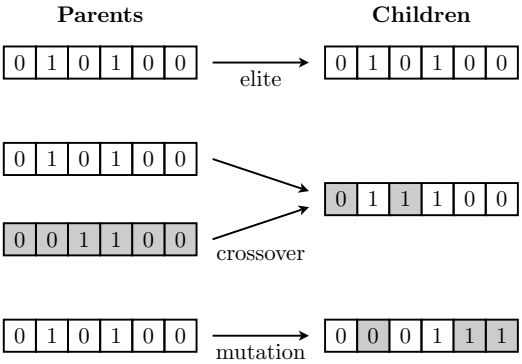

Figure 4.2: Bit string manipulation of the input selection algorithm

rithm is implemented in MATLAB. The parameters of the IVS algorithm used are shown in Table 4.1.

Figure 4.2 shows the scheme used to produce the new generation of individuals. The best individuals proceed directly to the new generation (elitism). The others are stochastically chosen for reproduction. The new individuals are generated by a crossover or mutation operation. As the inputs are neither sorted nor grouped, point mutations are used, where randomly chosen bits are mutated from 0 to 1 or vice versa. Due to the fact that only a small subset of potential inputs are to be selected, the mutation rate from 1 to 0 is set higher than from 0 to 1. The mutation rates from 0 to 1 r_{01} is calculated as

$$r_{01} = \frac{n_{\text{des}}}{n_{\text{tot}}} \tag{4.1}$$

and the mutation rate from 1 to 0 r_{10} as

$$r_{10} = 1 - \frac{n_{\text{des}}}{n_{\text{tot}}} \tag{4.2}$$

where n_{des} is the desired number of inputs and n_{tot} the total number of inputs.

The fitness values of the actual individuals are tested by a model. The model to estimate the output values can be a polynomial (see [24]). Because of its higher flexibility, the output is calculated with a feedforward ANN in this study. The ANN is adapted to the training data points y for every new combination of inputs in the actual population using Levenberg-Marquardt backpropagation [25].

The fitness value and the model output $\hat{y}$ of each combination is then stored in memory to avoid multiple evaluations of the same selection. The fitness value of the selection is calculated as the mean square error of the scaled emission value estimation and is additionally penalized with the factor f if the number of the selected inputs n_{sel} exceeds the desired quantity n_{des}. The input selection search minimizes this fitness value J

$$J = \frac{1}{m} \sum_{k=1}^{m} \left(y(k) - \hat{y}(k)\right)^2 \cdot f \tag{4.3}$$

Table 4.1: Parameters of the input selection algorithm

Parameter	Value
Population size	500
Generations	≈100
Desired number of inputs	2-5
Number of hidden layers	1
Number of neurons of ANN	5
Genetic operators	elitism, mutation, crossover
Elitism fraction	0.1
Crossover function	stochastic uniform
Crossover fraction	0.25
Mutation function	uniform
Mutation fraction	0.65
Selection function	stochastic uniform

where m is the number of measurement data and f is

$$f = \begin{cases} 1 & \text{if } n_{\text{sel}} \leq n_{\text{des}} \\ n_{\text{sel}} - n_{\text{des}} + 1 & \text{if } n_{\text{sel}} > n_{\text{des}} \end{cases} . \tag{4.4}$$

In the next step the parameter-intensive ANN is replaced with a lean model structure determined by the symbolic regression algorithm discussed in the next section.

4.2 Model Structure Derivation

As mentioned in the introduction of this chapter, the structure of the model is found with a symbolic regression (SR) algorithm [12]. For all the SR calculations, the GPLab toolbox for MATLAB is used [26].

A cluster of eight computers reduces calculation time to generate the model structure. The main node executes the tree manipulations and sends the parameter calibration jobs to the slave nodes. Since nearly all of the processor time is used to calibrate the parameters, the overall calculation time can be reduced by nearly a factor of 7. The toolbox is equipped with state-of-the-art genetic operators, survival, and reproduction methods. The individuals of the population are stored in trees. Figure 4.3 shows the tree structure and the possible tree manipulations. Two kinds of mutations can occur. The first is the point mutation where several nodes are mutated independently. The second is the tree mutation where a part of the tree is exchanged for a new randomly generated tree. The new tree part has a maximal size of nodes (initial maximal level). Due to the open source code, the toolbox can easily be extended with the user's own meth-

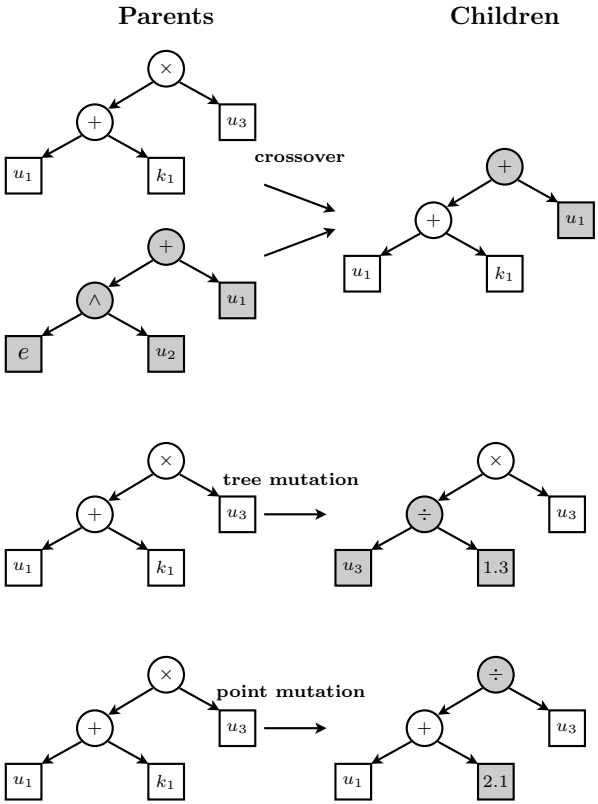

Figure 4.3: Symbolic regression: tree manipulations

ods. GPLab uses functions and terminals to represent the individuals. Any mathematical operation can be used as a function. Some operators demand protection to guarantee that the output is a real number. In this investigation the functions addition, multiplication, division, exponential, and the power function are used. The division is protected as follows:

$$a/b = \begin{cases} a/b & \text{if} \quad b \neq 0 \\ a & \text{if} \quad b = 0, \end{cases} \tag{4.5}$$

Therefore, if the b vector has a zero element the division is not evaluated. This part of the tree will presumably disappear or will be substituted due to a mutation in one of the next generations since it does not influence the fitness value. The power function is evaluated as

$$a^b = \exp(b \cdot \log(|a|)). \tag{4.6}$$

which results in a slightly faster evaluation.

Terminals can be input variables ($u_1 ... u_n$), constants (e.g. π), or random numbers. A new type of terminals is introduced to extend the application spectrum of the algorithm. The parameters ($k_1 ... k_8$) are used and calibrated separately for each tree generated. The toolbox is therefore extended with a local search algorithm based on a Nelder-Simplex approach [27]. The initial values of the parameters are set randomly between -1 and 1. The maximum number of variable parameters is approximately 8. If more parameters are required, a different local search algorithm must be used, for instance an evolutionary algorithm [28], since the solution found by the Nelder-Simplex algorithm would be suboptimal.

To avoid oversized individuals, a filter function replaces individuals with more nodes than a maximal tree size limit by randomly generated new trees. All the important settings of the symbolic regression algorithm used are shown in Table 4.2.

While the symbolic regression could also be used as an IVS algorithm, the advantage of separating the two steps is a reduced calculation time. The derivation of the model (ANN) used in the IVS algorithm takes around 10 seconds on a modern desktop computer. In contrast, for a given input

combination on the same computer the symbolic regression requires more than 50 hours to find the expected structure. A good selection of inputs with a poorly trained symbolic regression still has an insufficient fitness value. Therefore it is likely not chosen for the next generation. In addition, the separation simplifies the application of specifications to the number of inputs. Clearly, using the symbolic regression as an IVS algorithm is thus not recommended. Another advantage of the separated selection is the fact that different modeling approaches can be evaluated and compared.

Results of the modeling approach presented in this section are shown in the next chapter. The method is used to derive an extended quasi-static emission and combustion model of a diesel engine. However, the approach can be applied to various modeling problems. Also, dynamic models could be derived. In such a case, time-discrete signals with various numbers of delays Δt act as inputs

$$y = f\left(u_1(t), u_1(t-\Delta t), ..., u_1(t-i\cdot\Delta t), ..., \right. \tag{4.7}$$

$$\left. u_n(t), u_n(t-\Delta t), ..., u_n(t-i\cdot\Delta t)\right), \tag{4.8}$$

Table 4.2: Parameters of the symbolic regression algorithm

Parameter	Value
Population size	1000
Generations	≈ 100
Functions	plus, times, power, divide, exponential
Terminals	constant, random number, parameter
Number of parameters	8
Genetic operators	crossover, mutation
Mutation	pointmutation, treemutation
Maximal tree size	25 – 60 nodes
Initial maximal level	6
Elitism	keep best

where n is the number of possible process variables and i the maximal number of delays used. The number of delays is dependent on the slowest dynamic of the process to model. The time delay is chosen based on the fastest dynamic process.

Chapter 5

Control-Oriented Emission Model

The control-oriented emission model presented in this chapter is based on an extended quasi-static approach. This simplified approach does not consider any in-cylinder dynamics. Nevertheless, the transient deviations of the boundary condition of the combustion, such as mass in the cylinder at intake valve closing, affect the exhaust emissions. Therefore, the relevant deviations of the boundary conditions are used as inputs for the raw emission model.

The chapter is organized as follows. First, results of quasi-static simulations are presented and the deviations during transient operation are discussed. In Section 5.2, the extended quasi-static approach for the raw emissions is introduced. An important starting point for the design of the extended quasi-static model is the choice of the relevant inputs, which are selected by the input variable selection (IVS) algorithm introduced in Chapter 4. Possible inputs are characteristic engine process variables such as combustion center or cylinder mass. They are presented in Section 5.3. The results of the IVS algorithm are discussed in Section 5.4. The efficient structure of the model is then generated by the SR algorithm. The

structure derived is presented in Section 5.5.

The advantage of these process-relevant inputs and their functional coherence to the emission values is the reduction of parameters required to describe the emission formation. The adequate and therefore efficient structure reduces calculation time and future measurement efforts.

5.1 Quasi-Static Simulations

Quasi-static simulations are based on the assumption that maps are available that describe the correlation between the current operating point of the engine defined by engine speed and fuel mass flow and the outputs such as torque production. Depending on the application of these maps, the inputs and outputs are swapped.

In this research the pollutant emission outputs that are subjected to legal limits are stored in such base maps as well. These maps are built with static measurement data of the entire operation range of the engine. The inputs into these maps are engine speed and fuel mass flow, which represent the actual operating point. The operating point variables are scaled in order to increase the portability of the models generated. The engine speed is expressed as the mean piston speed

$$c_m = \frac{\omega_e \cdot S}{\pi}, \tag{5.1}$$

where ω_e is the engine speed and S the stroke. The injected fuel mass flow $\overset{*}{m}_f$ is scaled by the engine speed, the displacement value V_d, and the lower heating value H_l of the fuel. The fuel mean effective pressure is then

calculated as

$$p_{\mathrm{mf}} = \frac{H_l \cdot \overset{*}{m}_f \cdot 4\pi}{V_d \cdot \omega_e}. \tag{5.2}$$

Using these maps, quasi-static simulations (QSS) can be performed. For instance the quasi-static value of the engine torque T_{e_0} is calculated as

$$T_{e_0} = f(c_m, p_{\mathrm{mf}}). \tag{5.3}$$

The quasi-static values stored in the base map are linearly interpolated for the current operating point defined by mean piston speed and fuel mean effective pressure.

Quasi-static simulations are useful for calculating the fuel consumption on a transient cycle. However, the quasi-static assumption fails for the calculation of engine-out emissions, which is shown next. Figure 5.1 shows a comparison of the result of quasi-static simulations and measurement data during a load step. The measured engine torque and its quasi-static simulation agree quite well. In contrast, the PM emissions of the engine are substantially different from their QSS prediction. During the transient phase, the amount of PM emissions detected is approximately ten times higher than the quasi-static values, while the NO emissions are lower. These deviations can be explained by analyzing the boundary condition of the combustion process. The boost pressure substantially differs from its QSS value during the load step. Figure 5.2 shows the difference between measurement data and results of quasi-static simulations of the other gas path variables and the injection actuators. The relevant gas path variables are boost pressure, EGR rate, and the temperature after the intercooler. The intake manifold temperature is strongly dependent on the EGR mass

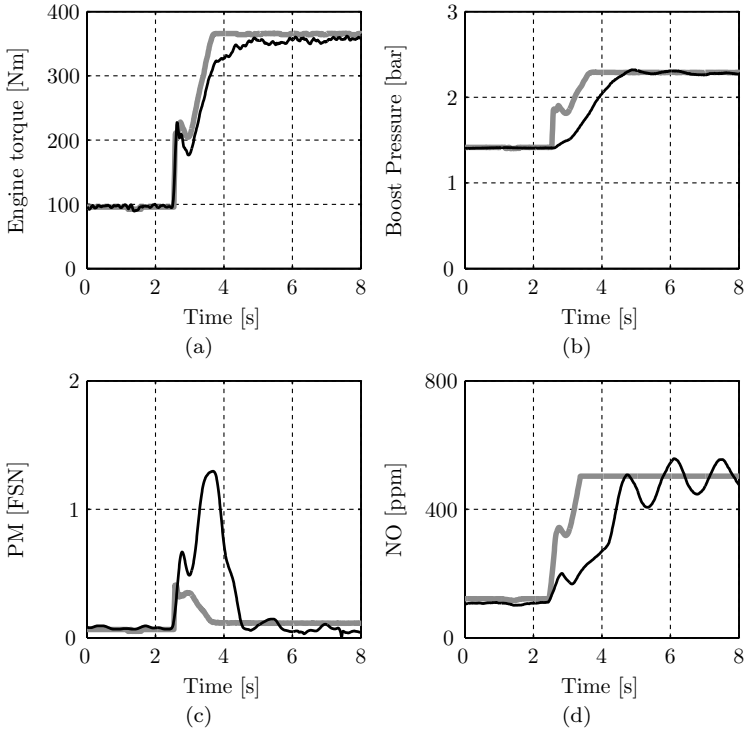

Figure 5.1: Comparison between measurement data (black) and results of quasi-static simulations (gray) during a step from 20% to 80% load at 2000 rpm: engine torque (a), boost pressure (b), PM emissions (c), and NO_x (d).

flow and temperature. To separate the two dynamics, the temperature after the intercooler is shown as well. Nevertheless, as a controlled intercooler is used on the test bench, the temperature dynamics are different from those of a real in-vehicle application of the engine. The gas path variables influence the mass and the gas composition in the cylinder at intake valve closing. The injection actuators are start of injection, fuel rail pressure, and injection duration. The turbocharger inertia causes the most significant dynamic effect in a modern DI diesel engine in that it in-

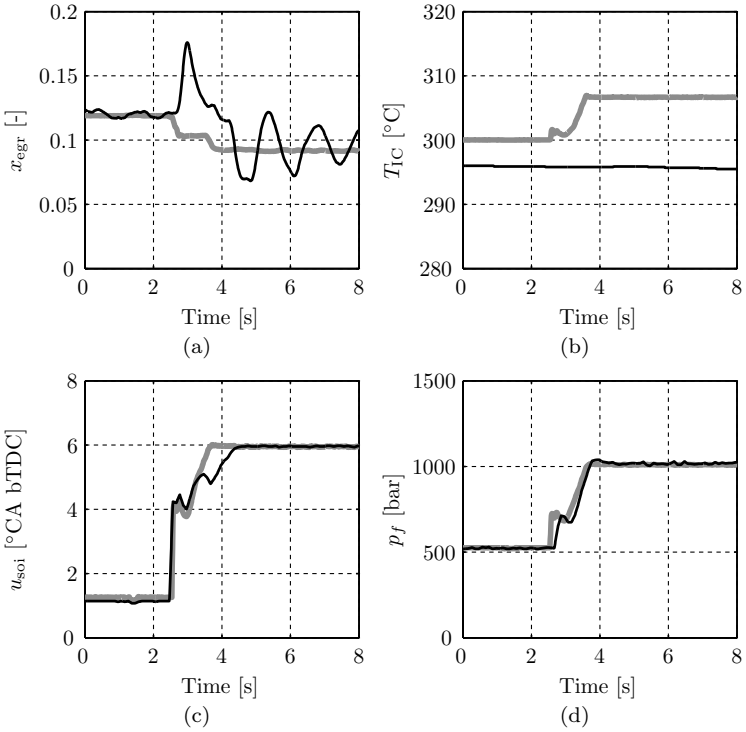

Figure 5.2: Comparison between measurement data (black) and results of quasi-static simulations (gray) during a load step at constant engine speed: EGR rate (a), temperature after the intercooler (b), start of main injection (c), and fuel rail pressure (d).

fluences the boost pressure and the EGR rate during transient operation. This turbo lag is responsible for the high PM emissions during transient operation of the engine, because these slow dynamics yield a relatively low air/fuel ratio of the cylinder charge. The start of injection follows mostly its quasi-static value in transient operating conditions. During a tip-in, the common-rail injection system cannot follow the desired fuel rail pressure. This leads to longer injection times, which increases the PM emissions

during a few engine cycles. The longer injection time causes the first PM emission peak during the load step shown in Fig. 5.1.

The influence of the cylinder wall temperature on the transient engine raw emission is negligibly small [29]. Therefore the temperature effects are neglected in the further investigations. The relevant boundary conditions of the combustion and of the emission formation can be summarized as:

- operating point (injected fuel, engine speed),
- cylinder charge (mass, gas composition, and gas temperature in the cylinder at intake valve closing),
- injection (fuel rail pressure, start, duration, and split of injection events).

The deviations of the boundary conditions are considered in the extended quasi-static emission model using correction factors. The extension describes the static and transient deviations of the raw emissions compared with the quasi-static values. An overview of the control-oriented REM is presented in the next section.

5.2 Extended Quasi-Static Model

Figure 5.3 shows the basic structure of the proposed control-oriented modeling approach for the raw emission. The model output $\overset{*}{\mu}_y$ stands either for the scaled PM emissions $\overset{*}{\mu}_{\mathrm{PM}}$ or for the scaled $\mathrm{NO_x}$ emissions $\overset{*}{\mu}_{\mathrm{NO_x}}$. The proposed raw emission model consists of two static parts. In the base map (QSS) part,

$$\overset{*}{\mu}_{y_0} = f(c_m, p_{\mathrm{mf}}), \tag{5.4}$$

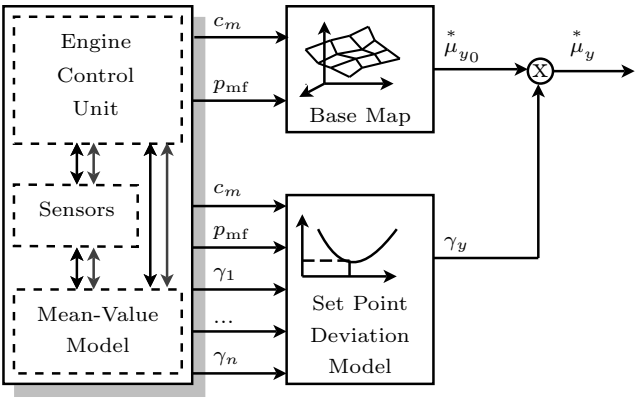

Figure 5.3: The structure of the control-oriented emission and combustion model structure used.

the quasi-static output value $\overset{*}{\mu}_{y_0}$ is a function of the actual mean piston speed c_m and the fuel mean pressure p_{mf}. The second part is the nonlinear set point deviation model, which models the transient deviations or static offsets of the emission values due to the changed boundary conditions of the combustion. The output of the set point deviation model is the correction factor γ_y. This correction factor models the ratio between the actual emission value and the base map value. The correction factor is modeled as a function of the operating point variables mean piston speed and fuel mean pressure as well as the additional inputs γ_i. Since the influences of these additional inputs may vary in the operating range, the operating point variables have to be included in the model of the correction factor γ_y

$$\gamma_y = f(c_m, p_{\mathrm{mf}}, \gamma_1, \gamma_2, ..., \gamma_n). \tag{5.5}$$

The inputs γ_i are the ratios of relevant engine process variables to their base map values. These variables represent the relevant boundary con-

ditions of the combustion. An input variable selection algorithm selects these variables. The selection algorithm is discussed in detail in Chapter 4. The relevant engine process variables used are presented in Section 5.3. The variables γ_i are calculated as

$$\gamma_i = \frac{u_i}{u_{i0}}, \tag{5.6}$$

where u_i is the actual value of the relevant engine process variable. The base map value u_{i0} of this relevant engine process variable again depends on the actual mean piston speed and the fuel mean effective pressure

$$u_{i0} = f(c_m, p_{\mathrm{mf}}). \tag{5.7}$$

The actual emissions value is then calculated as a multiplication of the base map value and the correction factor

$$\overset{*}{\mu}_y = \gamma_y \cdot \overset{*}{\mu}_{y_0} \ . \tag{5.8}$$

Neither the correction factor nor the base map value have any additional dynamics. The dynamics are considered only in the transient behavior of the inputs or correction factors, respectively. The structure is similar to that of the approach reported in [30] where the proposed linear set point deviation model is adopted as a virtual sensor to estimate and control the actual NO_x emissions at the engine out. Compared to [30], the main difference in this research is the nonlinear formulation of the set point deviation model. Since the PM emissions act highly nonlinear to air/fuel-ratio deviations, the assumption of linearity would not be appropriate.

Additionally, since the model should cover the entire operating range of the engine, large deviations from the standard operating point settings can occur in all boundary conditions.

The model can be calibrated with static measurement data due to the quasi-static formulation. Since the post-processing of transient measurement data is a demanding task, this formulation significantly simplifies the parametrization. The relevant engine process variables used as inputs into the set point deviation model can be provided by a mean-value model, or by sensor signals. The application area of the REM defines the final enveloping structure.

For the further calculation the emission values are scaled. This scaling increases the portability and the extrapolation capabilities of the generated models. Therefore the NO_x mass flows are divided by the fuel mass flow. The correction factors of the scaled NO_x emissions range between 0.4 and 2.5. The filter smoke number (FSN) is used to represent the PM emission. The base map values of the PM emissions are very low (≈ 0.1). In order to reduce the range of the correction factor, the PM correction factor is expressed as follows:

$$\gamma_{\mathrm{PM}} = \frac{\overset{*}{\mu}_{\mathrm{PM}} + 1}{\overset{*}{\mu}_{\mathrm{PM_0}} + 1}. \tag{5.9}$$

The final correction factors thus range between 0.5 and 4.

The design procedure of the set point deviation model can be divided into three main steps:

1. Definition of the relevant process variables by expert knowledge.
2. Selection of candidate variables from a set of characteristic process variables using the IVS algorithm.

3. Determination of a lean model structure based on the SR algorithm.

The results of the three steps are discussed in Sections 5.3 through 5.5.

5.3 Characteristic Process Variables

Most of the inputs (actuator values) into the system do not influence the emission values directly. The following line of action exemplifies this statement; the EGR valve actuator signal implies an open valve area. This valve area yields a certain EGR mass flow, which influences the cylinder charge at intake valve closed. Finally the exhaust gas mass in the cylinder significantly influences the raw emissions. Therefore, the model complexity can be reduced by using directly the exhaust gas mass in the cylinder as an input instead the actuator signal.

Analogously to this example, typical engine process variables must be defined first. The number of process variables used as inputs should be equal to or less than the number of actuators of the system. Otherwise an overdetermined system results. Table 5.1 shows the characteristic process variables used. Of course the list is not complete and other variables could be added. In addition, the actuator input signals are added. These signals are not selected by the IVS, as will be shown in the next section. This result shows the advantage of using the typical engine process variables. The values that are not measured directly are estimated.

The EGR fraction in the intake manifold is estimated based on the CO_2 measurement signal in the intake and exhaust receivers. The cylinder charge is estimated based on the EGR ratio and the intake mass flow sensor signal. The total cylinder charge is thus composed of intake air, external

Table 5.1: The 40 characteristic process variables used

Signal type	Symbol	Description	Unit
Actuator signals	u_{vtg}	variable turbine geometry input	[0-1]
	u_{egr}	EGR valve input	[0-1]
	u_{soi}	start of injection	[° CA]
	p_f	actual fuel rail pressure	[Pa]
	t_{inj}	injection duration	[μs]
	u_{thr}	throttle input	[0-1]
Gas path	p_2	intake manifold pressure	[Pa]
	ϑ_2	intake manifold temperature	[K]
	$\overset{*}{m}_{\mathrm{egr}}$	EGR mass flow	[kg/s]
	$\overset{*}{m}_{\mathrm{ia}}$	intake air mass flow	[kg/s]
	p_3	exhaust manifold pressure	[Pa]
	ϑ_3	exhaust manifold temperature	[K]
	λ	air/fuel ratio	[-]
	ω_{tc}	turbocharger speed	[rad/s]
Cylinder charge	m_e	total mass in cylinder	[kg]
	m_{air}	air mass	[kg]
	$m_{\mathrm{O_2}}$	oxygen mass	[kg]
	$m_{\mathrm{CO_2}}$	carbon dioxide mass	[kg]
	m_{bg}	burnt gas mass	[kg]
	x_{air}	air ratio	[-]
	$x_{\mathrm{O_2}}$	oxygen ratio	[-]
	$x_{\mathrm{CO_2}}$	carbon dioxide ratio	[-]
	x_{bg}	burnt gas ratio	[-]
Combustion	τ_{ID}	ignition delay	[μs]
	φ_{B01}	start of combustion	[° CA]
	φ_{B05}	location of 5% fuel mass burnt	[° CA]
	φ_{B10}	location of 10% fuel mass burnt	[° CA]
	φ_{B50}	location of 50% fuel mass burnt	[° CA]
	φ_{B90}	location of 90% fuel mass burnt	[° CA]
	φ_{B95}	end of combustion	[° CA]
	$\Delta\varphi_{B10-B50}$	duration from φ_{B10} to φ_{B50}	[° CA]
	$\Delta\varphi_{B50-B90}$	duration from (φ_{B50} to φ_{B90})	[° CA]
	$\Delta\varphi_{\mathrm{co}}$	combustion duration (φ_{B01}–φ_{B95})	[° CA]
	p_{max}	peak cylinder pressure value	[Pa]
	$\varphi_{p_{\mathrm{max}}}$	location of peak cylinder pressure	[° CA]
	$\overset{*}{Q}_{\mathrm{max}}$	maximum heat release rate (HRR)	[J/° CA]
	$\varphi_{\overset{*}{Q}_{\mathrm{max}}}$	location of maximum HRR	[° CA]
Injection spray	l_l	liquid spray length	[m]
	l_{lo}	lift-off length	[m]
	λ_{co}	air/fuel ratio of initial combustion	[-]

EGR, internal EGR, and injected fuel mass.

A one-zone heat release analysis is performed to obtain the in-cylinder process variables [31]. To avoid very large correction factors, all crank angle based signals are expressed as crank angle after 20° CA before top dead center. The model used to calculate the liquid fuel spray length and the lift-off length of the injection spray is proposed by [32] and [33]. Due to the fact that the calculation of the spray characteristics is an iterative process, it is quite time consuming. Finally the set of characteristic process variables contains highly redundant information which complicates the selection of an optimal subset.

The next step is to select the best combination from these process variables to build the inputs into the correction factor model. In total, 40 potential inputs are delivered to the IVS algorithm.

5.4 Results of the Input Selection

As mentioned in the previous chapter, it is not possible to calculate all combinations of inputs due to the limited computational resources available [34]. Therefore, the input selection algorithm introduced is used to choose a promising combination from the potential inputs defined in the previous section.

The parameters of the IVS algorithm are discussed next. The desired quantity of inputs is set to three, in addition to the operating point variables (mean piston speed, fuel mean pressure). The ANN used has four neurons in one hidden layer. The number of parameters depends on the number of inputs. If five inputs are selected, the number of parameters is

36 for the ANN structure used. Hence a large number of measurement data points is necessary to calibrate the ANN. Five times more measurement data than parameters are needed at least. The measurement data set is divided into a set of training data and a set of validation data. The best fitness value of the population stagnates after approximately one hundred generation runs. If the population size is five hundred, approximately fifty thousand neural networks need to be adapted to the data sets.

To find the most promising input combination, both engine data sets are used in parallel. The fitness value of each combination is calculated as the sum of the mean square errors of both data sets

$$J = \left(\frac{1}{m_1} \sum_{k=1}^{m_1} (y_1(k) - \hat{y}_1(k))^2 + \frac{1}{m_2} \sum_{k=1}^{m_2} (y_2(k) - \hat{y}_2(k))^2 \right) \cdot f \qquad (5.10)$$

where the factor f is calculated as in Eq. (4.4). The result of the IVS algorithm is the Pareto front with the best combination of inputs found. Few individuals evaluated have more than eight additional inputs due to

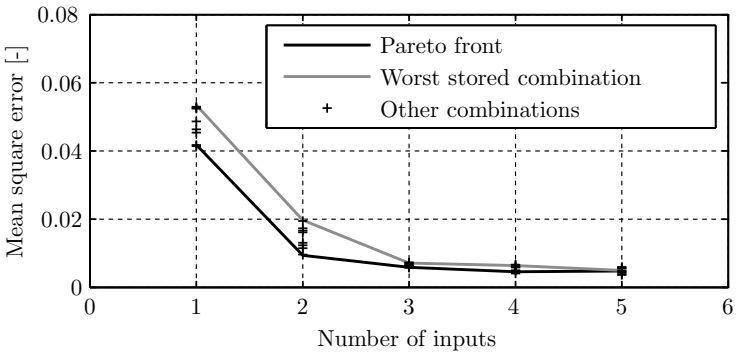

Figure 5.4: Pareto front of the input selection algorithm for the normalized nitrogen oxide emissions without factor f

the factor f. Therefore, the Pareto front yields reliable results between one and approximately eight additional inputs only.

Figure 5.4 clearly shows that the fitness value of the NO_x emissions decreases significantly until three additional inputs to the operating point variables are reached. The benefit of a higher complexity is very low. The six actuators ($u_{\mathrm{egr}}, u_{\mathrm{thr}}, u_{\mathrm{vtg}}, u_{\mathrm{soi}}, p_f, t_{\mathrm{inj}}$) and the engine speed can be summarized into three relevant process variables and the two operating point variables. If more than six or seven inputs into the model are used, the fitness value decreases even more. The calibration algorithm of the ANN finds only a suboptimal solution for the large number of parameters in this case. There are two likely explanations for this effect. Either the problem is overparametrized, or the input range is overdetermined, i.e., several inputs or combinations of them contain redundant information. Both cases result in an overfitted ANN which performs worse on the validation data. Additionally, fewer possible combinations are tested with more than eight parameters due to the extra penalty of the fitness value.

As expected, multiple combinations of inputs (due to the redundant information) yield nearly the same fitness value in the case of three or more inputs. If only two inputs are selected, the choice of the input subset is more sensitive. Thus, the engineer can choose a combination of "cheap" inputs. Inputs are called "cheap" if they are variables directly measured by a standard sensor or they can be easily calculated based on available sensor signals.

Table 5.2 presents the results of the input selection algorithm for the NO_x emissions. If only one input is selected, the best choice is the air or burnt gas fraction at intake valve closing. The best input combination for

two inputs selects the combustion center and the air fraction. All the other promising combinations in the Pareto front use one input describing the cylinder mass composition and one describing a combustion characteristic such as the start, the center, or the end of combustion. The benefit of using two additional inputs instead of one is high. If three additional inputs are chosen, the third input is used to characterize the cylinder mass composition more accurately. For example, the mass and the air fraction at intake valve closing are selected in addition to the combustion center. The combustion center is used in every promising combination. The author recommends the following input combination for the nitrogen oxides:

- operating point (mean piston speed, fuel mean pressure),

Table 5.2: Mean square error of each input selection for the NO_x emissions

		Light-duty [g/kg]	Heavy-duty [g/kg]
One input	x_{air}	0.0352	0.0385
	x_{bg}	0.0374	0.0396
	m_{bg}	0.0410	0.0403
	m_{air}	0.0638	0.0977
	λ	0.0580	0.1198
	φ_{B50}	0.0964	0.1021
	u_{egr}	0.1639	0.0773
Two inputs	φ_{B50}, x_{bg}	0.0077	0.0049
	φ_{B50}, x_{air}	0.0074	0.0054
	φ_{B90}, x_{air}	0.0102	0.0056
	φ_{B90}, x_{bg}	0.0108	0.0059
	φ_{B05}, x_{bg}	0.0145	0.0170
	φ_{B05}, x_{air}	0.0141	0.0191
Three inputs	φ_{B50}, p_2, x_{air}	0.0046	0.0029
	φ_{B50}, m_e, x_{air}	0.0048	0.0027
	φ_{B50}, x_{air}, l_l	0.0044	0.0032
	φ_{B50}, m_{air}, x_{air}	0.0055	0.0026
	φ_{B50}, x_{air}, p_3	0.0050	0.0031
	φ_{B50}, x_{air}, λ_{co}	0.0049	0.0035
	φ_{B50}, x_{air}, ϑ_3	0.0060	0.0026
	φ_{B50}, x_{bg}, l_l	0.0055	0.0033

- cylinder mass at intake valve closing m_e,
- air fraction in the cylinder at intake valve closing x_{air},
- combustion center φ_{B50},

which results in the following equation for the NO_x correction factor

$$\gamma_{\text{NO}_\text{x}} = f(c_m, p_{\text{mf}}, \gamma_{m_e}, \gamma_{x_{\text{air}}}, \gamma_{\varphi_{B50}}). \tag{5.11}$$

Then, inserting (5.11) into (5.8) yields the actual NO_x emission value.

Table 5.3 presents the results of the inputs selection algorithm for the PM emissions. If only one input is selected, the best choice is combustion

Table 5.3: Mean square error of each input selection for the PM emissions

		Light-duty [FSN]	Heavy-duty [FSN]
One input	$\Delta_{\varphi_{B50}-\varphi_{B90}}$	0.0403	0.0413
	m_e	0.0603	0.0517
	m_{air}	0.0612	0.0565
	λ	0.0541	0.0646
	φ_{B90}	0.0470	0.0842
	l_l	0.0897	0.1120
	u_{soi}	0.0948	0.2520
Two inputs	$\Delta_{\varphi_{B10}-\varphi_{B90}}$, m_{air}	0.0331	0.0194
	φ_{B90}, m_{air}	0.0361	0.0206
	φ_{B90}, m_e	0.0367	0.0184
	φ_{B50}, m_{air}	0.0330	0.0206
	$\Delta_{\varphi_{B10-B90}}$, m_e	0.0363	0.0194
	$\Delta_{\varphi_{B10-B90}}$, λ	0.0378	0.0193
	φ_{B50}, m_e	0.0345	0.0240
Three inputs	φ_{B50}, $\overset{*}{Q}_{\text{max}}$, m_e	0.0179	0.0173
	φ_{B90}, p_f, m_{air}	0.0212	0.0144
	φ_{B10}, φ_{B50}, m_e	0.0203	0.0160
	φ_{B05}, $\overset{*}{Q}_{\text{max}}$, m_e	0.0196	0.0170
	$\Delta_{\varphi_{B10-B90}}$, φ_{B50}, m_e	0.0242	0.0135
	φ_{B50}, m_e, u_{soi}	0.0219	0.0175
	l_l, m_{air}, τ_{inj}	0.0177	0.0222
	φ_{B50}, m_{air}, u_{soi}	0.0211	0.0189

duration. The best input combination for two inputs is the combustion duration and the air mass at intake valve closing. All other promising combinations in the Pareto front use one input describing the cylinder mass composition and one describing a combustion characteristic. If three additional inputs are chosen, the third input is used to characterize the combustion duration more accurately. For example, the fuel rail pressure or the maximal heat release rate are selected additionally. The end of the combustion seems to be more important for characterizing the PM emissions. The benefit of using three additional inputs instead of two is higher than for the NO_x emissions. The following inputs are recommended for the PM emissions:

- operating point (mean piston speed, fuel mean pressure),
- cylinder air mass at intake valve closing m_{air},
- fuel rail pressure p_f,
- location of the 90% fuel mass burnt φ_{B90}.

The PM correction factor is then estimated as follows:

$$\gamma_{\mathrm{PM}} = f(c_m, p_{\mathrm{mf}}, \gamma_{m_{\mathrm{air}}}, \gamma_{p_f}, \gamma_{\varphi_{B90}}). \tag{5.12}$$

The engine-out PM emission value is then calculated as

$$\overset{*}{\mu}_{\mathrm{PM}} = (\overset{*}{\mu}_{\mathrm{PM_0}} + 1) \cdot \gamma_{\mathrm{PM}} - 1. \tag{5.13}$$

In the next step, the artificial neural networks are replaced by a lean model structure derived by using the symbolic regression algorithm.

5.5 Results of the Symbolic Regression

In this section the results of using the symbolic regression algorithm are presented. The symbolic regression is performed for two different data sets in parallel. However, the inputs and the tree structure used are identical for both data sets. Only the variable parameters are calibrated by the local search algorithm for both data sets separately. The fitness value of each individual is then calculated as the sum of the mean square errors of both data sets. Hence both data sets are weighted equally. Figure 5.5 shows a plot of the NO_x emission fitness values for various maximal tree size limits. The fitness values decrease significantly up to a limit of 15 nodes for both data sets. If the limit is set higher than 40 nodes, the mean square error marginally decreases. Therefore the maximal number of nodes is set between 25 and 40.

Using a tree size limit of 25 nodes, the resulting function for the NO_x

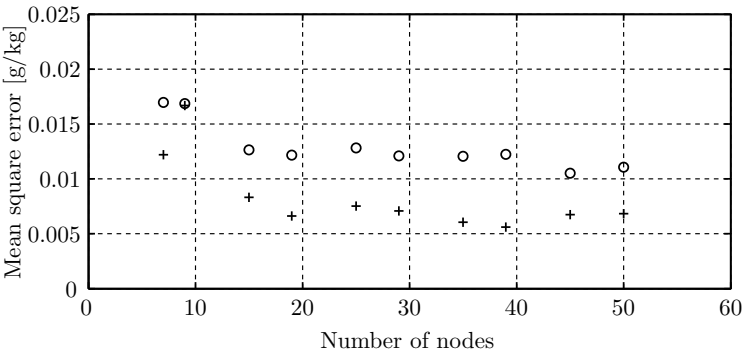

Figure 5.5: Mean square error for the NO_x emissions for the two different data sets, light-duty engine (circle), heavy-duty engine (plus sign)

correction factor $\gamma_{\mathrm{NO_x}}$ is

$$\gamma_{\mathrm{NO_x}} = \left(\gamma_{\varphi_{B50}} \cdot {\gamma_{x_{\mathrm{air}}}}^{\left(\gamma_{x_{\mathrm{air}}}+k_3\right)}\right)^{k_5 \cdot a \cdot b} \tag{5.14}$$

where a and b are defined as

$$a = \left(\frac{\gamma_{\varphi_{B50}}}{\gamma_{x_{\mathrm{air}}}}\right)^{k_2 \cdot \gamma_{m_e} + k_1} \tag{5.15}$$

$$b = \frac{\gamma_{\varphi_{B50}}}{c_m} + k_4 \tag{5.16}$$

The mean fuel effective pressure is not included in the function. Hence, the influence of the load on the correction factor is negligible. Furthermore not all of the variable parameters are used. The resulting formula has five variable parameters.

The generated function for the PM correction factor γ_{PM} is

$$\gamma_{\mathrm{PM}} = \left(\gamma_{m_{\mathrm{air}}} {}^{a\left(\frac{k_1}{\gamma_{\varphi_{B90}}}\right)^{-\gamma_{p_f}}}\right)^{k_4 \cdot b} \tag{5.17}$$

where a and b are defined as

$$a = \frac{k_2 \cdot {\gamma_{m_{\mathrm{air}}}}^{k_3}}{\gamma_{p_f}} + k_5 \tag{5.18}$$

$$b = p_{\mathrm{mf}} + \gamma_{\varphi_{B90}} + k_6 \tag{5.19}$$

The mean piston speed is not selected as an input. The formula contains six variable parameters. Table 5.4 lists the optimized parameter values for the $\mathrm{NO_x}$ and the PM formulas, respectively. The parameters for the $\mathrm{NO_x}$ model diverge moderately for the two data sets, whereas the PM

model parameters differ significantly for the two data sets. The resulting small number of parameters of the models allows their fast application to other engine types. In contrast to the ANN model used for the IVS algorithm, the number of parameters needed can be reduced by a factor of six. In addition, the reduced number of parameters is directly correlated to the amount of measurement data needed for the calibration of the model, as shown below. The results are comparable with those obtained from the neural networks approach used in the IVS algorithm. The portability of the emission models is shown using the two data sets from engines of very different sizes. This result corroborates the use of well-selected, characteristic engine process variables as inputs to the nonlinear statistical model.

Figure 5.6a shows the parametrization results of the NO_x formula derived for various training data fractions. To parametrize the formula ,less than one tenth of the measurement are needed to yield reliable results. Therefore, the amount of measurement data required can be reduced significantly. Fifty measurement data points selected out of the 300 points are sufficient to calibrate the model. The PM emission formula requires an increased training data fraction. Nevertheless, a training data fraction

Table 5.4: Parameter values of the resulting formulas

	k_1	k_2	k_3	k_4	k_5	k_6
Light-duty engine						
NO_x	8.36	-8.94	-4.54	-2.41	-2.58	...
PM	5.01	-775.0	152.0	-45.4	2.86	-1.33
Heavy-duty engine						
NO_x	-3.61	3.03	-3.17	-3.04	-4.06	...
PM	1.73	-0.02	463.0	-1.99	0.06	0.31

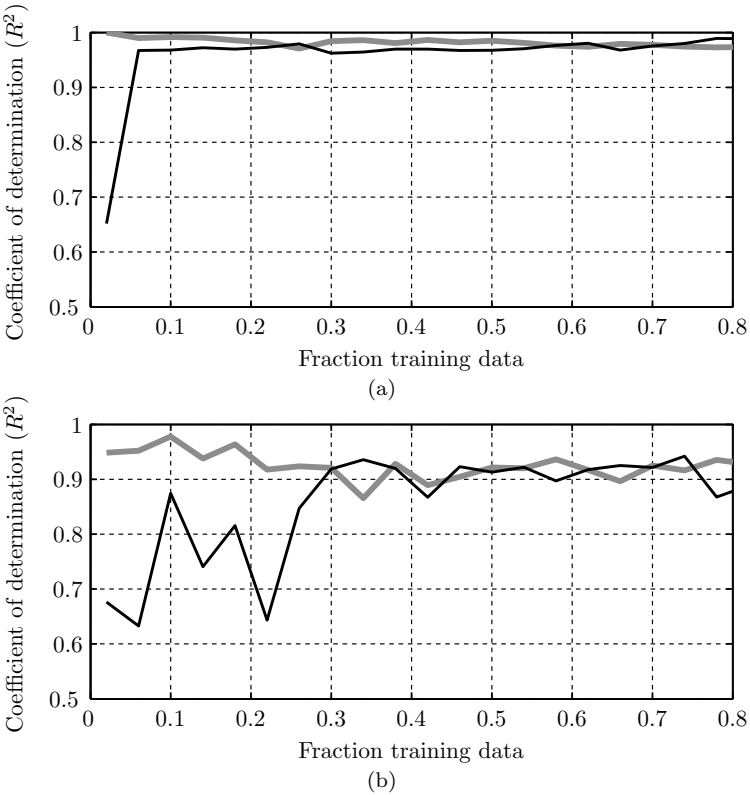

Figure 5.6: Coefficient of determination of the training data set (gray) and the validation data set (black) of the light-duty engine for various training data fractions: NO_x emissions (a) and PM Emissions (b).

of 30% is adequate as Fig. 5.6b shows. Since, the whole data set includes approximately 300 data points, the measurement data set should include at least 100 data points to parametrize the PM emission formula reliably.

The simulation results of the model structures derived with the proposed method show a good correlation with the static measurement data. Figures 5.7 and 5.8 show the results of the NO_x and PM emission model for the light-duty (LD) and the heavy-duty (HD) engine types. The regression of the PM emission is worse due to the relatively high measurement

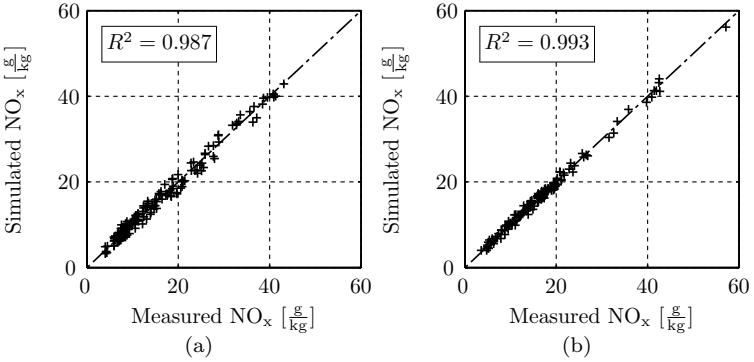

Figure 5.7: Regression plot of the NO_x emissions: LD (a) and HD (b) engine type using in-cylinder pressure sensors

errors, especially for low filter smoke numbers. Overall, the model performs better on the HD engine data set. This fact can be explained by the two different base maps used for the LD engine measurements. Unfortunately, for the LD engine only static and dynamic measurement data with different base maps were available. The transient measurements are carried out with a different timing of the start of injection. Therefore, the base map used for the transient measurements is taken to calculate the correction factor values for the static measurement data as well. Hence, large correction factors occur in most static measured actuator variations. Figure 5.9 shows the results of the emission model using non-optimized parameters. The parameters of the LD engine data set are used to calculate the emissions of the HD engine data set. The performance obtained with the non-optimized parameters shows not only the portability of the structure derived, but also of the parameters, even though the estimation of the PM emissions contains some outliers.

Further results of the raw emission model are shown in the next chapter

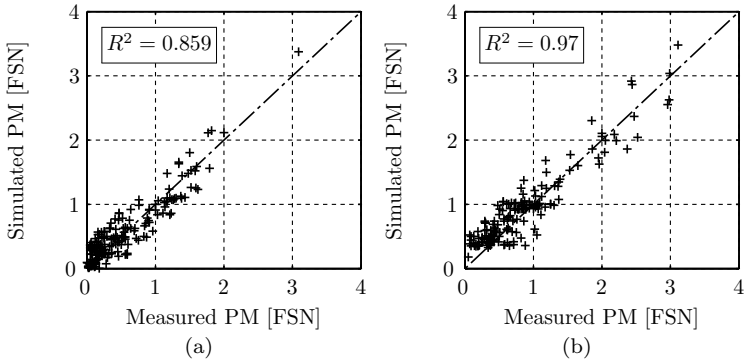

Figure 5.8: Regression plot of the PM emissions: LD (a) and HD (b) engine using in-cylinder pressure sensors

where the model is used as a virtual sensor to estimate the raw emission during various transients.

5.6 Summary and Discussion

The purpose of this analysis is to formulate a method to derive a control-oriented model of the raw emissions of a diesel engine. The mixed physics and regression approach proposed simplifies the generation of nonlinear models. The models derived are advantageous due to their increased portability to other engines. The modeling methodology proposed is applicable to various problems.

The method drastically reduces the calibration effort due to the reduced number of parameters needed to describe the transient raw emissions. The extended quasi-static approach is adequate to describe the combustion and the formation of emissions. Due to the extended quasi-static approach, the raw emission model can be calibrated with static measurement data, which

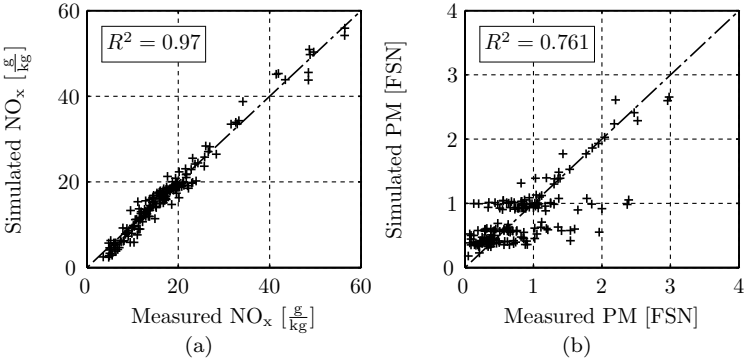

Figure 5.9: Regression plot of the emission model using the HD engine data set with the LD engine parametrization: NO_x (a) and PM (b) emissions

lowers the application costs of the model and the requirements for the test bench.

The inputs to the raw emission model are chosen by an input variable selection procedure based on a genetic programming wrapper approach. The input selector is fed with some 40 characteristic process variables. Due to the highly redundant process variables used as candidates, the input variable selection algorithm proposes a selection of promising subsets. As expected, several combinations show a comparable performance. The practitioner has the option of choosing a subset of inputs that is easy to measure or to estimate.

The functional structure of the raw emission model is derived with a symbolic regression algorithm. The toolbox used is extended with a local search algorithm to calibrate the parameters of the functional relations generated. The separation of the input variable selection task from the model structure generation significantly reduces the computational effort. The performance of the model derived is similar to that of an ANN with

around ten times more parameters. The method used is tested on two different engine types, and it yields similar results. The model shows a good portability to other engine types, especially the NO_x model.

In the next two chapters, the model derived is tested on two different application scenarios. In Chapter 6, the raw emission model is used as a virtual sensor to estimate the emission values during transient operation of the engine. The simulation results are compared to measurement data, showing the extrapolation capabilities of the derived modeling structure. The static-formalized model performs well on various transients.

In Chapter 7 the raw emission model is embedded in a mean-value engine model describing the gas path dynamics. The total engine system model is used to investigate optimal actuator inputs during transient operation of the engine.

Chapter 6

Application I: Virtual Sensor

This chapter presents a virtual sensor application of the raw emission model generated. Some of the transient inputs into the set point deviation model can be provided directly by standard sensor signals of the ECU. Nevertheless, several additional parts of the engine must be modeled to estimate all of the relevant engine process variables selected. If the REM is used as a virtual sensor, the cylinder charge variables (m_e, x_{air}) and the combustion characteristics (φ_{B50}, φ_{B90}) must be estimated by a model. Figure 6.1 shows the signal flow chart of the three combined models. Due to the slow dynamics of the CO_2 measurement device available, the EGR mass flow is not measured during transient operation of the test bench. Therefore a cylinder charge estimation is necessary to compare the REM estimations with measurement data. The combustion characteristics are measurable with a real-time cylinder pressure evaluation available at the test bench. The combustion model is optional in this case.

The cylinder charge variables are estimated by a simple gas path model, which is discussed in Section 6.1. The combustion model used is presented in Section 6.2.

If the emission model is used as a standalone, the entire engine systems must be modeled. This includes the intake air path, the exhaust gas path, the turbocharger, the EGR system, the gas-exchange cycle, and the combustion cycle. In this case, the necessary dynamic signals can be estimated by a state-of-the-art mean-value engine model [35]. Such an approach is shown in the second application scenario discussed in Chapter 7.

6.1 Cylinder Charge Estimation

Due to the lack of an EGR mass flow sensor, the cylinder charge (mass and gas composition) at intake valve closing must be estimated by a model. The remaining gas path signals are measured directly by standard ECU sensors. The EGR mass flow estimation is based on the intake mass flow sensor signal and an engine mass flow estimation. The EGR mass flow can be calculated as

$$\overset{*}{m}_{\text{egr}} = \frac{d}{dt} m_2 + \overset{*}{m}_{e,\text{in}} - \overset{*}{m}_{\text{hfm}}, \tag{6.1}$$

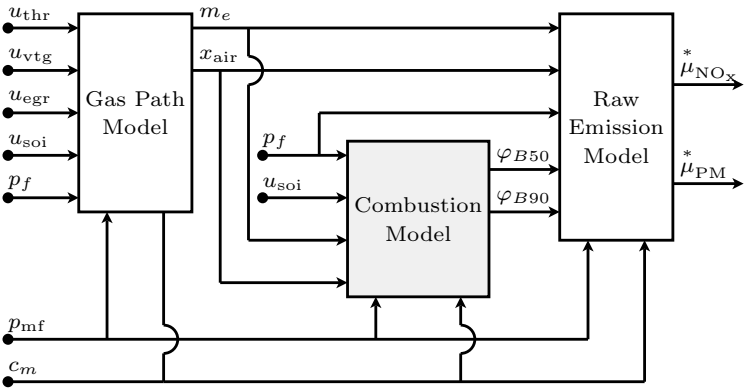

Figure 6.1: Interactions of the three models: virtual sensor application

where $\overset{*}{m}_{\text{hfm}}$ is the intake air mass flow sensor signal, m_2 the mass in the intake manifold, and $\overset{*}{m}_{e,\text{in}}$ the mass flow into the engine. The burnt gas fraction of the EGR mass flow is estimated using the air/fuel ratio signal λ. The conversion from air/fuel ratio to burnt gas fraction is defined as follows:

$$x_{\text{bg}} = \frac{\sigma_0 + 1}{\lambda \cdot \sigma_0 + 1}, \tag{6.2}$$

where σ_0 is the stoichiometric air/fuel ratio. The mass flow into the engine can be estimated using the volumetric pump approach (for details see Section 7.1.2). The mass in the intake manifold is calculated using the ideal gas law. If the temperature in the intake manifold ϑ_2 is assumed to be slowly varying, the derivative of the mass can be estimated as

$$\frac{d}{dt} m_2 = \frac{d}{dt} p_2 \cdot \frac{V_2}{R \cdot \vartheta_2}, \tag{6.3}$$

where $\frac{d}{dt} p_2$ is the derivative of the intake manifold pressure signal, V_2 the manifold volume, and R the gas constant. Alternatively, the EGR mass flow can be estimated modeling the EGR valve as a compressible flow restriction element. Then, the mass flow trough the throttle ($\approx \overset{*}{m}_{\text{hfm}}$) is estimated using Eqs. (6.1) and (6.3). The intake air mass flow sensor is not needed in this case.

The internal residual gas mass m_{rg} is estimated as follows:

$$m_{\text{rg}} = \frac{p_3 \cdot V_c}{R \cdot \vartheta_3}, \tag{6.4}$$

where p_3 is the exhaust manifold pressure, ϑ_3 the engine-out temperature, V_c the top dead center cylinder volume, and R the gas constant of the

exhaust gas. The burnt gas fraction of the residual gas mass is calculated using Eq. (6.2). The cylinder charge at intake valve closing is composed of intake air mass, external, and internal EGR mass. Due to the discretized operation of the engine, signal delays must be considered as well. Details on the in-cylinder time delays are discussed in Chapter 7.

The following sensors signals must be available to estimate the cylinder charge:

- intake mass flow sensor,
- pressure sensor in the intake manifold,
- pressure sensor in the exhaust manifold,
- temperature sensor in the intake manifold,
- temperature sensor in the exhaust manifold,
- air/fuel-ratio sensor,
- engine speed.

If no exhaust manifold pressure pressure and temperature sensors are available, the high-pressure gas path must be modeled as well. In addition, the turbine mass flow must be calculated. The equations needed are discussed in Appendix B.5. The exhaust temperature could be estimated using the approach presented in Chapter 7. To simplify the model, the residual gas mass could be estimated as a constant factor of the in-cylinder mass.

6.2 Combustion Model

In addition, a combustion model is generated. The combustion model estimates the combustion center and the location of the 90% fuel mass burnt. This model is necessary if no cylinder pressure sensor signal is available. The structure of the combustion model is similar to the emission model. Again, the model is formulated as an extended quasi-static approach using the same methodology as for the REM. The combustion center is calculated as follows:

$$\varphi_{B50} = u_{\text{soi}} + \Delta\varphi_{B50}. \tag{6.5}$$

where u_{soi} is the start of injection angle and $\Delta\varphi_{B50}$ represents the duration between start of injection and location of 50% fuel mass burnt expressed in crank angle degrees. Then, $\Delta\varphi_{B50}$ is estimated as

$$\Delta\varphi_{B50} = \gamma_{\Delta\varphi_{B50}} \cdot \Delta\varphi_{B50_0}, \tag{6.6}$$

where $\Delta\varphi_{B50_0}$ is the mapped quasi-static value and $\gamma_{\Delta\varphi_{B50}}$ the correction factor. The correction factor is a function of the operating point, the cylinder mass m_e, the air fraction at intake valve closing x_{air}, and the fuel rail pressure p_{rail}

$$\gamma_{\Delta\varphi_{B50}} = f(c_m, p_{\text{mf}}, \gamma_{m_e}, \gamma_{x_{\text{air}}}, \gamma_{p_f}). \tag{6.7}$$

The functional coherences are derived again by the symbolic regression algorithm. The location of 90% fuel mass burnt is estimated similarly as

$$\varphi_{B90} = u_{\text{soi}} + \Delta\varphi_{B90}. \tag{6.8}$$

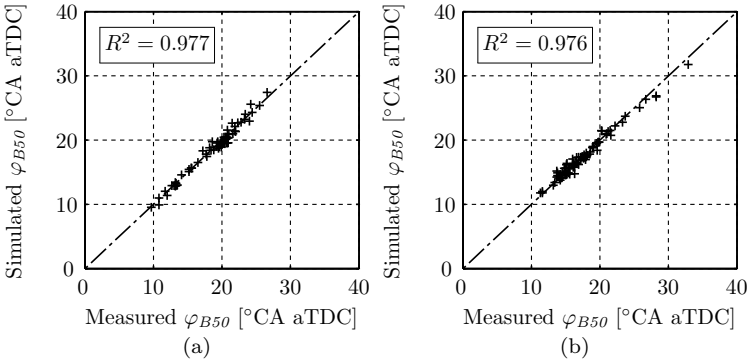

Figure 6.2: Regression plot of the combustion center: LD (a) and HD (b) engine type

Then, $\Delta\varphi_{B90}$ is calculated as

$$\Delta\varphi_{B90} = \gamma_{\Delta\varphi_{B90}} \cdot \Delta\varphi_{B90_0}, \tag{6.9}$$

where the correction factor $\gamma_{\Delta\varphi_{B90}}$ is estimated as

$$\gamma_{\Delta\varphi_{B90}} = f(c_m, p_{\mathrm{mf}}, \gamma_{m_e}, \gamma_{x_{\mathrm{air}}}, \gamma_{p_f}, \gamma_{u_{\mathrm{soi}}}). \tag{6.10}$$

If necessary, other combustion variables such as peak pressure, maximum heat release rate, or location of 10% fuel mass burnt can be estimated analogously. To avoid very large correction factors, all crank angle based signals are expressed as crank angle after 20 ° bTDC.

The following ECU signals must be provided to estimate the combustion characteristic variables start of injection, fuel rail pressure, injected fuel mass, and engine speed. The other required signals (m_e, x_{air}) are estimated by the cylinder charge model.

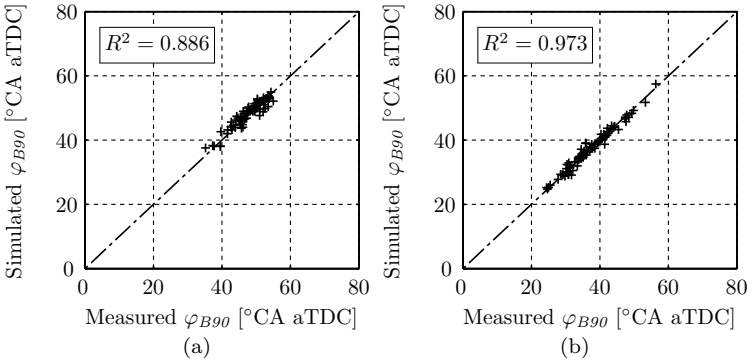

Figure 6.3: Regression plot of the combustion end: LD (a) and HD (b) engine type

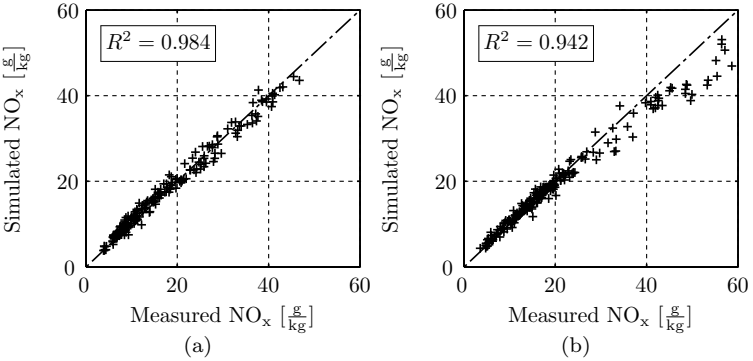

Figure 6.4: Regression plot of the NO_x emission model coupled with the combustion model: LD (a) and HD (b) engine type without using in-cylinder pressure sensors

The simulation results of the combustion model show a good correlation with the static measurement data. Figures 6.2 and 6.3 show the results of the combustion center and combustion end estimation for the light-duty (LD) and the heavy-duty (HD) engine types. The regression of the combustion end is worse due to higher measurement and pressure trace evaluation errors. Overall, the model performs better on the HD engine

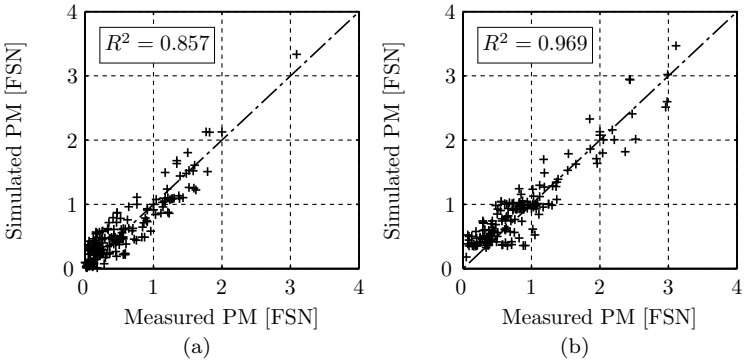

Figure 6.5: Regression plot of the PM emission model coupled with the combustion model: LD (a) and HD (b) engine type without using in-cylinder pressure sensors

data set. This fact can be explained again by the two different base maps used for the LD engine measurements.

Figures 6.4 and 6.5 show the results of the NO_x and PM emission models coupled with the combustion model for the light-duty and the heavy-duty engine types. The performance of the total model is comparable to the results of the emission model only. Therefore, the estimation of the combustion center and combustion end can be used replace the cylinder pressure sensor. In the next section, simulation results obtained during transient operation are shown.

6.3 Simulations and Results

The extended quasi-static model trained on static measurement data is then tested with the same parameters during transient operating conditions to show its extrapolation capabilities. All the transient results shown are measurement data from the light-duty engine.

The transient simulations are conducted together with the cylinder charge and the combustion model to estimate the mass composition at intake valve closing and the combustion characteristics, respectively. The results presented next demonstrate the possibility of using the three models combined as a virtual raw emission sensor.

Figure 6.6 shows a comparison between measurement data and simulation results of the combustion model during a load step. Due to the smaller amount of air mass in the cylinder, the combustion process takes longer during the transient phase. However, the combustion model is able to predict these deviations from the base map as represented by the dashed line. The combustion end is more sensitive to the cylinder charge mass and composition. As the EGR valve is oscillating at the end of the load step, the combustion end oscillates as well. Since the controller of the engine was still under development, the transient behavior of the EGR controller

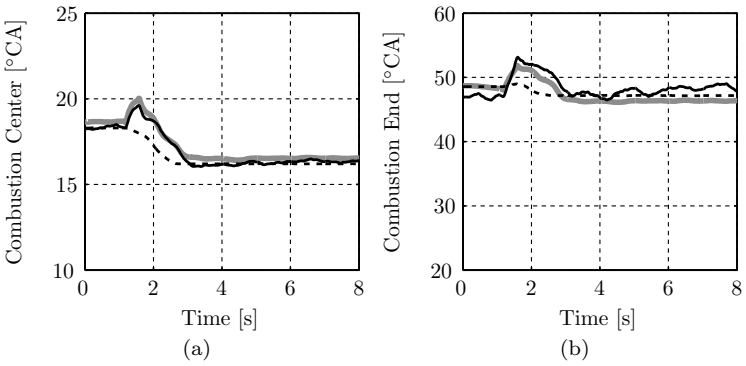

Figure 6.6: Comparison of measurement data and simulation results of the combustion center (a) and combustion end (b) during a load step from 20% to 80% at 2250 rpm, measurement (black), combustion model (gray), quasi-static simulation (dashed);

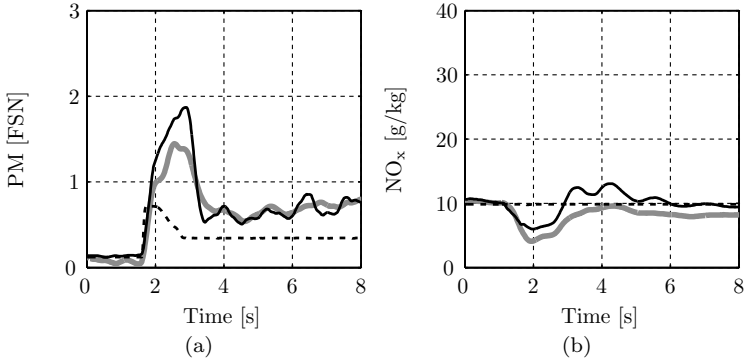

Figure 6.7: Comparison of simulation results and measurement data of PM (a) and NO_x (b) emissions during a load step from 20% to 80% at 2250 rpm, measurement (black), raw emission model (gray), quasi-static simulation (dashed)

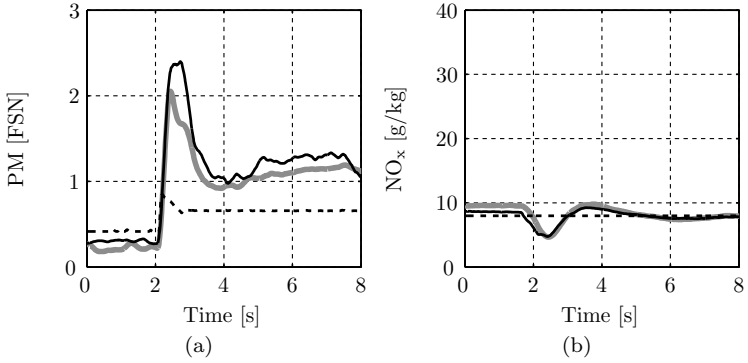

Figure 6.8: Comparison of simulation results and measurement data of PM (a) and NO_x (b) emissions during a load step from 20% to 80% at 2750 rpm, measurement (black), raw emission model (gray), quasi-static simulation (dashed)

is not optimized yet, which explains these oscillations.

Figure 6.7 shows the performance of the REM during a load step from 20% to 80% at 2250 rpm. The results of the simulation agree well with the measurement data. During the turbolag phase, the amount of PM emissions detected is approximately five times higher. Nevertheless, the

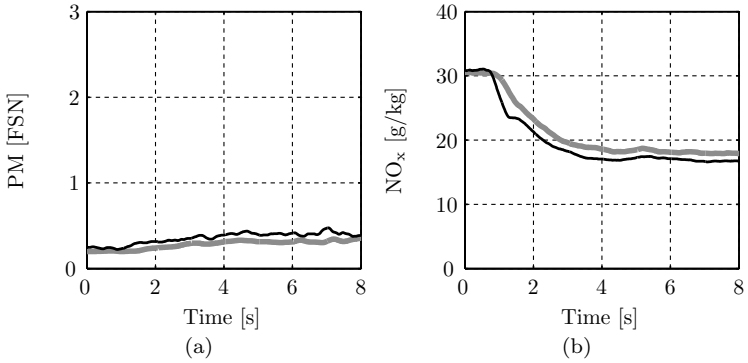

Figure 6.9: Comparison of simulation results and measurement data of PM (a) and NO_x (b) emissions during an EGR-rate step from 0 to 10%, measurement (black), raw emission model (gray)

emission model is able to predict these deviations. In this phase, the NO_x emissions are lower than in static operation due to the reduced amount of oxygen available during combustion.

The transient characteristics of the investigated engine are simular to results reported in [36]. The oscillation of the NO_x emission observable after the load step are due to the oscillating EGR valve. However, the model is able to predict these oscillations for both species of engine-out emissions. In addition, after the first two seconds of the load a static offset remains. This effect can be explained by the fact that the EGR mass was different from that in the stored base map. Nevertheless, the model is able to predict these static offsets from the base map as well.

Figure 6.8 shows the performance of the REM during a load step from 20% to 80% at a higher speed, namely 2750 rpm. During the turbolag phase, the amount of PM emissions detected is again significantly higher. Nevertheless, the emission model is able to predict the measured load step

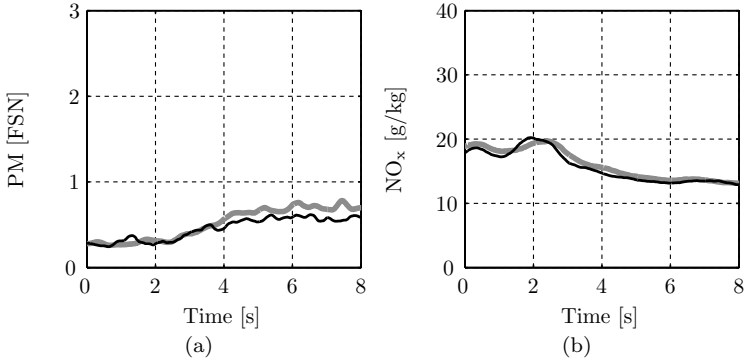

Figure 6.10: Comparison of simulation results and measurement data of PM (a) and NO_x (b) emissions during a boost pressure step from 2.1 to 1.7 bar, measurement (black), raw emission model (gray)

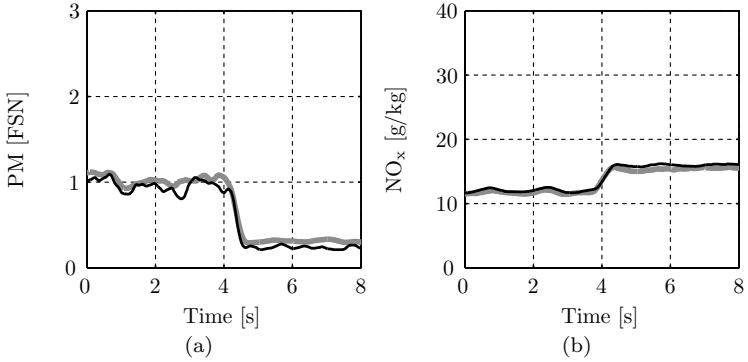

Figure 6.11: Comparison of simulation results and measurement data of PM (a) and NO_x (b) emissions during a fuel rail pressure step from 600 to 800 bar, measurement (black), raw emission model (gray)

very well.

Figures 6.9 – 6.12 show simulation results of actuator steps. The actuator steps are carried out at a 60% load and an engine speed of 2000 rpm. The gas path actuators (EGR valve and turbine actuator) influence the boundary condition of the combustion dynamically. The slow increase in

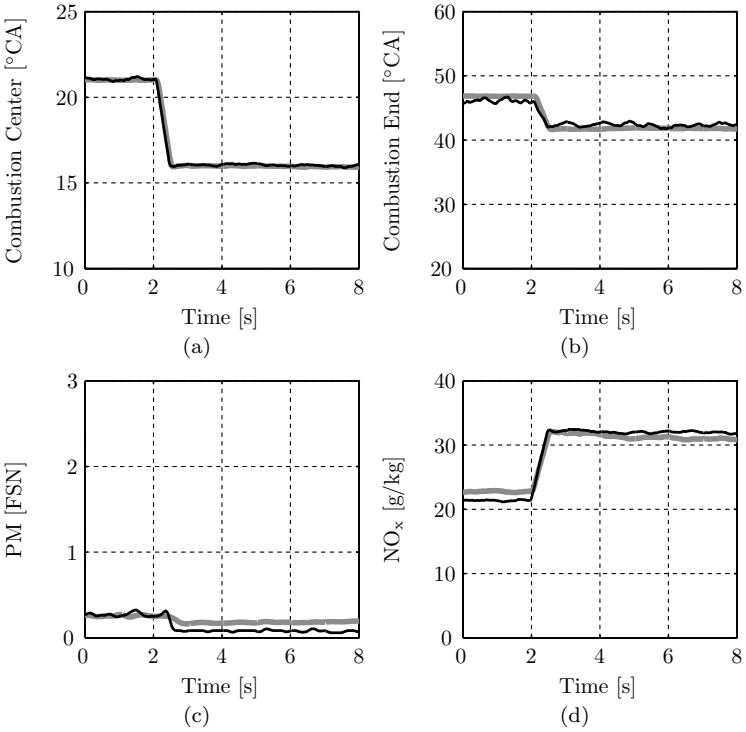

Figure 6.12: Comparison of simulation results and measurement data of combustion center (a), combustion end (b), PM emissions (c), and NO_x emissions (d) during a start of injection step from 0 to 5° CA bTDC, measurement (black), raw emission model (gray)

boost pressure due to the turbolag is evident in the emission data as well. The PM emissions are more sensitive to a lower boost pressure than the NO_x emissions. The higher EGR rate reduces the NO_x emissions by one-half. The mixing dynamics of the intake receiver and the EGR controller significantly influence the EGR mass at intake valve closing. In contrast, the very fast injection actuators also cause a step in the emissions and the combustion characteristics as shown in Figure 6.12. The only relevant

dynamics are the exhaust path delay time and the gas mixing process in the exhaust system.

6.4 Summary and Discussion

This chapter showed a potential application of the raw emission model as a virtual sensor. The raw emission model is embedded in a simple gas path and combustion model. The combination of the three models allows an estimation of the raw emissions in transient operating conditions.

Simulation results of the three models are compared to measurement data. The extended quasi-static approach is able to predict the quantities of the raw emissions and the combustion characteristics during various transients. Hence the extrapolation capability of the control-oriented model is shown. Another important observation, which can be seen is that the combustion and emission formation can be treated as quasi-static, but only if all relevant boundary conditions of the combustion such as cylinder charge composition are considered. Thus all the combustion and raw emission models can be calibrated with measurement data obtained from static operating condition. The requirements for the test bench are thus much lower, and no fast exhaust gas analyzers are necessary.

In addition, the usage of the combustion and cylinder charge model does not significantly degrade the performance of the emission model.

Chapter 7

Application II: Optimal Actuator Controls

In the second application scenario of the raw emission model derived, optimal controls for the engine actuators are investigated. The most important transient operation for a diesel engine is a load step [37]. During acceleration phases, the engine shows slower dynamics due to the relatively large inertia of the drivetrain and the vehicle mass. As already mentioned in the introduction, emission peaks occur during the transient operation of diesel engines. In this chapter, optimal actuator controls are derived to reduce these peaks and to increase the driveability of the vehicle. The driveability of the vehicle is a measure of how fast the engine can change from a low-load to a high-load operating point as perceived by the driver.

The chapter is structured as follows: First, the enveloping structure of the raw emission model is presented in Section 7.1. The gas path model is represented by a so-called mean-value approach.

In Section 7.2 a feedforward injection controller is introduced to eliminate the path constraints of the optimal control problem. The numerical

optimization procedure based on a direct shooting method is discussed in Section 7.3. To demonstrate the capabilities of the method proposed, it is applied for three test cases introduced at the end of Section 7.3. Two of these test cases are focused on the reduction of transient emission levels, while the third test case targets the improvement of the driveability of the vehicle while not increasing the emission values significantly.

The results of the three optimal control problems are presented in Section 7.4.

7.1 Control-Oriented Engine Model

The emission model derived in Chapter 5 is used together with a state-of-the-art mean-value engine model (MVEM) representing the engine gas path dynamics. Additionally, the MVEM provides the transient boundary conditions such as boost pressure and EGR rate for the combustion and the emission model. The MVEM approach is physics-oriented, i.e., it can predict the engine behavior in operating points not included in the measured data set. During the optimization process the actuator inputs can vary in a wide range. Therefore, all the engine component limits must be represented by the model to guarantee a physically meaningful output for arbitrary input signals. Otherwise, the optimization can converge to unrealistic engine operating areas. In the next subsections, selected parts of the mean-value engine model are described in more detail. The remaining components are modeled in accordance with [35]. The detailed equations of these components can be found in Appendix B.

7.1.1 Gas Path Model

The basic part of the gas path system is the receiver block. It has a fixed volume, and its states, such as temperature and pressure, are assumed to be constant over the entire volume (lumped-parameter assumption). The other main dynamics are the engine inertia, the turbocharger inertias, and the actuator dynamics.

Two kinds of flow restriction elements are considered. The air filter, the intercooler, the EGR cooler, and the oxidation catalyst are modeled as incompressible flow restrictions since the gas velocity through these devices is rather low. Details are presented in Appendices B.1 and B.2. The temperature out of the coolers is modeled using the model described in Appendix B.3.

The turbocharger is modeled in accordance with [35] and [38]. The detailed equations can be found in Appendices B.4 and B.5. During transient operation, the pressure ratio over the compressor can become quite large, which causes the compressor to surge. When this condition occurs, the mass flow through the compressor is set to zero, and the derivative of the mass flow is limited to adequately represent the surge condition. In its low-speed regime, the compressor is modeled as an orifice. A smooth change over the two regimes is implemented.

In the gas path a novel receiver approach is introduced to represent the burnt gas fraction in the receiver system more accurately. The approach is discussed in the next subsection.

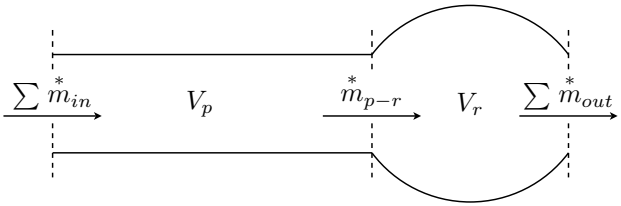

Figure 7.1: Illustration of the pipe receiver model

Pipe Receiver

Beside the standard receiver block presented in Appendix B.8, a novel receiver model including a transport delay for the burnt gas fraction is implemented (see Fig. 7.1). This additional delay allows a more realistic representation of the burnt gas fronts traveling through the receiver system. Due to the high sensitivity of the emissions to the amount of burnt gas in the cylinder at intake valve closing, the lumped value assumption is not satisfactory for the burnt gas fraction. The transport delays for the intake and exhaust manifolds depend on the operating point. These delays are in the range of 50 - 150 ms [39]. The pressure and temperature are still modeled as lumped values. The pipe volume and the receiver volume are defined as follows:

$$V_p = V_{\text{tot}} \cdot r_p \tag{7.1}$$

$$V_r = V_{\text{tot}} \cdot (1 - r_p), \tag{7.2}$$

where V_{tot} is the total volume and r_p the pipe volume fraction. The total volume of the pipe receiver can be derived directly from the design. The

pipe volume fraction is estimated based on the measured delay times. Since the pressure and the temperature are modeled as lumped parameters and if the different specific gas constants of air and burnt gases are neglected, the following simplification is valid

$$\frac{m_r}{m_p} = \frac{V_r}{V_p}, \tag{7.3}$$

where m_r is the mass in the receiver part and m_p the mass in the pipe. The receiver system equations thus consist of two mass balances (air mass m_{air} and burnt gas m_{bg}) and one energy balance. The formulation of the differential equation for the temperature derivative is analogous to that of the standard receiver block. The energy balance of the total system is given by

$$\frac{d}{dt}U = \overset{*}{H}_{in} - \overset{*}{H}_{out} + \overset{*}{Q}_{\text{in}}, \tag{7.4}$$

where $\overset{*}{Q}_{\text{in}}$ is a heat flow into or out of the receiver, respectively. The coupling between these three equations is given by the ideal gas law

$$p_r \cdot V_r = m_r \cdot R \cdot \vartheta_r, \tag{7.5}$$

and the following caloric equations

$$U = (m_r + m_p) \cdot c_v \cdot \vartheta_r \tag{7.6}$$

$$\overset{*}{H}_{in} = \sum \overset{*}{m}_{in} \cdot c_p \cdot \vartheta_{in} \tag{7.7}$$

$$\overset{*}{H}_{out} = \sum \overset{*}{m}_{out} \cdot c_p \cdot \vartheta_{out}. \tag{7.8}$$

Transforming (7.4) and using the caloric equations (7.6)-(7.8), the derivative of the temperature is obtained:

$$\frac{d}{dt}\vartheta_r = \frac{\overset{*}{Q}_{in} - \overset{*}{Q}_{out} + \overset{*}{Q}_{in} - c_v \cdot \vartheta_r \cdot \frac{d}{dt} m_r \cdot \left(1 + \frac{V_p}{V_r}\right)}{c_v \cdot m_r \cdot \left(1 + \frac{V_p}{V_r}\right)}. \tag{7.9}$$

The derivative of the mass in the pipe and in the receiver volume can be calculated by

$$\frac{d}{dt} m_p = \sum \overset{*}{m}_{\text{in}} - \overset{*}{m}_{\text{p-r}} \tag{7.10}$$

$$\frac{d}{dt} m_r = \overset{*}{m}_{\text{p-r}} - \sum \overset{*}{m}_{\text{out}} . \tag{7.11}$$

Inserting Eq. (7.10) into Eq. (7.11), substituting $\frac{d}{dt} m_p$ by differentiating (7.3)

$$\frac{d}{dt} m_r = \sum \overset{*}{m}_{\text{in}} - \frac{d}{dt} m_r \cdot \frac{V_p}{V_r} - \sum \overset{*}{m}_{\text{out}}, \tag{7.12}$$

and solving Eq. (7.12) for the derivative of the receiver mass $\frac{d}{dt} m_r$ thus yields

$$\frac{d}{dt} m_r = \frac{\sum \overset{*}{m}_{\text{in}} - \sum \overset{*}{m}_{\text{out}}}{1 + \frac{V_p}{V_r}}. \tag{7.13}$$

The derivative of the burnt gas mass in the receiver is derived similarly as

$$\frac{d}{dt} m_{\text{bg,r}} = x_{\text{bg},\Delta\text{t}} \cdot \overset{*}{m}_{\text{p-r}} - x_{\text{bg,r}} \cdot \sum \overset{*}{m}_{\text{out}}, \tag{7.14}$$

where $x_{\text{bg,r}}$ is the burnt gas ratio in the receiver part. The burnt gas ratio at the intersection between pipe and receiver part $x_{\text{bg},\Delta\text{t}}$ is defined

as follows:

$$x_{\mathrm{bg},\Delta \mathrm{t}} = \frac{\sum \overset{*}{m}_{\mathrm{bg,in}}}{\sum \overset{*}{m}_{\mathrm{in}}} \left(t - \Delta t_d\right). \tag{7.15}$$

The actual transport delay Δt_d is found by solving the following equation

$$\int_{t-\Delta t_d}^{t} \frac{\sum \overset{*}{m}_{\mathrm{in}}\left(\tau\right)}{V_p \cdot \rho_{\mathrm{in}}(\tau)} d\tau = 1, \tag{7.16}$$

where $\rho_{\mathrm{in}}(\tau)$ is the density of the gas at the intake at time τ. The burnt gas ratio in the receiver part is calculated by

$$x_{\mathrm{bg,r}} = \frac{m_{\mathrm{bg,r}}}{m_r}. \tag{7.17}$$

The intake, exhaust, and EGR receivers are modeled as a pipe receiver.

7.1.2 Cylinder Model

The cylinder model used calculates the cylinder mass flow and the mass composition. These variables defines the interaction with the gas path model. In addition, the torque generation, and the engine-out temperature are calculated by the cylinder model.

Since the engine is a discrete working machine, three main time delays need to be considered. However, in the mean-value modeling approach used, the cylinder is modeled as a continuously working device. The three time delay are

- exhaust-to-induction delay ($\Delta t_{\text{ex-in}} = 213^\circ$ CA),
- induction-to-combustion delay ($\Delta t_{\text{in-co}} = 255^\circ$ CA),
- combustion-to-exhaust delay ($\Delta t_{\text{co-ex}} = 251^\circ$ CA),

where the combustion event is defined at top dead center, the induction event where the intake valve is fully open, and the exhaust event where the exhaust valve is fully open, respectively. The induction-to-exhaust delay $\Delta t_{\text{in-ex}}$ is thus 506° CA.

These time delays mainly influence the air/fuel ratio, which is used by the combustion and the emission model.

All input signals of the emission and the combustion model are timed at the combustion event.

Cylinder Mass and Composition

The engine is modeled as a volumetric pump. Therefore, the mass flow into the cylinders can be estimated as follows

$$\overset{*}{m}_{e,\text{in}} = \lambda_l \cdot \frac{V_d \cdot \omega_e \cdot \rho_2}{4\pi}, \tag{7.18}$$

where λ_l is the volumetric efficiency and ρ_2 is the gas density in the intake manifold. The volumetric efficiency is modeled as a function of the mean piston speed c_m and the pressure ratio of the exhaust manifold to the intake manifold pressure in accordance with [35].

$$\lambda_l = (k_{\lambda,0} + k_{\lambda,1} \cdot c_m + k_{\lambda,2} \cdot {c_m}^2) \cdot \frac{r_c - (\frac{p_3}{p_2})^{\frac{1}{\kappa}}}{r_c - 1}, \tag{7.19}$$

where r_c is the compression ratio of the engine. The mass flow out of the cylinder is estimated as the sum of the intake mass and the fuel mass flow

$$\overset{*}{m}_{e,\text{out}} = \overset{*}{m}_{e,\text{in}}\,(t - \Delta t_{\text{in-ex}}) + \overset{*}{m}_f\,(t - \Delta t_{\text{co-ex}}). \tag{7.20}$$

In addition, there remains a internal residual gas mass m_{rg} in the cylinder which is estimated as

$$m_{\mathrm{rg}} = \frac{p_3 \cdot V_c}{R \cdot \vartheta_{e,\mathrm{out}}}, \tag{7.21}$$

where p_3 is the exhaust manifold pressure, $\vartheta_{e,\mathrm{out}}$ the engine-out temperature, V_c the top dead center cylinder volume, and R the specific gas constant of the exhaust gas. The cylinder charge at intake valve closing is composed of intake air, external and internal EGR. The mass composition in one cylinder at the induction event is

$$\begin{aligned} m_{\mathrm{air,in}} &= (1 - x_{\mathrm{bg,in}}) \cdot \overset{*}{m}_{e,\mathrm{in}} \cdot h_{\mathrm{cyl}} \\ &\quad + (1 - x_{\mathrm{bg,out}}(t - \Delta t_{\text{ex-in}})) \cdot m_{\mathrm{rg}}(t - \Delta t_{\text{ex-in}}), \end{aligned} \tag{7.22}$$

$$\begin{aligned} m_{\mathrm{bg,in}} &= x_{\mathrm{bg,in}} \cdot \overset{*}{m}_{e,\mathrm{in}} \cdot h_{\mathrm{cyl}} \\ &\quad + x_{\mathrm{bg,out}}(t - \Delta t_{\text{ex-in}}) \cdot m_{\mathrm{rg}}(t - \Delta t_{\text{ex-in}}), \end{aligned} \tag{7.23}$$

where h_{cyl} is defined as

$$h_{\mathrm{cyl}} = \frac{4\pi}{n_{\mathrm{cyl}} \cdot \omega_e}. \tag{7.24}$$

The mass composition in one cylinder at the combustion event (after the injected fuel is burnt) is estimated as

$$m_{\mathrm{air,co}} = m_{\mathrm{air,in}}(t - \Delta t_{\text{in-co}}) - m_f \cdot \sigma_0 \tag{7.25}$$

$$m_{\mathrm{bg,co}} = m_{\mathrm{bg,ind}}(t - \Delta t_{\text{in-co}}) + m_f \cdot (1 + \sigma_0) \tag{7.26}$$

where σ_0 is the stoichiometric air/fuel ratio.

The burnt gas ratio at the combustion event and at the engine-out is

then calculated as

$$x_{\mathrm{bg,co}} = \frac{m_{\mathrm{bg,co}}}{m_{\mathrm{air,co}} + m_{\mathrm{bg,co}}} \tag{7.27}$$

$$x_{\mathrm{bg,out}} = x_{\mathrm{bg,co}}(t - \Delta t_{\text{co-ex}}). \tag{7.28}$$

Engine Torque

The engine torque is estimated using a Willans approach [40], where the mean effective pressure p_{me} is defined as follows:

$$p_{\mathrm{me}} = e \cdot p_{\mathrm{mf}} - p_{\mathrm{m0}}, \tag{7.29}$$

where p_{mf} is the fuel mean pressure and p_{m0} represents the losses. The fuel mean pressure is calculated using Eq. (5.2). The pressure losses are estimated as the sum of the gas exchange losses $p_{\mathrm{m0,g}}$, the engine friction $p_{\mathrm{m0,fr}}$, and the power needed by the auxiliary devices $p_{\mathrm{m0,r}}$, mainly the high-pressure rail pump.

$$p_{\mathrm{m0}} = p_{\mathrm{m0,fr}} + p_{\mathrm{m0,g}} + p_{\mathrm{m0,r}}. \tag{7.30}$$

The three loss terms are estimated as

$$p_{\mathrm{m0,fr}} = k_{\mathrm{fr},1} \cdot \omega_e^2 + k_{\mathrm{fr},2} \cdot \omega_e + k_{\mathrm{fr},3} + k_{\mathrm{fr},4} \cdot p_{\mathrm{mf}} \tag{7.31}$$

$$p_{\mathrm{m0,g}} = p_3 - p_2 - k_{\mathrm{g}} \tag{7.32}$$

$$p_{\mathrm{m0,r}} = \frac{\overset{*}{m}_f \cdot p_f \cdot 4 \cdot \pi}{\eta_{\mathrm{hpp}} \cdot \rho_f \cdot \omega_e}, \tag{7.33}$$

where p_f is the actual fuel rail pressure and ρ_f the density of the diesel fuel.

As mentioned, e denotes the thermodynamic efficiency. The following variables influence this efficiency:

- engine speed, parametrized by e_ω,
- boost pressure e_{p2},
- injection timing e_ξ,
- fuel rail pressure e_{fp},
- burnt gas ratio e_{bg}.

The total thermodynamic efficiency is calculated as the product of these factors

$$e = e_\omega \cdot e_{p2} \cdot e_\xi \cdot e_{\text{fp}} \cdot e_{\text{bg}}. \tag{7.34}$$

The individual factors are approximated as follows:

$$\begin{aligned}
e_\omega &= e_{\omega,\text{opt}} - k_\omega \cdot (\omega - \omega_{\text{opt}})^2 && (7.35)\\
e_{p2} &= 1 - k_{p2} \cdot \left(p_2 \left(t - \Delta t_{\text{in-co}}\right) - p_{2,\text{opt}}(\omega_e, \overset{*}{m}_f) \right)^2 && (7.36)\\
e_\xi &= 1 - k_\xi \cdot \left((u_{\text{soi}} - u_{\text{soi,opt}}(\omega_e, \overset{*}{m}_f) \right)^2 && (7.37)\\
e_{\text{fp}} &= 1 - k_{\text{fp}} \cdot \left(p_f - p_{f,\text{opt}}(\omega_e, \overset{*}{m}_f) \right)^2 && (7.38)\\
e_{\text{bg}} &= 1 - k_{bg,1} \cdot (1 + k_{bg,2} \cdot \omega_e) \cdot x_{\text{bg,co}}^2. && (7.39)
\end{aligned}$$

The intake manifold pressure signal and the burnt gas ratio at the intake valve closing are delayed by $\Delta t_{\text{in-co}}$. The best efficiency is defined by $e_{\omega,\text{opt}}$.

The optimal values ($p_{2,\mathrm{opt}}$, $u_{\mathrm{soi,opt}}$, $p_{f,\mathrm{opt}}$) depend on the operating point and are stored in maps.

Engine Exhaust Temperature

Since the specific heat capacity c_p of air and burnt gases (air/fuel ratio equal to one) varies significantly with temperature, the specific heat capacity is approximated as a linear function of the gas temperature ϑ. The specific heat capacity of the mixed gas is calculated by weighting the two values according to the exhaust gas mass ratio

$$\begin{aligned} c_p =& x_{\mathrm{bg}} \cdot (999.2 \tfrac{\mathrm{J}}{\mathrm{kg \cdot K}} + 0.240 \tfrac{\mathrm{J}}{\mathrm{kg}} \cdot \vartheta) \\ &+ (1 - x_{\mathrm{bg}}) \cdot (965.5 \tfrac{\mathrm{J}}{\mathrm{kg \cdot K}} + 0.152 \tfrac{\mathrm{J}}{\mathrm{kg}} \cdot \vartheta). \end{aligned} \tag{7.40}$$

The error in the typical exhaust gas temperature interval is below 0.1%. The enthalpy balance over the cylinder can be estimated as follows:

$$\begin{aligned} \overset{*}{H}_{e,\mathrm{out}} &= \overset{*}{H}_{e,\mathrm{in}} \, (t - \Delta t_{\text{in-ex}}) \\ &\quad + k_\vartheta \cdot (1 - e(t - \Delta t_{\text{co-ex}})) \cdot H_l \cdot \overset{*}{m}_f \, (t - \Delta t_{\text{co-ex}}), \end{aligned} \tag{7.41}$$

where k_ϑ is a function of the current operating point quantifying how much of the loss energy is diverted to the exhaust gas. The other parts are heat losses to the cylinder walls:

$$\overset{*}{H}_{e,\mathrm{in}} = c_{p,\mathrm{in}} \cdot \overset{*}{m}_{e,\mathrm{in}} \cdot \vartheta_2 \tag{7.42}$$

$$\overset{*}{H}_{e,\mathrm{out}} = c_{p,\mathrm{out}} \cdot \overset{*}{m}_{e,\mathrm{out}} \cdot \vartheta_{\mathrm{e,out}} \tag{7.43}$$

Equation (7.41) is solved for the engine-out temperature $\vartheta_{\mathrm{e,out}}$. Figure

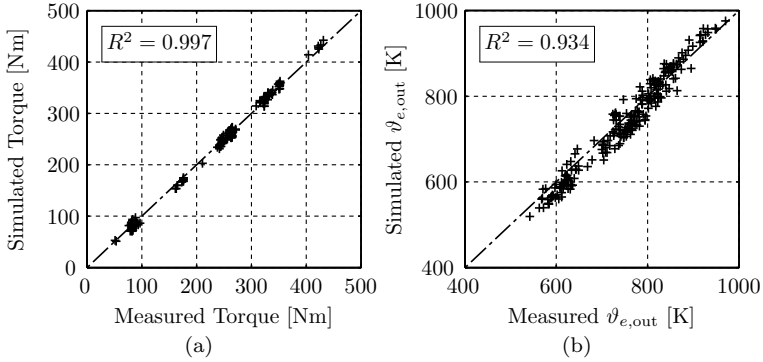

Figure 7.2: Comparison of simulation results and static measurement data: engine torque (a), engine exhaust temperature (b)

7.2 shows a comparison of measurement data and simulation results of the torque generation and engine-out temperature model in steady-state conditions. The simulation agrees well with the measurement data.

During transient operation, the engine-out temperature varies due to some additional heat flux from or to the cylinder walls. This effect is described by an additional lag compensator element. The parameters of the lag compensator are a function of the exhaust mass flow, whose static gain is equal to one. The transfer function is

$$G(s) = \frac{a \cdot s + 1}{b \cdot s + 1} \tag{7.44}$$

where the two parameters are defined as

$$a = \frac{k_{\vartheta,1} \cdot \overset{*}{m}_{e,\mathrm{out}}}{\overset{*}{m}_{e,\mathrm{out}} - k_{\vartheta,2}} \tag{7.45}$$

$$b = \frac{k_{\vartheta,1} \cdot \overset{*}{m}_{e,\mathrm{out}}}{\overset{*}{m}_{e,\mathrm{out}} + k_{\vartheta,2}} \tag{7.46}$$

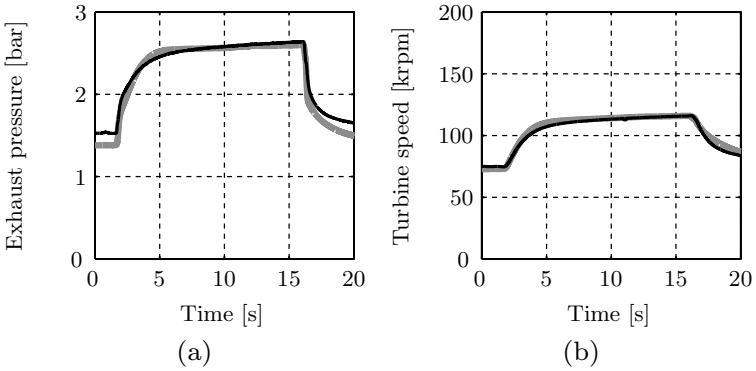

Figure 7.3: Comparison of simulation results (gray) and measurement data (black) during a load step and a load drop at constant engine speed: exhaust manifold pressure (a), turbocharger speed (b)

Figure 7.3 shows a comparison of measurement data and simulation results of the MVEM model during two load steps. The slow increase of the turbocharger speed after the first load step from 5 to 15 seconds can be explained by the lag element used to calculate the engine-out temperature.

7.1.3 Actuator Models

The throttle, the EGR valve, and the variable turbine geometry all influence the gas path (see Fig. 1.1). The injection is determined by the start of injection, the injection duration, the delivery valve, and the control valve of the fuel rail pressure system. The other system inputs, such as the control valves of the cooling circuits, are not considered in the model. The start of injection and the injection duration are not showing any actuator dynamics. These two inputs act as feedtrough terms to the torque and emission generation. The other actuators have a dynamic behavior during

transients. These actuator dynamics are modeled as a low-pass and a delay time element in series. The actual actuator position u_{pos} is estimated as

$$u_{\text{pos}} = \frac{1}{\frac{s}{\tau_{\text{act}}} + 1} \cdot e^{-s \cdot \Delta t_{\text{act}}} \cdot u_{\text{des}}, \tag{7.47}$$

where u_{des} is the desired actuator position, τ_{act} the time constant of the low-pass part, and Δt_{act} the delay time. Table 7.1 shows the values used for the time constant and the time delay of each actuator.

Figure 7.4 shows the common-rail system and its components. The common-rail is fed by a high-pressure pump, which is controlled by a delivery control valve. This main control loop is operated by a PID controller supported by a feedforward controller. If the pressure in the rail is too high, an additional control valve is used to control the flow from the common-rail back to the tank. The pressure control valve is fully closed under normal conditions to reduce pumping losses. If the desired fuel rail pressure is lower than the actual fuel rail pressure, a PID controller operates the valve.

The pressure change in the rail is calculated as follows:

$$\frac{d}{dt} p_f = \frac{K_f}{V_{\text{rail}} \cdot \rho_f} \cdot (\overset{*}{m}_{\text{hpp}} - \overset{*}{m}_f - \overset{*}{m}_{\text{pcv}}), \tag{7.48}$$

Table 7.1: Actuator time delay and time constants used

Actuator	Time Constant τ_{act}	Time Delay Δt_{act}
EGR valve	0.15	0.05
VTG actuator position	0.08	0.05
Throttle	0.15	0.05
Delivery control valve	0.05	0.04
Pressure control valve	0.01	0.01

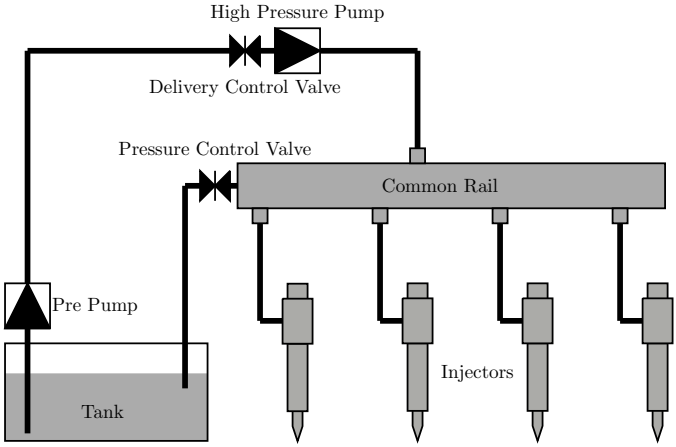

Figure 7.4: Illustration of the fuel injection system

where K_f is the bulk modulus of elasticity, ρ_f the fuel density, V_{rail} the rail volume, $\overset{*}{m}_{\text{hpp}}$ the mass flow delivered by the pump, $\overset{*}{m}_{\text{pcv}}$ the mass flow through the control valve, and $\overset{*}{m}_f$ the mass flow delivered to the injectors. The bulk modulus of elasticity is expressed as [41]

$$K_f = 1.2 \cdot 10^9 \cdot (1 \text{ Pa} + \frac{p_f}{10^9}). \tag{7.49}$$

The mass flow through the high-pressure pump $\overset{*}{m}_{\text{hpp}}$ is calculated as

$$\overset{*}{m}_{\text{hpp}} = \frac{w_e}{4\pi} \cdot V_{\text{hpp}} \cdot \rho_f \cdot \eta_{\text{hpp}}(\omega_e, p_f) \cdot u_{\text{dcv}}, \tag{7.50}$$

where V_{hpp} is the total pump volume and η_{hpp} is the pump efficiency depending on the actual rail pressure and engine speed. The position of the delivery control valve u_{dcv} controls the actual volume flow. The mass

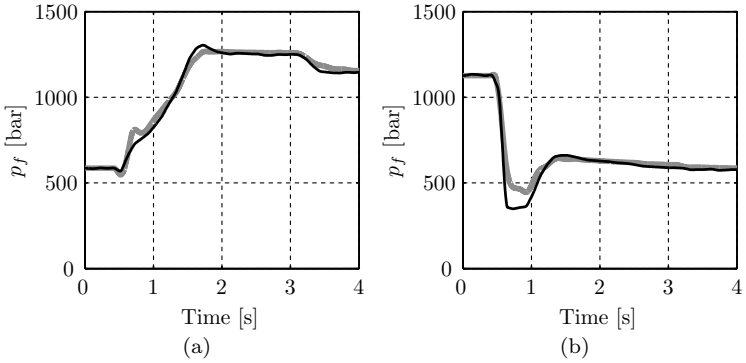

Figure 7.5: Comparison of simulation results and measurement data of the fuel rail pressure control system, measurement (black), simulation (gray) during a pressure step (a) and a pressure drop (b)

flow through the pressure control valve $\overset{*}{m}_{\text{pcv}}$ is estimated as

$$\overset{*}{m}_{\text{pcv}} = A_{\text{eff}}(u_{\text{pcv}}) \cdot \sqrt{2 \cdot p_f \cdot \rho_f}, \tag{7.51}$$

where the effective valve area A_{eff} of the pressure control valve is a function of the control input u_{pcv}. Both valves have an opening and a closing dynamic.

In the further considerations, to simplify the optimal control problem, the desired fuel rail pressure acts directly as a input signal. Clearly, there remains a certain potential for improving the characteristics of the fuel rail system by directly controlling the two valves. Nevertheless, as the dynamics of the fuel rail control system are very fast, the potential for any further optimization is fairly low. Figure 7.5 shows simulation results of two desired fuel rail pressure steps, which clearly shows that the dynamics may not be neglected.

7.2 Feedforward Torque Controller

Typically, the engine speed is required to follow a desired trajectory for a predefined load torque. Since these nonlinear path constraints complicates the optimal control problem, a feedforward controller is introduced to internally fulfill these constraints.

The engine speed constraint is converted to a required engine torque through differentiation. Adding the load torque T_l, the required engine torque $T_{e,\mathrm{req}}$ is derived as

$$T_{e,\mathrm{req}} = T_l + \Theta \cdot \dot{\omega}_e, \tag{7.52}$$

where Θ is the moment of inertia of the drivetrain. The fuel mass flow $\overset{*}{m}_f$ provides a direct feedthrough to the engine torque. The torque model introduced before has to be inverted to calculate the fuel mass flow needed to produce the requested torque. However, the torque model is not directly

Table 7.2: Pseudo-code of the iterative calculation of the fuel mass flow.

```
Calculate loss terms assuming p_mf = 0
Calculate engine efficiencies e_ω and e_bg, set e_p2, e_ξ and e_fp to 1
Calculate m*_f required to achieve the requested torque
while p_me differs from p_me,req more than Tol
    Calculate p_m0,f and p_m0,r using current m*_f estimation
    Calculate efficiencies e_p2, e_ξ and e_fp using current m*_f estimation
    Calculate p_me from current p_mf, e, and p_m0
    if p_me is lower than p_me,req
        Increase m*_f by stepsize
    else
        Halve the stepsize
        Decrease m*_f by stepsize
    end if
end while
```

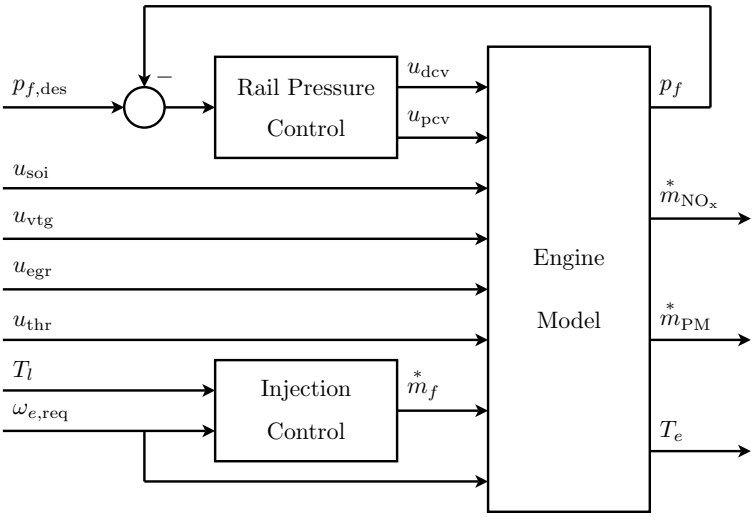

Figure 7.6: Final model structure of the optimal control problem

invertible because the efficiencies e_{p2}, e_{ξ}, and e_{fp} and the loss pressures p_{m0f} and p_{m0r} depend on the fuel mass flow. Therefore, the required fuel mass flow is calculated iteratively. An approximation is supplied for the required fuel mass flow by estimating the drag torque and efficiency of the engine while setting the injection-dependent efficiency factors to unity. Since these factors can never be larger than one, the actual required fuel mass flow is guaranteed to be higher than this approximation. Then, the fuel mass flow is increased stepwise. If the required torque is not yet met, another step is taken. If the required torque has been crossed, the step size is halved. This procedure is repeated until the fuel mass flow has converged within a given tolerance. Table 7.2 shows the pseudo-code of the iterative algorithm. The removal of the output constraints (engine speed) drastically simplifies the optimal control problem. In addition, the dimensionality of the problem is reduced to five or six constrained

inputs. During the simulation, approximately 10% of the calculation time is needed to calculate the correct fuel mass flow. The remaining inputs can be separated into two types. The inputs u_{vtg}, u_{egr}, u_{thr} and $p_{f,\mathrm{des}}$ influence the outputs through the gas path or fuel rail dynamics, respectively, while u_{soi} has a direct feedthrough to the outputs. The optional input engine load T_l is only used in the test case where the driveability is optimized. The five control inputs can be chosen freely respecting the maximal and minimal values of each actuator.

Figure 7.6 shows the final model structure with five inputs, the optional input T_l, and three outputs. The outputs of the model are the two emission values that are subject to legislative limits, and the torque produced.

7.3 Numerical Optimization Procedure

The final model including the gas path model, the raw emission model, the rail pressure controller, and the injection controller is now used to generate optimal actuator trajectories during selected transients.

7.3.1 Formulation of the Optimal Control Problem

Consider a dynamic system for which the states $\mathbf{x}$ are given by

$$\dot{\mathbf{x}} = \mathbf{f}(\mathbf{x}, \mathbf{u}) \tag{7.53}$$

and whose initial state at time t_0 is

$$\mathbf{x}(t_0) = \mathbf{x}_0. \tag{7.54}$$

To formalize the term of optimality, the cost function J is introduced as

$$J = \int_{t_0}^{t_f} L(\mathbf{x}(t), \mathbf{u}(t), t)dt. \tag{7.55}$$

To account for the constraints on states and controls, the formulation is extended by a constraint function

$$\mathbf{G}(\mathbf{x}(t), \mathbf{u}(t)) \geq \mathbf{0} \tag{7.56}$$

grouping all equality and inequality constraints. The objective of the optimal control solution is to find the input $\mathbf{u}_{\text{opt}}(t)$ that minimizes J during the time interval t_0 to t_f.

7.3.2 Choice of Numerical Method

Several methods have been developed to find numerical solutions of optimal control problems [42]:

- dynamic programming,
- direct method,
- indirect method.

Dynamic programming is based on the idea that optimal solutions of subproblems can be used to build the optimal solution of a larger problem. In the case of optimal control, this means that the optimal control input over the whole time interval $[t_0, t_f]$ is split into a set of shorter time intervals which are solved consecutively. If an optimal control solution for a short time interval $[t_x, t_f]$ is found, it must be part of the optimal solution for

the whole interval $[t_0, t_f]$. Using this idea, the optimal control problem is solved backwards. The resulting optimal trajectory is the globally optimal solution within the search space.

However, dynamic programming is subject to the curse of dimensionality [43]. With an increasing dimension in the state-space, the number of state discretization points to be calculated grows exponentially. Therefore, dynamic programming is only suited for problems having a small number of states and inputs. Due to the high dimensionality of the engine model used, the application of dynamic programming is computationally too expensive.

The indirect method is an entirely different approach. The optimization is a minimization of J, subject to the constraints that the system dynamics and the initial condition are fulfilled. Therefore time-varying Lagrange multipliers $\boldsymbol{\lambda}(t)$ are introduced. The resulting *boundary value problem* must be solved numerically. The differential equations for the Lagrange multipliers are often strongly nonlinear. Therefore a good initial guess $\boldsymbol{\lambda}^T(t_0)$ is required due to the often small zones of convergence. In the present case, the cost function used is dependent on the emissions produced. The algebraic expressions linking the cost to the system states are rather complex. Since the model contains delay times, maps, and various discontinuities such as saturations, reformulating and analytically differentiating these terms with respect to the state and control variables is not feasible. However, these differentiations are required to express the differential equations of the Lagrange multipliers. This restriction prevents the use of indirect methods without introducing too many simplifications.

The third class of numerical solutions are direct methods. These methods are based on the strategy of converting the search for an optimal function $\mathbf{u}(t)$ to a parameter optimization problem. These parameters $\mathbf{q}$ approximate the input function $\mathbf{u}(t)$, typically by discretizing it on a time grid as follows:

$$\mathbf{u} = f(t, q). \tag{7.57}$$

Therefore the optimal control inputs can be defined as

$$\mathbf{u}_{\text{opt}}(t) = f(\arg\min_{\mathbf{q}} J) \text{ with } \mathbf{q} \in [\mathbf{u_{lb}}, \mathbf{u_{ub}}], \tag{7.58}$$

where $\mathbf{u_{lb}}$ is the lower and $\mathbf{u_{ub}}$ the upper boundary of the input vector. This formulation represents a finite-dimensional nonlinear programming problem (NLP), for the solution of which there exist powerful algorithms. Notice that the parameter optimization used in direct methods does not use the Lagrange multiplier formulation introduced in the indirect method. In addition, the cost function must not be defined explicitly. Since the number of parameters is proportional to the number of time discretization points, the length of the optimization window is limited to short time intervals. Thus, the solution calculated is not the optimal solution to the original problem, but rather, it is the solution possible under the assumption of discretized input signals.

7.3.3 Solving the Optimal Control Problem

The final optimization problem can be stated as follows. The cost function (7.55) is to be minimized over the parameter vector $\mathbf{q}$, with $\mathbf{q}$ denoting the

discretized values of the five inputs. The path constraint (engine speed) is eliminated using the feedforward injection controller. Additionally, the feedforward controller guarantees the solution to end up in the desired final operating point such that no further cost function term is necessary to penalize any end point deviations.

Since no path constraints are present, the only remaining constraints are those on the five input signals. Table 7.3 lists the input constraints. The EGR valve position and throttle position can only range between 0 and 1, which signify *fully closed* and *fully open*, respectively. The VTG input ranges from 0 to 1, which represent the minimal and maximal angle of the turbine blades, respectively. The fuel rail pressure is limited to 1600 bar as the maximum pressure specified by the manufacturer. Since there are no hard limits for the SOI, the upper limit is chosen as 10° CA bTDC in order to avoid extremely high in-cylinder peak pressures. The load torque is limited to not exceed the maximal torque that the engine can supply.

The direct single shooting method used has several advantages. The handling of any input constraints is straightforward, since the optimal control problem and the ODE problem are solved sequentially. During

Table 7.3: Input and actuator constraints

Actuator	Lower limit	Upper limit	Unit
Throttle (u_{thr})	0	1	[-]
EGR valve (u_{egr})	0	1	[-]
VTG input (u_{vtg})	0	1	[-]
Start of injection (u_{soi})	-	10	[°CA bTDC]
Rail pressure (p_f, des)	-	1600	[bar]
Load torque (T_l)	-	400	[Nm]

the engine model simulation, only valid input signals are used since the input constraints are applied in advance. In addition, few restrictions for the model structure have to be considered. The model can be quite complex including discontinuities, time delays, and nonlinear equations, as long as the cost function can be evaluated for a given set of input signals. Nevertheless, finding a valid solution can be difficult in the case of an unstable system or path constraints present. The elimination of the path constraints by the feedforward injection controller is thus an important step toward finding a solution to the optimal control problem.

To directly solve the optimal control problem, the input needs to be discretized, as mentioned above. The most commonly used way of discretizing optimal control inputs is a stepwise discretization, meaning that the input signal is assumed to be constant over one discretization interval. The main advantage of this discretization is its local support since during each time step, the control signal only depends on one parameter. As an alternative to such a stepwise discretization, a linearly interpolated discretization process could be used. This method does not provide any local support since the input signal of one interval depends on two input parameters. However, providing continuous input signals can be advantageous when the behavior of real input signals is to be represented. A third method is the polynomial interpolation, where the parameters q are nodes defining a polynomial of the order $q-1$. The polynomial interpolation allows meaningful input signals to be with far fewer parameters, but local support is lost completely. Since in the given problem of optimizing an actuator position, steps in the inputs are expected to occur, a step discretization is used. During the optimization of the input trajectories, the discretization

is increased to yield smoother signals and to minimize the influence of the discretization. The resulting optimal trajectories of the larger discretized optimal control problem are used as the initial input trajectories for the finer grid problem. The smallest discretization grid is 100 ms, since a finer grid does not improve the cost function observably. If only a subset of the inputs are optimized, the trajectories of the non-optimized actuators are fixed at their initial values.

The NLP problem is solved using a sequential quadratic programming (SQP) algorithm, which is included in the Optimization Toolbox for MATLAB [44]. The SQP algorithm used to optimize the system requires values of the gradient of the cost function (7.55) with respect to the control input parameters $\mathbf{q}$. Since an algebraic differentiation is not feasible, a finite differencing process is used to approximate the derivative with respect to one component of $\mathbf{q}$. SQP algorithms are an frequently used method due to their fast convergence and robustness while being able to handle both equality and inequality constraints [45]. Similarly to Newton's method, an SQP algorithm solves a series of approximated subproblems, each of which provides a new estimate of the optimal point. The size of the parameter vector $\mathbf{q}$ depends on the number of inputs to be optimized and the discretization of the time. For instance, the number of parameters q is 80 in the load step case where all four inputs (u_{soi}, $p_{f,\mathrm{des}}$, u_{vtg}, u_{egr}) are optimized.

7.3.4 Test Cases

As mentioned in the introduction of this chapter, three different test cases are investigated. The first two are focused on reducing the emission values

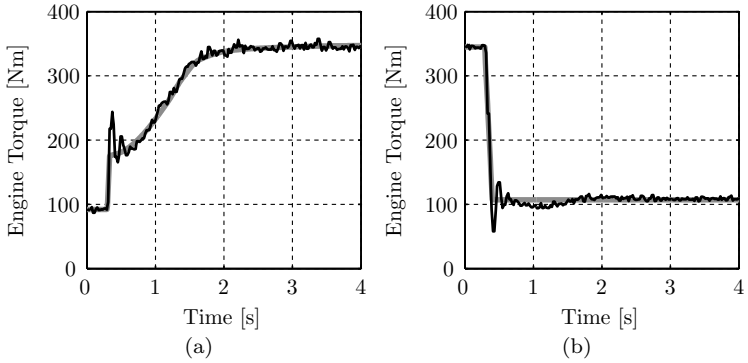

Figure 7.7: Comparison between measured (black) and smoothed (gray) load step: engine torque during the load step at 2250 rpm (a), engine torque during the load drop at 2750 rpm (b).

during a load step and a load drop, respectively. The third test case investigates optimal control inputs to increase the driveability of the vehicle. The initial values of the parameter vector $\mathbf{q}$ defining the system inputs are set equal to those of the smoothed inputs of measured load steps. Figure 7.7a shows a comparison of the smoothed and the real measured engine torque during a load step from 20% to 80% load at 2250 rpm. In the first part of this step, the injected fuel mass rises suddenly. Then the fuel mass flow is limited during the first second of the load step to prevent high PM emissions causing a moderate increase of the engine torque. The load step takes four seconds. The actuator trajectories are optimized between 0.3 and 2.3 seconds. The objective of this first optimal control problem is to minimize NO_x and PM emissions. In the very short transients investigated, a slight increase in fuel consumption is possible, but it is tolerable since its influence on the overall fuel consumption is quite small. Therefore, the cost function is defined as the sum of the integrated PM (m_{PM}) and NO_x

($m_{\mathrm{NO_x}}$) emissions. The particulate mass is weighted with a factor w

$$J = \int_{t_0}^{t_f} (\overset{*}{m}_{\mathrm{NO_x}} + w \cdot \overset{*}{m}_{\mathrm{PM}}) dt. \tag{7.59}$$

The values for the weighting factor are chosen based on European emission standards, which define the maximum allowable emission values of $\mathrm{NO_x}$ and PM. The weighting factor is chosen as the ratio between the two values. Table 7.4 shows the values of w for different European emission standards and different vehicle classes. Since the measurement data are taken from an engine which complies with the EURO IV emission limits, a weighting factor of 10 is chosen. The constraint function used is defined as

$$\mathbf{G}(u_{\mathrm{soi}}, p_{f,\mathrm{des}}, u_{\mathrm{vtg}}, u_{\mathrm{egr}}) \geq \mathbf{0}. \tag{7.60}$$

As a further test, the engine behavior during a load drop from 80% to 20% at 2750 rpm is evaluated. Figure 7.7b shows this test case, representing the typical end of an acceleration phase. In addition to the first load step problem, the throttle position is included during the optimizations. The actuator trajectories are optimized between 0.3 and 1.5 seconds. The same cost function (7.59) is used. The constraint function for the load

Table 7.4: Ratio of allowed $\mathrm{NO_x}$ emissions to allowed PM emissions for various European emission standards.

Emission standard	II	III	IV	V	VI
Passenger	-	10	10	36	16
Light-duty	-	7.8	6.5	56	25
Heavy-duty	22.2	46.7	38.5	175	100

drop test case is defined as

$$\mathbf{G}(u_{\mathrm{soi}}, p_{f,\mathrm{des}}, u_{\mathrm{vtg}}, u_{\mathrm{egr}}, u_{\mathrm{thr}}) \geq \mathbf{0}. \tag{7.61}$$

The objective of the third optimal control problem is to minimize the NO_x and PM emissions while maximizing the crank shaft work delivered by the engine. Again, a load step from 20% to 80% at 2250 rpm is investigated. The measured load step is used as a reference. The cost function is defined as the weighted sum of the PM (m_{PM}) and NO_x ($m_{\mathrm{NO_x}}$) emissions, divided by the fuel mass flow. The particulate mass is weighted with a factor w_1. The second term maximizes the power provided by the engine. A second weighting factor w_2 is introduced

$$J = \int_{t_0}^{t_f} \left(\frac{\overset{*}{m}_{\mathrm{NO_x}} + w_1 \cdot \overset{*}{m}_{\mathrm{PM}}}{\overset{*}{m}_f} + w_2 \cdot \frac{H_l}{T_e \cdot \omega_e} \right) dt. \tag{7.62}$$

The constraint function for this test case additionally includes the load torque T_l

$$\mathbf{G}(u_{\mathrm{soi}}, p_{f,\mathrm{des}}, u_{\mathrm{vtg}}, u_{\mathrm{egr}}, T_l) \geq \mathbf{0}. \tag{7.63}$$

The load step takes four seconds. The trajectories of the actuator inputs and the load torque are optimized between 0.3 and 1.8 seconds.

7.4 Numerical Optimal Control Results

Particular inputs and combinations of input trajectories are optimized, respectively. With this procedure, the potential of each actuator combination for reducing the emission values is evaluated. In the first subsection,

the results of the load step case are shown. In Subsection 7.4.2, the results of the load drop test case are presented. The results of the driveability test case are discussed in Subsection 7.4.3. The measured load steps are used as a reference in all test cases.

7.4.1 Load Step Test Case

Figure 7.8 shows the optimization of the start of injection only. The start of injection is a very fast input which can be changed from one combustion event to the next. Therefore, it would be most suitable for controlling the emission levels during transients. But the potential for reducing the emission is fairly low since the optimized trajectory does not differ much from the reference trajectory. The start of injection is shifted to earlier injection timings during the PM emission peak. The higher NO_x emission levels are compensated in the beginning with later injection timings. At the end of the optimization, the injection starts similarly to the reference

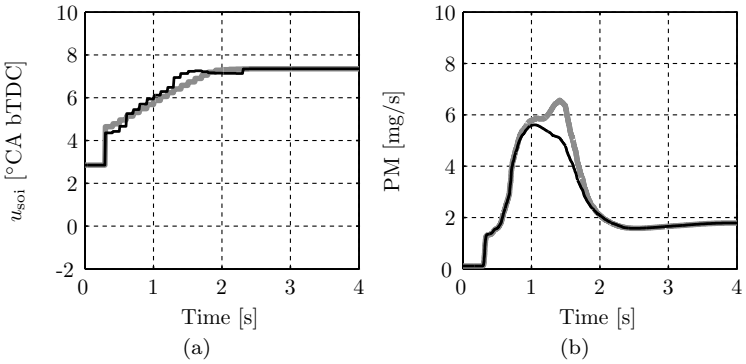

Figure 7.8: Comparison of reference (gray) and optimized (black) trajectories during a load step with an optimized start of injection at constant engine speed: start of injection (a), PM (b).

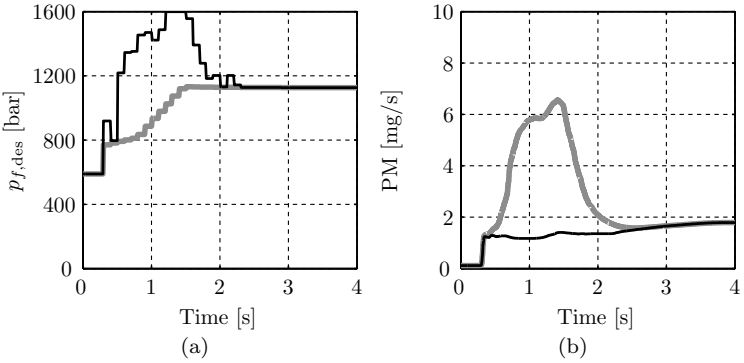

Figure 7.9: Comparison between reference (gray) and optimized (black) trajectories during a load step with an optimized fuel rail pressure at constant engine speed: fuel rail pressure (a), PM (b).

trajectory. Hence, the start of injection of the reference trajectories is optimally designed for the weighting factor of 10 used in a static sense as well. Nevertheless, as the NO_x emission levels are normally lower during a load step than in quasi-static simulations, a certain increase of the NO_x emissions is tolerable to reduce the PM emissions. Therefore, a potential to moderately adjust the start of injection to earlier injection events still exists. The weighting factor must be increased to shift the PM-NO_x trade-off to lower the PM emissions. Figure 7.9 shows the results of the optimized fuel rail pressure. The other inputs are set to their reference values. Shortly after the load step, the desired fuel pressure is increased strongly. This increase results in much lower PM emissions during the entire transient. However, the much higher fuel injection pressure would increase the noise level of the engine significantly. Since the engine combustion noise is neither measured nor modeled, it is neglected in the cost function. Further investigations are necessary on this subject to enhance

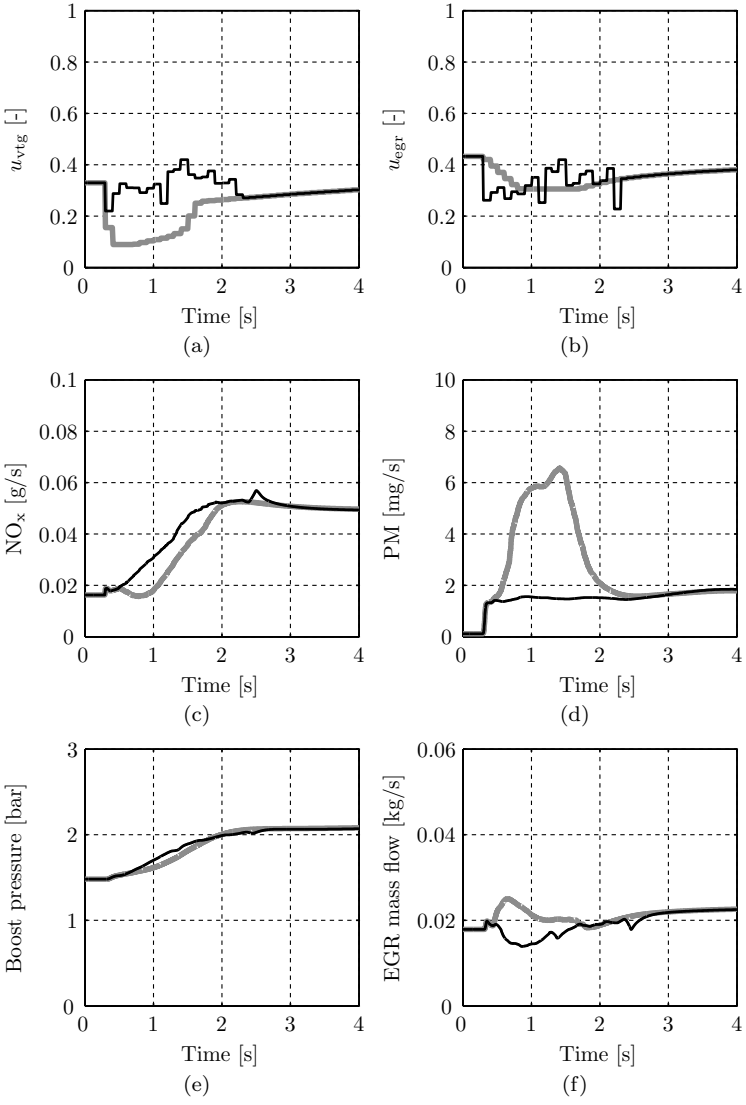

Figure 7.10: Comparison between reference (gray) and optimized (black) trajectories of the gas path actuators during a load step at constant engine speed: VTG actuator position (a), EGR valve position (b), NO_x emissions (c), PM emissions (d), boost pressure (e), and EGR mass flow (f).

the value of the resulting optimized trajectories. The graphs (a) and (b) in Figure 7.10 show the optimized gas path actuator trajectories (u_{vtg}, u_{egr}). Due to the optimized inputs the boost pressure increases faster. A nearly closed EGR valve during the first phase of the load step further increases the air mass in the cylinder. Therefore, the PM emissions are reduced drastically (by 61%), while the NO_x emissions are increased by 21%. This effect is as expected due to the lack of exhaust gas recirculation caused by the nearly closed EGR valve. The NO_x values are higher in almost the entire optimization interval. However, as discussed in relation to previous results, the reference NO_x values are lower than those of the quasi-static simulation. The emission reduction potential is comparable to that reached by the optimized fuel rail pressure.

The fuel consumption in the optimized case is slightly lower than under reference conditions (4% less), which can be explained by the reduced EGR rate. Notice that a weighting factor of 10 leads to approximately equal costs for NO_x and PM emissions in relative terms. Therefore, the trade-off is accepting slightly increased NO_x emissions to reach much lower PM emissions.

Table 7.5 summarizes the potential of improving the control strategy of various actuator combinations. Optimizing only the start of injection shows the lowest benefit. All other combinations lead to drastic reductions of the PM emissions, while increasing the NO_x emissions moderately. The reduction can be reached either by the two gas path actuators EGR valve and VTG actuator position or the fuel rail pressure only, respectively. Obviously, the optimization of all actuators yields the best result. However, optimally controlling all available actuators offers only small advantages in

reducing the emission levels compared to a well-chosen subset of actuators.

Table 7.5: Cost reduction potential of different input combinations for the load step test case

Optimized inputs	m_f [g]	$m_{\mathrm{NO_x}}$ [g]	m_{PM} [mg]
Reference	8.13	0.063	7.630
u_{soi}	8.12 (99%)	0.063 (101%)	6.960 (91%)
$p_{f,\mathrm{des}}$	8.16 (100%)	0.080 (127%)	2.580 (34%)
u_{soi}, $p_{f,\mathrm{des}}$	8.16 (100%)	0.080 (127%)	2.510 (33%)
u_{vtg}, u_{egr}	7.79 (96%)	0.076 (121%)	2.960 (39%)
u_{vtg}, u_{egr}, u_{soi}	7.79 (96%)	0.075 (120%)	2.940 (39%)
u_{soi}, $p_{f,\mathrm{des}}$, u_{vtg}, u_{egr}	8.14 (100%)	0.071 (113%)	2.710 (36%)

7.4.2 Load Drop Test Case

Compared to the load step test case, the emission peaks are generally very low in the load drop case.

In contrast to the first test case, the optimal solution favors the reduction of the NO_x emissions. Nevertheless, the reduction potential is low, especially in absolute terms. Figure 7.11 shows the optimization of the injection inputs (u_{soi}, $p_{f,\mathrm{des}}$) during a load drop. The optimal earlier injection timing shortly after the load drop reduces the PM peak. The lower fuel injection pressure further reduces the NO_x emissions by approximately 25% during the first 500 ms of the load drop. Due to the lean air/fuel ratio, the PM emissions are only slightly increased between 0.5 and 2 seconds.

Figure 7.12 shows the trajectories of the optimized gas path actuators in combination with an optimized start of injection timing. In the optimal solution, the EGR valve and the VTG area are fully open in the first period of the load drop. The boost pressure thus reaches the desired boost

pressure of the new operating point faster. The throttle is moderately closed (≈20%) to further accelerate the reduction of the boost pressure during the load drop. The injection is used to eliminate the PM emission peak during the first 100 ms of the load drop. Late injection timings are optimal for reducing the NO_x emissions until the boost pressure reaches the desired value. Again, due to the lean air/fuel ratio the PM emission are not increased considerably. At the end of the load drop the optimization

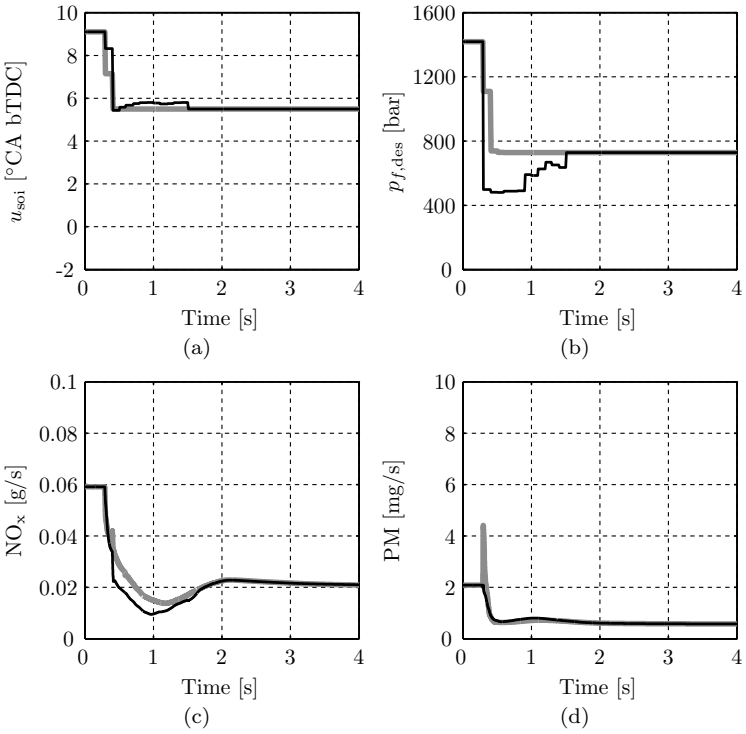

Figure 7.11: Comparison of reference (gray) and optimized (black) trajectories with optimized injection parameters during the load drop at constant engine speed: start of injection (a), fuel rail pressure (b), NO_x emissions (c), PM emissions (d).

favors a higher EGR rate as the EGR valves stays fully open. For the static optimization of this operating point a higher weighting factor w must be applied. Table 7.6 provides an overview of the optimization results for the load drop test case. The fast injection inputs show the greatest potential to reduce the emission values during this test case. The throttle input can be used either to reduce the boost pressure or to increase the EGR rate due to the higher pressure difference between the intake and the exhaust manifolds. Nevertheless, using the throttle input in addition to the EGR valve and the VTG inputs does not show any benefit in this test case. As in the load step test case, the optimization of all actuators yields the best result.

Table 7.6: Cost reduction potential of different input combinations for the load drop test case

Optimized inputs	m_f [g]	$m_{\mathrm{NO_x}}$ [g]	m_{PM} [mg]
Reference	3.06	0.025	0.923
u_{soi}	3.08 (101%)	0.024 (94%)	0.905 (98%)
$p_{f,\mathrm{des}}$	3.06 (99%)	0.017 (67%)	1.060 (114%)
u_{soi}, $p_{f,\mathrm{des}}$	3.05 (99%)	0.019 (76%)	0.952 (103%)
u_{vtg}, u_{egr}	3.08 (101%)	0.020 (78%)	1.010 (109%)
u_{thr}	3.04 (99%)	0.021 (83%)	0.962 (104%)
u_{vtg}, u_{egr}, u_{thr}	3.08 (101%)	0.020 (78%)	1.000 (109%)
u_{soi}, u_{vtg}, u_{egr}, u_{thr}	3.11 (102%)	0.017 (66%)	1.070 (116%)

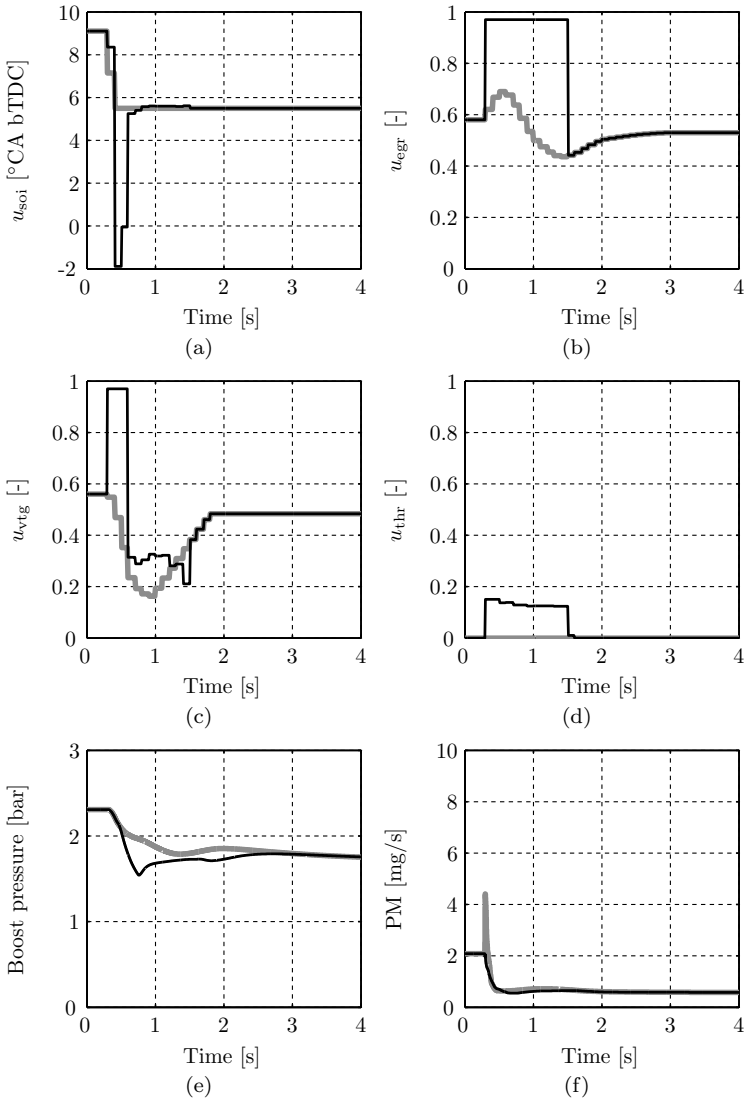

Figure 7.12: Comparison between reference (gray) and optimized (black) trajectories of the start of injection, of the EGR valve, of the VTG actuator position, and of the throttle position during a load drop at constant engine speed: start of injection (a), EGR valve position (b), VTG actuator position (c), throttle position (d), boost pressure (e), and PM emissions (f).

7.4.3 Driveability Test Case

In this subsection the results of the driveability test case are shown. The weighting factors used are $w_1 = 40$ and $w_2 = 0.9$. As in the previous test cases, various actuator combinations are tested for their potential. To avoid very high fuel rail pressures, the maximal desired fuel rail pressure is set to 1400 bar instead of 1600 bar. This measure keeps the engine noise within a reasonable range. Figure 7.13 shows the results of the driveability

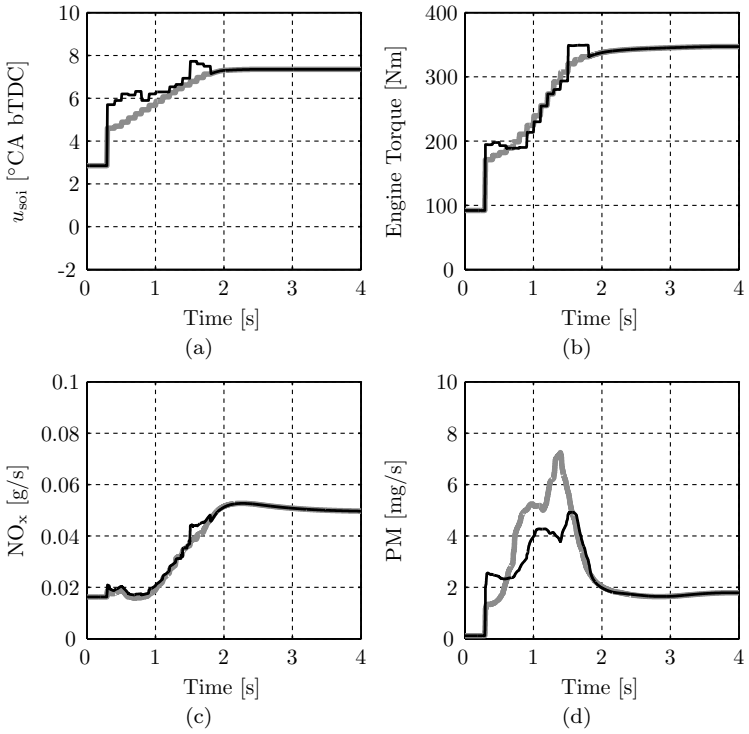

Figure 7.13: Comparison between reference (gray) and optimized (black) trajectories of the start of injection during a load step at constant engine speed: start of injection (a), engine torque (b), NO_x emissions (c), and PM emissions (d).

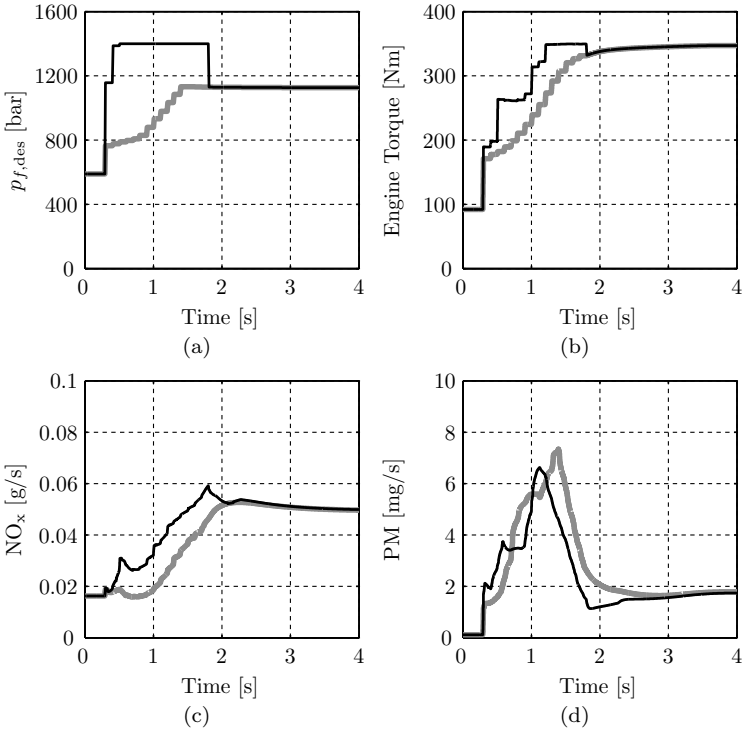

Figure 7.14: Comparison between reference (gray) and optimized (black) trajectories of the fuel rail pressure during a load step at constant engine speed: fuel rail pressure (a), engine torque (b), NO_x emissions (c), and PM emissions (d).

optimization using the start of injection input only. The benefit of using the start of injection actuator to increase the driveability is rather small with the weighting factors used. The optimized trajectory moves the start of injection to earlier injection timings. This measure allows an increase of the engine torque without generating significantly more engine-out emissions. Due to the earlier injection timings the PM emissions are slightly reduced. Figure 7.14 shows the torque trajectory using an optimized fuel

injection pressure. As in the first test case, the optimizer uses the maximal fuel injection pressure allowed (1400 bar). The generated torque is improved, while the engine-out emissions are comparable to those of the reference trajectory. The torque of the new operating point is reached approximately half a second earlier. Figure 7.15 shows the torque trajectory using an optimized fuel injection pressure and start of injection. As in the previous case, the optimizer uses the maximal fuel injection pressure allowed (1400 bar). The start of injection is set earlier during the entire load step. The generated torque is improved significantly while the engine-out emission levels stay in a reasonable range.

Figure 7.16 shows the torque trajectory using the optimized gas path actuator inputs. During the first part of the load step, the EGR valve is fully closed. Due to the optimized actuator inputs, the desired boost pressure is reached much earlier. This characteristic can be explained by the increased mass flow through the turbine, since the EGR valve is fully closed. The VTG input is set to a wider opening are, as this measure improves the turbine efficiency. Due to the higher turbine mass flow, the torque delivered to the compressor is increased. The engine torque of the new operating point is reached nearly one second earlier. However, due to the reduced EGR rate, much higher amounts of NO_x must be accepted, whereas the PM emission levels are lower.

Figure 7.17 shows the torque trajectory using the optimized gas path actuator inputs and an optimized fuel injection pressure. The additional degree of freedom is used to further increase the driveability of the engine. The gas path actuator inputs are showing trajectories comparable to those obtained in the previous case. The high number of parameters complicates

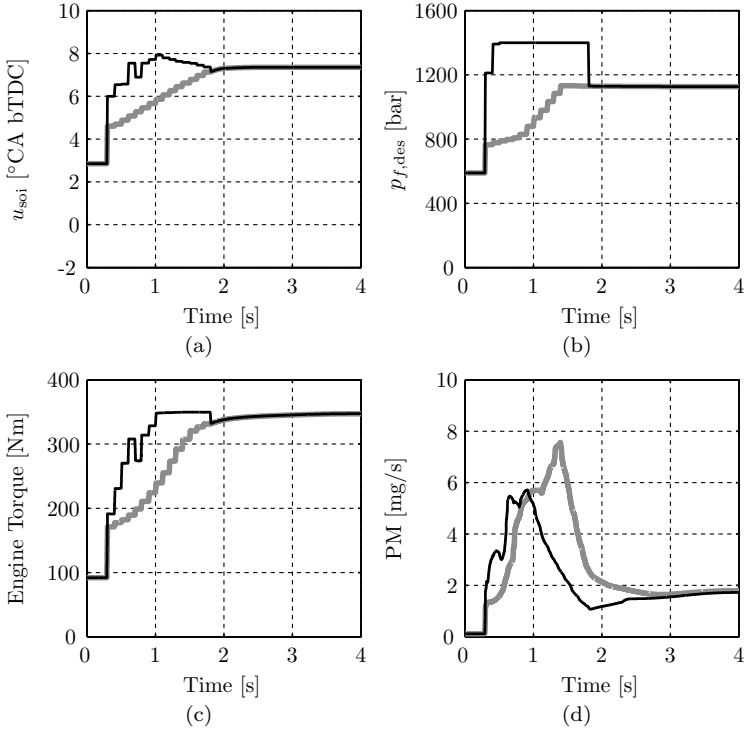

Figure 7.15: Comparison between reference (gray) and optimized (black) trajectories of the fuel rail pressure during a load step at constant engine speed: start of injection (a), fuel rail pressure (b), engine torque (c), and PM emissions (d).

the convergence of the optimization. All the trajectories oscillate increasingly. The fuel rail pressure is set to its maximal allowed value. Therefore, the PM emission levels are lower than in the previous case. A high, but narrow peak of the PM emissions occurs during the first part of the load step.

Table 7.7 summarizes the results of the driveability test case. The mechanical energy delivered to the crank shaft can be increased by ap-

proximately 30%. The amount of PM emissions decreases by between 20% and 60%. In contrast, the amount of NO_x emissions increases significantly. Again, as mentioned in the previous test cases, the NO_x emission levels are lower during a load step than in steady-state conditions.

Table 7.7: Potential of various input combinations for improving the driveability in the load drop test case

Optimized inputs	E_{mech} [kJ]	m_{NO_x} [g]	m_{PM} [mg]
Reference	87.1	0.038	6.52
u_{soi}	88.1 (101%)	0.041 (107%)	5.24 (80%)
$p_{f,\text{des}}$	104.0 (120%)	0.056 (147%)	5.65 (87%)
u_{soi}, $p_{f,\text{des}}$	111.0 (126%)	0.066 (173%)	5.12 (79%)
u_{vtg}, u_{egr}	107.0 (123%)	0.091 (241%)	3.62 (56%)
u_{soi}, u_{vtg}, u_{egr}	113.0 (130%)	0.096 (252%)	3.69 (57%)
$p_{f,\text{des}}$, u_{vtg}, u_{egr}	116.0 (133%)	0.100 (263%)	2.51 (39%)
u_{soi}, $p_{f,\text{des}}$, u_{vtg}, u_{egr}	117.0 (134%)	0.084 (222%)	2.30 (35%)

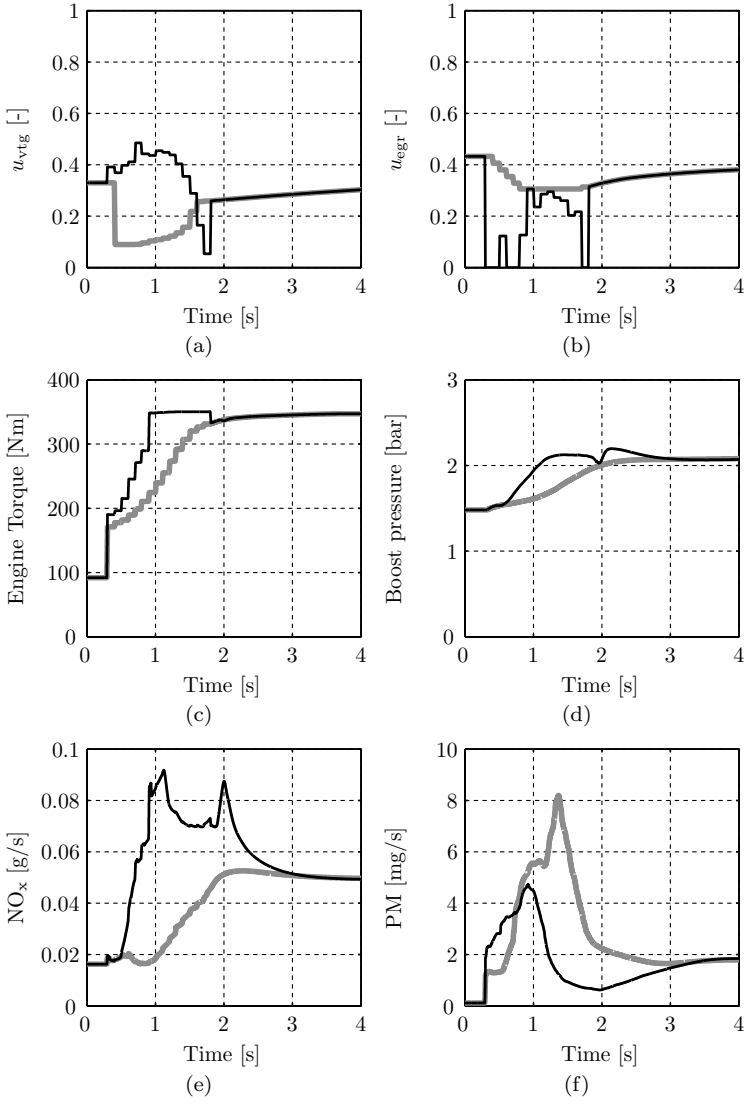

Figure 7.16: Comparison between reference (gray) and optimized (black) trajectories of the gas path actuators during a load step at constant engine speed: VTG input (a), EGR valve position (b), engine torque (c), boost pressure (d), NO_x emissions (e), and PM emissions (f).

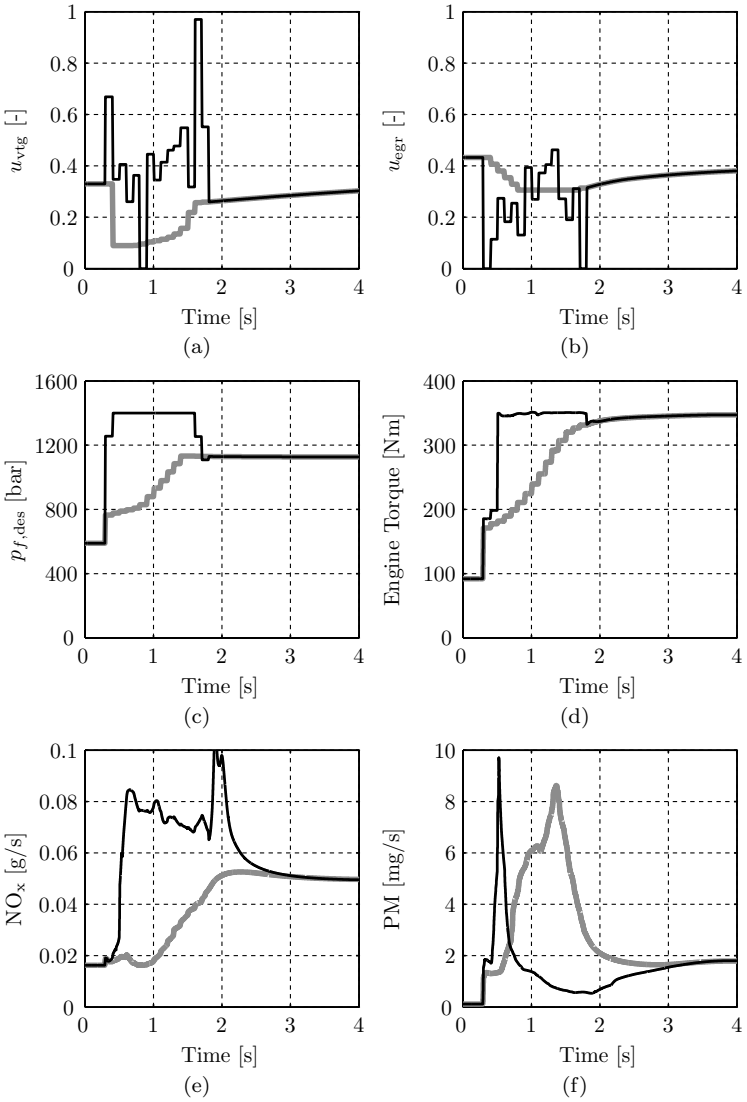

Figure 7.17: Comparison between reference (gray) and optimized (black) trajectories of the gas path actuators and the fuel rail pressure during a load step at constant engine speed: VTG input (a), EGR valve position (b), fuel rail pressure (c), engine torque (d), $\mathrm{NO_x}$ emissions (e), and PM emissions (f).

7.5 Summary and Discussion

In this chapter, a method has been presented that allows finding optimal control strategies for a diesel engine during transient operation. Together with an extended quasi-static emission model to estimate the raw emissions, a mean-value model of the engine gas path is used, .

Direct methods are the only class of optimal control solution methods found to be suitable for the given problem due to the high dimensionality and complexity of the engine model including variable time delays, nonlinear equations, and discontinuities. The optimal control problem is solved using a sequential quadratic programming algorithm.

The nonlinear, state-dependent equality constraints for engine torque and speed have been replaced by a feedforward fuel mass flow controller. This replacement considerably simplifies the optimization problem since the nonlinear path constraints are automatically fulfilled. To allow stable simulations of the engine behavior, the modeling approach is focused on the robustness of the mean-value model. All the hardware constraints are carefully implemented in the model. The combination of model and optimization algorithm is well suited to solve the problem, since physically reasonable trajectories result.

The results show a great potential in the application of optimal control methods during transient engine operation. Reductions in the order of 60% of the PM emissions are achievable during load steps. A large fraction of the emission reductions attainable can be achieved by controlling either the fuel rail pressure or the two gas path actuators. The trade-off between nitrogen oxide and particulate matter emissions is highlighted, showing

that the improvements in particulate matter emissions were obtained while just moderately increasing the nitrogen oxide emissions.

The third test case, where the requested engine torque is optimized as well, a significant increase of the driveability could be reached while the emission levels are comparable with the measured reference load step.

Chapter 8

Summary and Outlook

This chapter presents a summary of the work performed and indicates future research areas in the field of model-based engine application. Some conclusions have already been provided in the previous chapters.

8.1 Summary and Conclusion

The purpose of this analysis was to formulate a method to derive a control-oriented model of the raw emissions of a diesel engine. The mixed physics and regression approach proposed simplifies the generation of nonlinear models. In addition, the models derived are advantageous due to their increased portability to other engines. The methodology proposed is applicable to various modeling problems.

The method significantly reduces the calibration effort due to the reduced number of parameters needed to describe the transient raw emissions. The model is formulated using an extended quasi-static approach. The extension to the base map part describes the set point deviations during transient operating conditions of the engine. The deviations are predicted using correction factors. Due to the extended quasi-static ap-

proach, the raw emission model can be calibrated with static measurement data, which lowers the application costs of the model and the requirements for the test bench.

The inputs to the raw emission model are chosen by an input variable selection procedure based on a genetic programming wrapper approach.

The functional structure of the raw emission model is derived with a symbolic regression algorithm. The toolbox used is extended with a local search algorithm to calibrate the parameters of the functional relations generated. The separation of the input variable selection task from the model structure generation significantly reduces the computational effort. The methodology can be divided into four main steps:

1. Definition of the relevant process variables by expert knowledge;

2. Selection of candidate variables from a set of characteristic process variables using the IVS algorithm;

3. Determination of a lean model structure based on the symbolic regression algorithm;

4. Providing the transient inputs of the model using control-oriented modeling approaches.

The raw emission model derived is tested for two different application scenarios. First, the raw emission model is used as a virtual sensor. A cylinder mass and composition estimator and an empirical combustion model provide the transient inputs for the raw emission model. The combination of the three models allows an estimation of the raw emissions in

transient operating conditions. The extended quasi-static approach is able to predict the quantities of the raw emissions during various transients.

Second, the raw emission model is embedded in a control-oriented engine system model. The model is used to generate optimal input trajectories to reduce emission peaks during selected transients. Direct methods are the only class of optimal control solution methods found to be suitable for the given problem due to the high dimensionality and complexity of the engine model. The optimal control problem is solved using a sequential quadratic programming algorithm. The combination of model and numerical algorithm is well suited to solve the optimal control problem, since physically reasonable trajectories result.

The results show a great potential in the application of optimal control methods during transient engine operation. The trade-off between nitrogen oxide and particulate matter emissions is highlighted, showing that the reductions in particulate matter emissions were obtained while increasing only moderately the nitrogen oxide emissions. In addition, driveability improvements are achieved using optimized actuator inputs.

The reduced emission levels have several advantages:

- fuel-costly regenerations of the particulate filter can be reduced,
- higher emission standards are reachable,
- requirements for the aftertreatment system are lower,
- requirements for the engine components are lower,
- driveability can be improvemed.

8.2 Outlook

There are several areas where the research can be pursued further. The raw emission model could be improved using comprehensive data sets of even more engine types. Additionally, a different model structure can be investigated to extend the possible application areas.

The virtual sensor structure could be implemented in the ECU to improve the control of the aftertreatment system. In addition, costly hardware, such as a NO_x sensor in the engine exhaust, could be replaced by the virtual sensor. Moreover, a robust closed-loop controller should be derived.

With further knowledge of design parameters such as engine noise dictating engine operation, the cost function of the optimization strategy could be refined. In addition, the aftertreatment devices could be considered as well to further improve the interactions of the entire engine system.

Based on regulatory driving cycles more test cases could be defined. The resulting trajectories should be realized as a feedforward control law that would be implementable directly in the ECU.

Appendix A

Nomenclature

The following lists explain the equation symbols, the subscripts and superscripts, the operations, and the abbreviations and acronyms used in this text. Naming conflicts are unavoidable. However, the proper meaning of each symbol should always be unambiguously deducible from the context. Unless otherwise stated, SI units are assumed throughout the thesis. The derivative of a variable $x(t)$, with respect to its independent variable t, is denoted either by

$$\frac{d}{dt}x(t)$$

or by

$$\dot{x}(t)$$

while the notation

$$\overset{*}{x}(t)$$

indicates a flow of mass or heat.

Symbols

Symbol	Description	Unit
A	surface or area	[m^2]
E	energy, work	[J]
H	enthalpy	[J]
G	transfer function	[-]
J	cost function	[-]
$\overset{*}{Q}$	heat flow	[J/s]
R	specific ideal gas constant	[J/kgK]
S	stroke	[m]
T	torque	[Nm]
U	internal energy	[J]
V	volume	[m^3]
c_m	mean piston speed	[m/s]
c_p	specific heat capacity at constant pressure	[J/kgK]
c_v	specific heat capacity at constant volume	[J/kgK]
d	diameter	[m]
e	engine efficiency	[-]
f	factor	[-]
k	constant coefficient (parameter)	[-]
l	length	[m]
m	mass	[kg]
n	quantity	[-]
p	pressure	[Pa]

Symbol	Description	Unit
p_{m0}	mean loss pressure	[Pa]
p_{me}	mean effective pressure	[Pa]
p_{mf}	fuel mean pressure	[Pa]
r	radius, ratio	[m],[-]
u	input signal	[-]
w	weighting factor	[-]
x	mass ratio	[-]
y	output signal	[-]
Δt	time delay	[s]
Π	pressure ratio	[-]
γ	correction factor	[-]
η	efficiency	[-]
ϑ	temperature	[K]
λ	air/fuel ratio	[-]
λ_l	volumetric efficiency	[-]
μ	scaled mass	[-]
ρ	density	[kg/m^3]
σ_0	stoichiometric air/fuel ratio	[-]
τ	time constant	[s]
φ	crank angle	[° CA]
ω	rotational speed	[rad/s]

Indices

Symbol	Description
0	reference, base map
1	before compressor
2	intake manifold
3	exhaust manifold
4	after turbine
a	ambient
b	braking
c	compressor
d	displaced, driving
e	engine
f	fuel
g	gas exchange
l	liquid, load
p	pipe
r	receiver
t	turbine
w	wall
B01	1% of fuel mass burnt
B05	5% of fuel mass burnt
B10	10% of fuel mass burnt
B50	50% of fuel mass burnt
B90	90% of fuel mass burnt

Symbol	Description
act	actual
air	air
bg	burnt gas
co	combustion
cr	critical
cyl	cylinder
dcv	delivery control valve
des	desired
ds	downstream
eff	effective
eg	exhaust gas
egr	exhaust gas recirculation
ex	exhaust stroke
fp	fuel pressure
fr	friction
he	heat exchanger
hfm	air flow sensor
hpp	high pressure common-rail pump
ia	intake air
ic	intercooler
ifr	incompressible flow restriction
in	flow-in, intake
inj	injection

Symbol	Description
lb	lower bound
lo	lift-off
max	maximal
opt	optimal
out	flow-out
pcv	common-rail pressure control valve
pos	position
rail	fuel rail
ref	reference
req	requested
res	rescaled
rg	residual gas
sel	selected
soi	start of injection
tc	turbocharger
thr	throttle
tot	total
tr	threshold
ub	upper bound
us	upstream

Acronyms and Abbreviations

Symbol	Description
ANN	artificial neural network
aTDC	after top dead center
BMEP	brake mean effective pressure
bTDC	before top dead center
CA	crank angle
CAN	controller area network
CFD	computational fluid dynamics
CI	compression ignited
CO	carbon monoxide
CO_2	carbon dioxide
CR	common-rail
DI	direct injected
DoE	design of experiments
DPF	diesel particulate filter
ECU	electronic control unit
EGR	exhaust gas recirculation
ETC	European Transient Cycle
ETH	Swiss Federal Institute of Technology
FSN	filter smoke number
HD	heavy-duty
HFM	hot-film mass flow sensor
GA	genetic algorithm

Symbol	Description
IC	internal combustion
ID	ignition delay
INJ	injection
IVS	input variable selection
LD	light-duty
MI	mutual information
MVEM	mean-value engine model
NLP	nonlinear programming
NO	nitric oxide
NO_x	nitrogen oxides
O_2	oxygen
ODE	ordinary differential equation
PCA	principle component analysis
PM	particulate matter
QSS	quasi-static simulation
REM	raw emission model
SCR	selective catalytic reduction
SOC	start of combustion
SOI	start of injection
SQP	sequential quadratic programming
SR	symbolic regression
TC	turbocharger
TDC	top dead center

Symbol	Description
THC	total hydrocarbons
VTG	variable turbine geometry
WG	waste gate

Appendix B

Mean-Value Engine Model

The following modeling approaches are mostly in accordance with [35].

B.1 Incompressible Flow Restriction

The incompressible flow restriction model [35] is used when moderate flow velocities (i.e., $u < 0.3$ Ma) occur.

The transformation of Bernoulli's equation for incompressible flows yields the following equations for the mass flow

$$\overset{*}{m}_{\mathrm{ifr}} = \sqrt{\frac{p_{\mathrm{us}}}{k_{\mathrm{ifr},1} \cdot \vartheta_{\mathrm{us}}}} \cdot \sqrt{p_{\mathrm{us}} - p_{\mathrm{ds}}}. \tag{B.1}$$

To avoid problems with the ODE solver in the case of small pressure differences, the second root in (B.1) is replaced by a linear component if the pressure difference is below a certain limit $k_{\mathrm{ifr},2}$.

$$\overset{*}{m}_{\mathrm{ifr}} = \sqrt{\frac{p_{\mathrm{us}}}{k_{\mathrm{ifr},1} \cdot \vartheta_{\mathrm{us}}}} \cdot \frac{p_{\mathrm{us}} - p_{\mathrm{ds}}}{\sqrt{k_{\mathrm{ifr},2}}} \text{ if } p_{\mathrm{us}} - p_{\mathrm{ds}} < k_{\mathrm{ifr},2} \tag{B.2}$$

In the case of negative pressure drops the mass flow is zero.

Since the restriction is assumed to be isothermal, the temperature downstream is equal to the temperature upstream:

$$\vartheta_{\mathrm{ds}} = \vartheta_{\mathrm{us}}. \tag{B.3}$$

Table B.1: Incompressible flow restriction: description

Inputs	p_{us}	[Pa]	pressure upstream
	p_{ds}	[Pa]	pressure downstream
	ϑ_{us}	[K]	temperature upstream
Outputs	$\overset{*}{m}_{\mathrm{ifr}}$	[kg/s]	mass flow through restriction
	ϑ_{ds}	[K]	temperature downstream
Parameters	$k_{\mathrm{ifr},1}$	[-]	flow resistance coefficient
	$k_{\mathrm{ifr},2}$	[Pa]	linearization limit

B.2 Compressible Flow Restriction

The compressible flow restriction model [35] is used when high flow velocities (i.e., $u > 0.3$ Ma) occur. As the flow through a compressible flow restriction might reach sonic speeds, the model distinguishes between choked and unchoked flows. The compressible flow restriction is modeled as an isenthalpic process. The throttling process is assumed to be isothermal. As in the incompressible flow restriction, for pressure ratios larger than 1, the mass flow is set to zero. The effective opening area A_{eff} is a function of the particular actuator input

$$A_{\mathrm{eff}} = f(u). \tag{B.4}$$

Using the relationship for an isentropic expansion, the following equation is obtained:

$$\overset{*}{m}_{\mathrm{cfr}} = A_{\mathrm{eff}} \cdot \frac{p_{\mathrm{us}}}{\sqrt{R \cdot \vartheta_{\mathrm{us}}}} \cdot \Psi(\Pi), \tag{B.5}$$

where Π is the pressure ratio defined as

$$\Pi = \frac{p_{\mathrm{ds}}}{p_{\mathrm{us}}}. \tag{B.6}$$

The function Ψ must distinguish between different cases. The usual case is the unchoked flow, which occurs when the pressure ratio Π is above the critical pressure ratio Π_{cr}. To avoid an infinite gradient of Ψ at $\Pi = 1$, an additional case is introduced for pressure ratios above some threshold pressure ratio Π_{tr}. The third case occurs when the pressure ratio is below the critical pressure ratio Π_{cr}. In this case the flow is choked:

$$\Psi = \begin{cases} 0 & \Pi \geq 1 \\ a \cdot (\Pi - 1)^3 + b \cdot (\Pi - 1) & 1 > \Pi \geq \Pi_{\mathrm{tr}} \\ \Pi^{1/\kappa} \cdot \sqrt{\frac{2\kappa}{\kappa - 1} \cdot \left(1 - \Pi^{\frac{\kappa-1}{\kappa}}\right)} & \Pi_{\mathrm{tr}} > \Pi \geq \Pi_{\mathrm{cr}} \\ \sqrt{\kappa \cdot \left(\frac{2}{\kappa+1}\right)^{\frac{\kappa+1}{\kappa-1}}} & \Pi < \Pi_{\mathrm{cr}} \end{cases} \tag{B.7}$$

where a and b are defined as

$$a = \frac{\Psi'_{\mathrm{tr}} \cdot (\Pi_{\mathrm{tr}} - 1) - \Psi_{\mathrm{tr}}}{2\,(\Pi_{\mathrm{tr}} - 1)^3} \tag{B.8}$$

$$b = \Psi'_{\mathrm{tr}} - 3a \cdot (\Pi_{\mathrm{tr}} - 1)^2. \tag{B.9}$$

The variables Ψ_{tr} and Ψ'_{tr} in (B.8) and (B.9) are the values of Ψ and the derivative of Ψ at the threshold pressure ratio Π_{tr}, respectively.

The critical pressure ratio is defined as

$$\Pi_{\mathrm{cr}} = \left(\frac{2}{\kappa+1}\right)^{\frac{\kappa}{\kappa-1}}. \tag{B.10}$$

Because of the assumption of no losses in the restriction, the downstream temperature is equal to the upstream temperature

$$\vartheta_{\mathrm{us}} = \vartheta_{\mathrm{ds}}. \tag{B.11}$$

Table B.2: Compressible flow restriction: description

Inputs	A_{eff}	[m^2]	effective area
	p_{us}	[Pa]	pressure upstream
	p_{ds}	[Pa]	pressure downstream
	ϑ_{us}	[K]	temperature upstream
Outputs	$\overset{*}{m}_{\mathrm{cfr}}$	[kg/s]	mass flow through restriction
	ϑ_{ds}	[K]	temperature downstream
Parameters	κ	[-]	specific heat capacity ratio
	R	[J/kgK]	specific ideal gas constant
	Π_{tr}	[-]	threshold pressure ratio

B.3 Heat Exchanger

Heat exchanging elements are used to cool down the gas after the compressor or the EGR mass flow, respectively. The downstream temperature

is estimated with the following equation

$$\vartheta_{ds} = (\vartheta_{us} - \vartheta_w) \cdot e^{k_{\mathrm{he},1} \cdot \overset{*}{m}_{\mathrm{he}}^{\,k_{\mathrm{he},2}}} + \vartheta_w. \tag{B.12}$$

The wall temperature of the heat exchanger is assumed to be constant.

Table B.3: Cooling element: description

Inputs	$\overset{*}{m}_{\mathrm{he}}$	[kg/s]	mass flow through the cooler element
	ϑ_{us}	[K]	upstream temperature
Outputs	ϑ_{ds}	[K]	downstream temperature
Parameters	$k_{\mathrm{he},1}$	[s/kg]	parameter one
	$k_{\mathrm{he},2}$	[-]	parameter two
	ϑ_w	[K]	wall temperature of the intercooler

B.4 Compressor

The compressor is modeled according to [38]. The model estimates the compressor torque, the downstream temperature and the compressor mass flow for a given pressure ratio, speed and upstream temperature. The model takes into account special cases such as choked flow, surge, and a low-speed regime to provide physically meaningful results over a wide range of input configurations. The measured compressor maps obtained on a special turbocharger test bench are correct for a given inlet temperature and pressure (e.g., 25 °C and 1013 hPa). Therefore the compressor speed is corrected with respect to the reference values as

$$\tilde{\omega}_{\mathrm{tc}} = \sqrt{\frac{\vartheta_{\mathrm{ref}}}{\vartheta_{\mathrm{us}}}} \cdot \omega_{\mathrm{tc}} \tag{B.13}$$

Table B.4: Compressor: description

Inputs	ω_{tc}	[rad/s]	turbocharger speed
	p_{us}	[Pa]	upstream pressure
	p_{ds}	[Pa]	downstream pressure
	ϑ_{us}	[K]	upstream temperature
Outputs	T_c	[Nm]	compressor torque
	ϑ_{ds}	[K]	downstream temperature
	$\overset{*}{m}_c$	[kg/s]	compressor mass flow
Parameters	κ	[-]	ratio of specific heats
	R	[J/kgK]	specific ideal gas constant
	p_{ref}	[Pa]	reference upstream pressure
	ϑ_{ref}	[K]	reference upstream temperature
	r_c	[m]	compressor wheel radius
	$k_{\mathrm{c,i}}$	[-]	fitting parameters for the mass flow
	$\overset{*}{\mu}_{c,\mathrm{opt}}$	[kg/s]	mass flow at $\eta_{c,\mathrm{opt}}$
	$\Pi_{c,\mathrm{opt}}$	[-]	pressure ratio at $\eta_{c,\mathrm{opt}}$
	$\eta_{c,\mathrm{opt}}$	[-]	optimal efficiency
	$\overset{*}{\mu}_{c,\mathrm{max}}$	[kg/s]	choked mass flow for reference properties
	$\omega_{\mathrm{tc,min}}$	[rad/s]	minimum speed for compressor characteristics
	$\omega_{\mathrm{tc,tol}}$	[rad/s]	tolerance band around $\omega_{\mathrm{tc,min}}$
	$k_{\eta,i}$	[-]	efficiency fitting parameters
	$k_{\sigma,i}$	[-]	surge line fitting parameters $i = 1, ..., 4$
	$\frac{d}{dt}\overset{*}{m}_{c,max}$	[kg/s^2]	maximum mass flow variation

and the mass flow through the compressor is corrected as

$$\overset{*}{\mu}_c = \sqrt{\frac{\vartheta_{\mathrm{us}}}{\vartheta_{\mathrm{ref}}}} \cdot \frac{p_{\mathrm{ref}}}{p_{\mathrm{us}}} \cdot \overset{*}{m}_c \, . \tag{B.14}$$

The pressure ratio over the compressor is defined as:

$$\Pi_c \;=\; \frac{p_{\mathrm{ds}}}{p_{\mathrm{us}}}. \tag{B.15}$$

The behavior of the compressor is given in graphs representing the normalized mass flow $\overset{*}{\mu}_c$ over the normalized pressure ratio Π_c. To model

the compressor characteristics, the head parameter Ψ_c and the normalized compressor flow rate Φ_c are introduced

$$\Psi_c = \frac{c_p \cdot \vartheta_{\text{ref}} \cdot \left[\left(\frac{p_2}{p_1} \right)^{\frac{\kappa-1}{\kappa}} - 1 \right]}{\frac{1}{2}(\tilde{\omega}_{\text{tc}} \cdot r_c)^2} \tag{B.16}$$

$$\Phi_c = \frac{\overset{*}{\mu}_c}{\rho_{\text{ref}} \cdot \pi \cdot r_c^3 \cdot \tilde{\omega}_{\text{tc}}} \tag{B.17}$$

where r_c is the compressor wheel radius and $\tilde{\omega}_{\text{tc}}$ the corrected shaft speed. The head parameter Ψ_c can be approximated as

$$\Psi_c = \frac{k_{c,1} + k_{c,2} \cdot \Phi_c}{k_{c,3} - \Phi_c}, \tag{B.18}$$

where the parameters $k_{c,1}$-$k_{c,3}$ are linear functions of the Mach number

$$\text{Ma} = \frac{r_c \cdot \tilde{\omega}_{\text{tc}}}{\sqrt{\kappa \cdot R \cdot \vartheta_{\text{ref}}}}. \tag{B.19}$$

By inversion of (B.18) and substitution into (B.17) the mass flow $\overset{*}{\mu}_c$ is obtained as

$$\overset{*}{\mu}_c = \frac{k_{c,3} \cdot \Psi_c - k_{c,1}}{k_{c,2} + \Psi_c} \cdot \rho_{\text{ref}} \cdot \pi \cdot r_c^3 \cdot \tilde{\omega}_{\text{tc}}. \tag{B.20}$$

Although (B.20) is defined for all real values except $\Psi_c = -k_{c,2}$, physically meaningful results are only obtained in the interval

$$\Psi_c \in \left[0, \frac{k_{c,1}}{k_{c,3}}\right] \tag{B.21}$$

since $\overset{*}{\mu}_c$ is negative for $\Psi_c > k_1/k_3$. In this operating range the compressor is in the so-called surge condition. When this condition occurs, the

mass flow through the compressor model is set to zero and the derivative of the mass flow is limited in order to adequately represent the surge condition. The actual surge line for reference conditions is approximated by a polynomial of third order as a function of the shaft speed.

The compressor must be carefully parametrized. The following condition must be fulfilled for the relevant turbocharger speed range

$$k_{c,1} + k_{c,2} \cdot k_{c,3} < 0 \tag{B.22}$$

in order to prevent wrong compressor mass flows in the high-speed regime. This behavior occurs due to a changed characteristic of the fitting curves, as expressed by Eq. (B.18). When the flow reaches sonic conditions in the narrowest section of the compressor, the mass flow cannot increase further. This characteristic is represented by an upper boundary for the mass flow $\overset{*}{\mu}_{c,\max}$. In its low-speed regime ($\omega_{\mathrm{tc}} \leq \omega_{\mathrm{tc,min}}$), the compressor is modeled as a fixed orifice. In this case, a mass flow only occurs when the pressure ratio Π_c is smaller than 1. The area of the orifice is calculated, such that it reaches choked conditions at reference temperature and pressure.

A smooth change over the two regimes is implemented to avoid oscillations between the two regimes. The fraction f_{ls} of low-speed operation is calculated as

$$f_{\mathrm{ls}} = \frac{\omega_{\mathrm{tc}} - (\omega_{\mathrm{tc,min}} - \omega_{\mathrm{tc,tol}})}{2 \cdot \omega_{\mathrm{tc,tol}}}. \tag{B.23}$$

The mass flow becomes the weighted average of low-speed mass flow $\overset{*}{\mu}_{c,\mathrm{ls}}$ and the normal speed mass flow $\overset{*}{\mu}_c$ can be calculated as follows:

$$\overset{*}{\mu}_c = f_{\mathrm{ls}} \cdot \overset{*}{\mu}_c + (1 - f_{\mathrm{ls}}) \overset{*}{\mu}_{c,\mathrm{ls}} \, . \tag{B.24}$$

The compressor torque is obtained as follows:

$$T_c = \overset{*}{m}_c \cdot c_p \cdot \vartheta_{\mathrm{us}} \cdot \left(\Pi_c^{\frac{\kappa-1}{\kappa}} - 1 \right) \cdot \frac{1}{\eta_c} \cdot \frac{1}{\omega_{\mathrm{tc}}}. \tag{B.25}$$

The temperature downstream of the compressor is defined by the compression ratio and the isentropic efficiency

$$\vartheta_{\mathrm{ds}} = \vartheta_{\mathrm{us}} + \left(\Pi_c^{\frac{\kappa-1}{\kappa}} - 1 \right) \cdot \frac{1}{\eta_c}. \tag{B.26}$$

The compressor isentropic isoefficiency lines are approximated by ellipsoids as follows:

$$\eta_c(\Pi_c, \overset{*}{\mu}_c) = \eta_{c,\mathrm{opt}} - \chi^T \cdot \begin{bmatrix} k_{\eta,1} & k_{\eta,2} \\ k_{\eta,3} & k_{\eta,4} \end{bmatrix} \cdot \chi \tag{B.27}$$

with

$$\chi^T(\Pi_c, \dot{\mu}_c) \;=\; \left[\overset{*}{\mu}_c - \overset{*}{\mu}_{c,\mathrm{opt}},\; \Pi_{c,\mathrm{res}} - \Pi_{c,\mathrm{opt}} \right] \tag{B.28}$$

using the rescaled pressure ratio $\Pi_{c,\mathrm{res}}$

$$\Pi_{c,\mathrm{res}} \;=\; 1 + \sqrt{\Pi_c - 1}. \tag{B.29}$$

B.5 Turbine (VTG)

For given values of pressure ratio, speed, and upstream temperature, the turbine model yields the torque provided by the turbine, the downstream temperature, and the mass flow.

The mass flow characteristic of the turbine is modeled as a fixed orifice. The pressure ratio over the turbine is defined as follows:

Table B.5: Turbine: description

Inputs	ω_{tc}	[rad/s]	turbocharger speed
	p_{us}	[Pa]	upstream pressure
	p_{ds}	[Pa]	downstream pressure
	ϑ_{us}	[K]	upstream temperature
Outputs	T_t	[Nm]	turbine torque
	ϑ_{ds}	[K]	downstream temperature
	$\overset{*}{m}_t$	[kg/s]	turbine mass flow
Parameters	κ	[-]	ratio of specific heats
	c_p	[J/kgK]	specific heat capacity at constant pressure
	r_t	[m]	turbine wheel radius
	$\tilde{c}_{\mathrm{us,opt}}$	[-]	turbine blade speed ratio at maximum efficiency
	$\eta_{t,\max}$	[-]	maximum turbine efficiency
	c_t	$[\frac{\mathrm{kg}\sqrt{\mathrm{K}}}{\mathrm{sPa}}]$	fitting parameter for turbine mass flow
	k_Π	[-]	fitting parameter for turbine mass flow

$$\Pi_t \;=\; \frac{p_{\mathrm{us}}}{p_{\mathrm{ds}}} \;\geq\; 1. \tag{B.30}$$

The mass flow model of the turbine follows the model of a normalized orifice. The parameters c_t and k_t need to be identified as follows:

$$\overset{*}{m}_t = \frac{p_{\mathrm{us}}}{\sqrt{\vartheta_{\mathrm{us}}}} \cdot c_t \cdot \sqrt{1 - \Pi_t^{k_t}}. \tag{B.31}$$

The downstream temperature and the torque provided by the turbine are calculated with the isentropic efficiency of the turbine

$$\vartheta_{\mathrm{ds}} = \vartheta_{\mathrm{us}} \cdot \left(1 - \left(1 - \Pi_t^{\frac{1-\kappa}{\kappa}}\right) \cdot \eta_t\right), \tag{B.32}$$

$$T_t \;=\; \frac{P_t}{\omega_{\mathrm{tc}}} = \overset{*}{m}_t \cdot c_p \cdot . \vartheta_{\mathrm{us}} \cdot \left(1 - \Pi_t^{\frac{1-\kappa}{\kappa}}\right) \cdot \eta_t. \tag{B.33}$$

The efficiency of the turbine is approximated using a quadratic approach, depending on the pressure ratio and the turbine-blade-speed ratio $\tilde{c}_{\mathrm{us}}$

$$\eta_t(\tilde{c}_{\mathrm{us}}) = \eta_{t,\max} \cdot \left(\frac{2\tilde{c}_{\mathrm{us}}}{\tilde{c}_{\mathrm{us,opt}}} - \left(\frac{\tilde{c}_{\mathrm{us}}}{\tilde{c}_{\mathrm{us,opt}}} \right)^2 \right). \tag{B.34}$$

The turbine-blade-speed ratio $\tilde{c}_{\mathrm{us}}$ is the ratio between the blade tip speed and the speed resulting from an isentropic expansion of the fluid

$$\tilde{c}_{\mathrm{us}} = \frac{r_t \cdot \omega_{\mathrm{tc}}}{\sqrt{2 \cdot c_p \cdot \vartheta_{\mathrm{us}} \cdot \left(1 - \Pi_t^{\frac{1-\kappa}{\kappa}}\right)}}. \tag{B.35}$$

VTG turbines have a variable impeller position which affects the inlet area. The fitting parameters c_t and k_t and the maximal efficiency thus are a function of the control signal u_{vtg}

$$c_t = f(u_{\mathrm{vtg}}), \tag{B.36}$$

$$k_t = f(u_{\mathrm{vtg}}), \tag{B.37}$$

$$\eta_{t,\max} = f(u_{\mathrm{vtg}}). \tag{B.38}$$

B.6 Heat Exchange and Wall Temperature

The internal energy level variable of the wall, its temperature, is approximated as being uniform over the wall section. The convective heat flow between the receiver wall and the gas in the receiver is estimated as follows:

$$\overset{*}{Q}_w = \alpha_w \cdot A_w \cdot (\vartheta_w - \vartheta_r), \tag{B.39}$$

where ϑ_w is the wall temperature and α_i the heat transfer coefficient. Radiation is neglected. The differential equation governing the temperature of the receiver wall is calculated as follows:

$$\frac{d}{dt}\vartheta_w = -\frac{\overset{*}{Q}_w + \overset{*}{Q}_a}{m_w \cdot c_w}, \tag{B.40}$$

where $\overset{*}{Q}_a$ is the heat flow from the wall to the ambient of the receiver element. According to (B.39), $\overset{*}{Q}_a$ is obtained as follows:

$$\overset{*}{Q}_a = \alpha_a \cdot A_w \cdot (\vartheta_w - \vartheta_a)\,. \tag{B.41}$$

Table B.6: Heat exchange and wall temperature: description

Inputs	ϑ_r	[K]	temperature in the receiver
Outputs	$\overset{*}{Q}_w$	[J/s]	heat flow from the receiver gas to the wall
	ϑ_w	[K]	wall temperature
Parameters	A_w	[m^2]	wall surface of the storage device
	m_w	[kg]	mass of the storage device (wall)
	ϑ_a	[K]	ambient temperature
	α_w	[W/m^{2}K]	inner heat transfer coefficient
	α_a	[W/m^{2}K]	outer heat transfer coefficient
	c_w	[J/kgK]	specific heat capacity of the wall material

B.7 Inertia

The rotational speed of the turbocharger and the crankshaft is calculated as

$$\Theta \cdot \frac{d}{dt}\omega = T_d - k_\Theta \cdot \omega - T_b, \tag{B.42}$$

where an additional damping coefficient d_ω is used.

Table B.7: Inertia: description

Inputs	T_d	[Nm]	driving torque
	T_b	[Nm]	braking torque
Outputs	ω	[rad/s]	rotational speed
Parameters	Θ	[m^{2}kg]	inertia
	k_Θ	[Nm s/rad]	damping coefficient
States	ω	[rad/s]	rotational speed

B.8 Receiver

The receiver model is used to approximate the storage capacities (mass and internal energy) in cavities such as the intake manifold, for instance [35]. It is modeled with a lumped parameter approach (i.e., no spatial variation of the states in the fluid). Additionally, the receiver takes into account the burnt gas fraction of the fluid. If the heat exchange of the receiver with its surroundings cannot be neglected, the model has an additional input for the heat flow into the system $\overset{*}{Q}_{\text{in}}$ or for negative values out of the receiver, respectively. The following differential equation describes the

mass balance of fresh air in the receiver

$$\frac{d}{dt}m_{\mathrm{air,r}} = \sum_i (1 - x_{\mathrm{bg,in,i}}) \cdot \overset{*}{m}_{\mathrm{in,i}} - \sum_j (1 - x_{\mathrm{bg,r}}) \cdot \overset{*}{m}_{\mathrm{out,j}} \ . \tag{B.43}$$

Analogously, the differential equation describing the mass balance of burnt gas in the receiver is defined as

$$\frac{d}{dt}m_{\mathrm{bg,r}} = \sum_i x_{\mathrm{bg,in,i}} \cdot \overset{*}{m}_{\mathrm{in,i}} - \sum_j x_{\mathrm{bg,r}} \cdot \overset{*}{m}_{\mathrm{out,j}} \ . \tag{B.44}$$

The burnt gas ratio in the receiver is defined as follows:

$$x_{\mathrm{bg,r}} = \frac{m_{\mathrm{bg,r}}}{m_r}. \tag{B.45}$$

Table B.8: Receiver: description

Inputs	$\overset{*}{m}_{\mathrm{in,i}}$	[kg/s]	input flow i
	$x_{\mathrm{bg,in,i}}$	[-]	burnt gas ratio of the input flow i
	$\vartheta_{\mathrm{in,i}}$	[K]	temperature of the input flow i
	$\overset{*}{m}_{\mathrm{out,j}}$	[kg/s]	output mass flow j
	$\overset{*}{Q}_{\mathrm{in}}$	[J/s]	heat flow into the system
Outputs	p_r	[Pa]	pressure in the receiver
	$x_{\mathrm{bg,r}}$	[-]	burnt gas ratio in the receiver
	ϑ_r	[K]	temperature in the receiver
Parameters	V_r	[m^3]	volume of the receiver
	κ	[-]	ratio of specific heats
	R	[J/kgK]	specific ideal gas constant
States	$m_{\mathrm{air,r}}$	[kg]	air mass in the receiver
	$m_{\mathrm{bg,r}}$	[kg]	burnt gas mass in the receiver
	ϑ_r	[K]	temperature in the receiver

where m_r is the total mass in the receiver given by

$$m_r = m_{\mathrm{bg,r}} + m_{\mathrm{air,r}}. \tag{B.46}$$

Under the assumption of negligible changes in potential and kinetic energy of the fluid, the differential equation describing the balance for the internal energy is obtained as follows:

$$\frac{d}{dt}U = \overset{*}{H}_{\mathrm{in}} - \overset{*}{H}_{\mathrm{out}} + \overset{*}{Q}_{\mathrm{in}} \,. \tag{B.47}$$

The coupling between these three equations is given by the ideal gas law and the following caloric equations:

$$U = m_r \cdot c_v \cdot \vartheta_r, \tag{B.48}$$

$$\overset{*}{H}_{\mathrm{in}} = \sum_i \overset{*}{m}_{\mathrm{in,i}} \cdot c_p \cdot \vartheta_{\mathrm{in}}, \tag{B.49}$$

$$\overset{*}{H}_{\mathrm{out}} = \sum_j \overset{*}{m}_{\mathrm{out,j}} \cdot c_p \cdot \vartheta_{\mathrm{r}}. \tag{B.50}$$

The differentiation of the internal energy with respect to t leads to

$$\frac{d}{dt}U = \frac{d}{dt}m_r \cdot c_v \cdot \vartheta_r + \frac{d}{dt}\vartheta_r \cdot c_v \cdot m_r. \tag{B.51}$$

After some algebraic manipulations, the substitution of (B.51) in (B.47) leads to the following differential equation for the receiver temperature:

$$\frac{d}{dt}\vartheta_r = \frac{1}{m_r \cdot c_v} \cdot \left(\overset{*}{H}_{\mathrm{in}} - \overset{*}{H}_{\mathrm{out}} + \overset{*}{Q}_{\mathrm{in}} - \frac{d}{dt}m_r \cdot c_v \cdot \vartheta_r \right). \tag{B.52}$$

The pressure in the receiver is given by the ideal gas law

$$p_r = \frac{m_r \cdot R \cdot \vartheta_r}{V_r}. \tag{B.53}$$

If high temperature changes occur in the receiver system, the specific heat capacity must be modeled as being quasi-constant. Since the specific heat capacity c_p of air and burnt gases (air/fuel ratio equal to one) varies significantly with temperature, the specific heat capacity is approximated as a linear function of the gas temperature. The specific heat capacity of the mixed gas is calculated by weighting the two values according to the exhaust gas mass ratio

$$\begin{aligned} c_p = & x_{\mathrm{bg}} \cdot (999.2 \tfrac{\mathrm{J}}{\mathrm{kg \cdot K}} + 0.240 \tfrac{\mathrm{J}}{\mathrm{kg}} \cdot \vartheta) \\ & + (1 - x_{\mathrm{bg}}) \cdot (965.5 \tfrac{\mathrm{J}}{\mathrm{kg \cdot K}} + 0.152 \tfrac{\mathrm{J}}{\mathrm{kg}} \cdot \vartheta) \end{aligned} \tag{B.54}$$

where ϑ is the gas temperature and x_{bg} the burnt gas fraction. The specific heat capacity c_v is then calculated as

$$c_v = \frac{c_p}{\kappa}. \tag{B.55}$$

Bibliography

[1] Robert Bosch GmbH, *Electronic Diesel Control EDC: Bosch Technical Instruction*. Bentley Publishers, 2003.

[2] L. Guzzella and A. Amstutz, "Control of diesel engines," *IEEE Control Systems Magazine*, vol. 18, no. 5, pp. 53–71, 1998.

[3] M. Ammann, N. Fekete, A. Amstutz, and L. Guzzella, "Control-oriented modeling of a turbo-charged common-rail diesel engine," in *Conference on Control and Diagnostics on Automotive Applications*, Sestri Levante, Italy, 2001.

[4] U. Christen and K. Vantine, "Event-based mean-value modeling of DI diesel engines for controller design," *SAE Technical Paper, no. 2001-01-1242*, 2001.

[5] I. Arsie, C. Pianese, and G. Rizzo, "Enhancement of control oriented engine models using neural network," in *Proc. of the 6th IEEE Mediterranean Conference on Control Systems*, Alghero, Italy, 1998.

[6] H. Hiroyasu, "Diesel engine combustion and its modeling," in *Proc. of COMODIA Symposium*, vol. Diagnostics and Modeling of Combustion in Reciprocating Engines, Tokyo, Japan, 1985, pp. 53–75.

[7] A. Amsden, J. Ramshaw, P. O'Rourke, and J. Dukowicz, "Kiva: A computer program for two- and three-dimensional fluid flows with chemical reactions and fuel sprays," Los Alamos National Laboratory, LA-10245-MS, Tech. Report, 1985.

[8] U. Gärtner, "Die Simulation der Stickoxid-Bildung in Nutzfahrzeug-Dieselmotoren," Ph.D. dissertation, University of Darmstadt, 2001.

[9] C. Ericson and B. Westerberg, "Transient emission prediction with quasi stationary models," *SAE Technical Paper, no. 2005-01-3852*, 2005.

[10] M. Traver and R. Atkinson, "Neural network-based diesel engine emissions prediction using in-cylinder combustion pressure," *SAE Technical Paper, no. 1999-01-1532*, 1999.

[11] L. del Re and P. Langthaler, "NO_x virtual sensor based on structure identification and global optimization," *SAE Technical Paper, no. 2005-01-0050*, 2005.

[12] J. Koza, *Genetic programming: On the programming of computers by means of natural selection.* MIT Press, 1992.

[13] M. Castagn, Y. Bentolila, F. Chaudoye, A. Hall, F. Nicolas, and D. Sinoquet, "Comparison of engine calibration methods based on design of experiments (DoE)," *Oil & Gas Science and Technology*, vol. 64 (4), pp. 563–582, 2008.

[14] M. Hafner and R. Isermann, "Multiobjective optimization of feedforward control maps in engine management systems towards low con-

sumption and low emissions," *Transactions of the Institute of Measurement and Control*, vol. 25, no. 1, pp. 57–74, 2003.

[15] A. Stefanopoulou, I. Kolmanovsky, and J. Freudenberg, "Control of variable geometry turbocharged diesel engines for reduced emissions," *IEEE Transactions on Control Systems Technology*, vol. 8, no. 4, pp. 733–745, July 2000.

[16] E. Alfieri, A. Amstutz, and L. Guzzella, "Gain-scheduled model-based feedback control of the air/fuel ratio in diesel engines," *Control Engineering Practice*, vol. 17, no. 12, pp. 1417–1425, December 2009.

[17] M. Hafner, M. Schuler, O. Nelles, and R. Isermann, "Fast neural networks for diesel engine control design," *Control Engineering Practice*, vol. 8, pp. 1211–1221, 2000.

[18] R. Omran, R. Younes, and J.-C. Champoussin, "Optimal control of a variable geometry turbocharged diesel engine using neural networks: Applications on the ETC test cycle," *IEEE Transactions on Control Systems Technology*, vol. 17, no. 2, pp. 380–393, March 2009.

[19] R. J. May, H. R. Maier, G. C. Dandy, and T. G. Fernando, "Non-linear variable selection for artificial neural networks using partial mutual information," *Environmental Modelling & Software*, vol. 23, no. 10-11, pp. 1312–1326, 2008.

[20] R. Kohavi and G. H. John, "Wrappers for feature subset selection," *Artif. Intell.*, vol. 97, no. 1-2, pp. 273–324, 1997.

[21] I. T. Joliffe, *Principal Component Analysis*. Springer-Verlag, 1986.

[22] A. Sharma, "Seasonal to interannual rainfall probabilistic forecasts for improved water supply management: Part 3 – a nonparametric probabilistic forecast model," *Journal of Hydrology*, vol. 239, no. 1-4, pp. 249–258, Dec. 2000.

[23] R. Battiti, "Using mutual information for selecting features in supervised neural net learning," *IEEE Transactions on Neural Networks*, vol. 5, no. 4, pp. 537–550, July 1994.

[24] K. Maertens, R. Babuska, and J. De Baerdemaeker, "Evolutionary input selection for the non-linear identification of complex processes," *Computers and Electronics in Agriculture*, vol. 49, no. 3, pp. 441–451, Dec. 2005.

[25] K. Levenberg, "A method for the solution of certain problems in least squares," *Quart. Appl. Math.*, vol. 2, pp. 164–168, 1944.

[26] S. Silva, *GPLAB: A Genetic Programming Toolbox for MATLAB*, 2007 ed., ECOS-Evolutionary and Complex Systems Group, University of Coimbra, Apr. 2007.

[27] J. C. Lagarias, J. A. Reeds, M. H. Wright, and P. E. Wright, "Convergence properties of the Nelder-Mead Simplex method in low dimensions," *SIAM J. on Optimization*, vol. 9, no. 1, pp. 112–147, 1998.

[28] D. E. Goldberg, *Genetic Algorithms in Search, Optimization and Machine Learning*, Addison-Wesley Longmann Publishing Inc., 1989.

[29] C. Rakopoulos, E. Giakoumis, and D. Rakopoulos, "Cylinder wall temperature effects on the transient performance of a turbocharged

diesel engine," *Energy Conversion and Management*, vol. 45, pp. 2627–2638, 2004.

[30] A. Schilling, A. Amstutz, C. H. Onder, and L. Guzzella, "A real-time model for the prediction of the NO_x emissions in DI diesel engines," in *Proc. of the 2006 IEEE International Conference on Control Applications*, Munich, Germany, 2006, pp. 2042–2047.

[31] P. Obrecht, *WEG: Benutzerhandbuch und Programmdokumentation*, IET-LAV, ETH Zurich, 2003.

[32] D. Siebers, "Scaling liquid-phase fuel penetration in diesel sprays based on mixing-limited vaporization," *SAE Technical Paper, no. 1999-01-0528*, 1999.

[33] J. Bayer and D. Foster, "Zero-dimensional soot modeling," *SAE Technical Paper, no. 2003-01-1070*, 2003.

[34] J.-S. Jang, "Input selection for anfis learning," in *Proceedings of the Fifth IEEE International Conference on Fuzzy Systems*, vol. 2, New Orleans, USA, 1996, pp. 1493–1499.

[35] L. Guzzella and C. H. Onder, *Introduction to Modeling and Control of Internal Combustion Engine Systems*. Springer-Verlag, 2004.

[36] J. Hagena, Z. S. Filipi, and D. Assanis, "Transient diesel emissions: Analysis of engine operation during a tip-in," *SAE Technical Paper, no. 2006-01-1151*, 2006.

[37] C. D. Rakopoulos and E. G. Giakoumis, *Diesel Engine Transient Operation*. Springer London, 2009.

[38] J. Jensen, A. Kristensen, S. Sorensen, N. Houbak, and E. Hendricks, "Mean-value modeling of a small turbocharged diesel engine," *SAE Technical Paper, no. 910070*, 1991.

[39] E. Alfieri, A. Amstutz, C. Onder, and L. Guzzella, "Model-based feedback control of the air-to-fuel ratio in diesel engines based on an empirical model," in *Computer Aided Control System Design, IEEE International Conference on Control Applications*, Oct. 2006, pp. 509–514.

[40] A. B. Greene and G. G. Lucas, *The Testing of Internal Combustion Engines.* English University Press Ltd., 1969.

[41] D. T. Hountalas and A. D. Kouremenos, "Development of a fast and simple simulation model for the fuel injection system of diesel engines," *Adv. Eng. Softw.*, vol. 29, no. 1, pp. 13–28, 1998.

[42] M. Diehl, H. G. Bock, H. Diedam, and P.-B. Wieber, "Fast direct multiple shooting algorithms for optimal robot control," *LNCIS*, vol. 340, pp. 65–93, 2006.

[43] D. P. Bertsekas, *Dynamic programming and optimal control.* Athena Scientific, 2005.

[44] *Optimisation Toolbox^{TM} 4.0, User's Guide*, The MathWorks, Inc., 2009.

[45] R. Fletcher, *Practical Methods of Optimization, 2nd Edition*, J. Wiley and Sons, Eds., 2000.